

# **A Study of Flow through Cellular Structures with Periodic Pore Geometry and Varying Unit Cell Sizes**

Roman Mazur

Thermal Energy and Process Engineering, TEPE4-1002, 2025-05

4<sup>th</sup> Master Thesis





**AAU Energy**  
Aalborg University  
<http://www.aau.dk>

## **AALBORG UNIVERSITY**

### STUDENT REPORT

**Title:**

A Study of Flow through Cellular Structures with Periodic Pore Geometry and Varying Unit Cell Sizes

**Theme:**

Fluid Mechanical Analysis Methods

**Project Period:**

Semester 2025

**Project Group:**

TEPE4-1002

**Participants:**

Roman Mazur

**Supervisors:**

Torsten Berning

**Number of Pages:** 90

**Date of Completion:**

May 28<sup>th</sup> - 2025

**Abstract:**

This study investigates the influence of unit cell size on the thermal and hydraulic performance of sheet-based Triply Periodic Minimal Surface (TPMS) structures, specifically Gyroid and Diamond geometries. A parametric analysis is conducted using Computational Fluid Dynamics (CFD) simulations, applying the Reynolds-Averaged Navier-Stokes (RANS) and energy equations with the  $k-\omega$  Shear Stress Transport (SST) turbulence model. The results show that a reduction in unit cell size consistently increases both pressure drop and volumetric heat transfer. From the largest to the smallest unit cell, pressure drop rises by up to 73 % for Diamond and 66 % for Gyroid structures, while volumetric heat transfer increases by as much as 57 %. At the same unit cell size, Diamond structures generally outperform Gyroid structures in volumetric heat transfer by 11 % to 17 %, primarily due to their higher specific surface area. However, Gyroid configurations exhibit Nusselt numbers up to 186 % higher with increasing unit cell size, compared to 156 % for Diamond, due to enhanced convective effects associated with more chaotic flow behavior. Performance and efficiency metrics,  $eff_P$  and  $\eta$ , reveal a trade-off. Smaller unit cells provide better volumetric heat transfer but lower energy efficiency, whereas larger unit cells result in reduced heat transfer performance but improved efficiency. Diamond structures achieve up to 40 % higher  $eff_P$  while maintaining comparable values of  $\eta$  across the entire range of unit cell sizes and are therefore considered superior to Gyroid structures.

*the author.*

*By accepting the request from the fellow student who uploads the study group's project report in Digital Exam System, you confirm that all group members have participated in the project work, and thereby all members are collectively liable for the contents of the report. Furthermore, all group members confirm that the report does not include plagiarism.*

# Preface

The following report is a Master's Thesis on the 4<sup>st</sup> semester Master in Thermal Energy and Process Engineering at the Department of Energy Technology at Aalborg University. The Thesis is written by Roman Mazur and has been supervised by Associate Professor Torsten Berning. The project was conducted in the period 1st of February 2022 to 28th of May 2022.

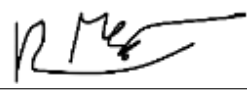
## Reading Guide

The citations have been done using the IEEE method where citations will be numbered as [1] shown in the order of appearance. The citations follow their references in the bibliography located at the end of the thesis. Figures, that are reused from previous publications follow the open access regulations of MDPI [32]. Chapters, sections, figures, tables, and equations are labeled and referenced when mentioned in the text. The numbering of these labels is in chronological order and chapter-wise. Throughout the report, some symbols and abbreviations may have different subscripts, however, these differences can be found in the Nomenclature.

The following software has been used in this thesis:

- OpenFOAM
- Paraview
- Mathworks MATLAB
- FreeCat
- Overleaf Latex
- Inkscape
- TPMSDesigner

Roman Mazur  
rmazur23@student.aau.dk

Signature:  \_\_\_\_\_

# Summary

This study examined the effect of unit cell size on the thermal and hydraulic performance of sheet-based Triply Periodic Minimal Surface (TPMS) structures, focusing on Gyroid and Diamond geometries. A parametric computational analysis was performed in the open source environment OpenFOAM, solving the incompressible Reynolds-Averaged Navier–Stokes equations coupled with the energy equation. Turbulence was modeled using the  $k-\omega$  Shear Stress Transport model. The simulation approach was verified through a grid independence study and validation against results from existing literature.

To ensure comparability, the porosity and structure length were kept constant across all cases. Periodic boundary conditions were applied in the transverse direction, a constant velocity and Temperature were imposed at the inlet, and the TPMS walls were kept at a constant temperature.

The results showed that reducing the unit cell size leads to higher pressure drop and increased volumetric heat transfer. Pressure losses increased by up to 73% in Diamond structures and 66% in Gyroid structures when moving from the largest to the smallest unit cell. Volumetric heat transfer improved by as much as 57%. Diamond structures performed better in volumetric heat transfer at each cell size, with improvements between 11 and 17% compared to Gyroid. On the other hand, the investigated geometries reached higher Nusselt numbers as the unit cell size increased, where the maximum observed increase was 186% for Gyroid and 156% for Diamond. This was due to stronger convective effects in bigger unit cells, resulting from more chaotic and turbulent flow behavior.

Performance and efficiency were assessed using the volumetric performance index  $eff_p$  and the thermal hydraulic efficiency index  $\eta$ . Smaller unit cells provided higher volumetric heat transfer but were less energy efficient. Larger unit cells reversed this trend, offering improved efficiency but lower thermal performance. Across all sizes, Diamond structures achieved up to 40 % higher  $eff_p$  while maintaining  $\eta$  values similar to those of the Gyroid structures.

In conclusion, Diamond structures generally outperform Gyroid structures over a wide range of unit cell sizes. Furthermore, smaller unit cells are more suitable for compact systems requiring high heat transfer, whereas larger unit cells are more effective when energy efficiency is the priority and space is not a major constraint.

# Nomenclature

Standard SI-Units will be used

Symbol	Explanation	Unit
$A$	Area	[m <sup>2</sup> ]
$a$	Unit cell size	[mm]
$c$	Level-set threshold for TPMS	[-]
$D_h$	Hydraulic diameter	[m]
$e$	Margin of error	[-]
$eff_p$	Volumetric performance metric	[-]
$f$	Darcy friction factor	[-]
$g$	Gravitational acceleration	[m/s <sup>2</sup> ]
$Gr$	Grashof number	[-]
$h$	Heat transfer coefficient	[W/(m <sup>2</sup> K)]
$k$	Turbulent kinetic energy	[J/kg]
$k$	Thermal conductivity	[W/(m · K)]
$L$	Structure length in flow direction	[m]
$L_c$	Characteristic length	[m]
$n$	Number of samples	[-]
$Nu$	Nusselt number	[-]
$p$	Pressure	[Pa]
$Pr$	Prandtl number	[-]
$q''$	Surface heat flux	[W/m <sup>2</sup> ]
$Re$	Reynolds number	[-]
$Ri$	Richardson number	[-]
$St$	Stokes number	[-]
$T$	Temperature	[K]
$T_f$	Film temperature	[K]
$T_s$	Surface temperature	[K]
$u$	Velocity vector	[m/s]
$u_{in}$	Inlet velocity	[m/s]
$U_\tau$	Friction velocity	[m/s]
$V_f$	Fluid volume	[m <sup>3</sup> ]
$\nu_t$	Turbulent viscosity	[m <sup>2</sup> /s]
$y^+$	Dimensionless wall distance	[-]
$\alpha$	Thermal diffusivity	[m <sup>2</sup> /s]
$\beta$	Volumetric expansion coefficient	[1/K]
$\Delta p$	Pressure drop	[Pa]
$\Delta T$	Temperature difference	[K]
$\mu$	Dynamic viscosity	[Pa · s]
$\nu$	Kinematic viscosity	[m <sup>2</sup> /s]
$\eta$	Thermal-hydraulic efficiency index	[-]
$\phi$	Porosity	[-]

# Abbreviations

Abbreviation	Explanation
TPMS	Triply Periodic Minimal Surface
CFD	Computational Fluid Dynamics
RANS	Reynolds-Averaged Navier–Stokes
SST	Shear Stress Transport
GCI	Grid Convergence Index
SIMPLE	Semi-Implicit Method for Pressure-Linked Equations
PISO	Pressure-Implicit with Splitting of Operators
LES	Large Eddy Simulation
DNS	Direct Numerical Simulation
CAD	Computer-Aided Design
STL	Stereolithography
TKE	Turbulent Kinetic Energy
VOF	Volume of Fluid
RES	Resolution

# Contents

<b>1</b>	<b>Introduction</b>	<b>1</b>
1.1	Triply minimal surfaces . . . . .	2
1.2	TPMS Literature . . . . .	3
1.2.1	TPMS topologies in heat exchangers . . . . .	4
1.2.2	TPMS topologies in Heat sinks . . . . .	5
1.3	Aim of this study . . . . .	9
<b>2</b>	<b>Case Setup</b>	<b>11</b>
2.1	TPMS Design . . . . .	13
2.2	Dimensionless and Performance Parameters . . . . .	14
<b>3</b>	<b>Computational Procedure</b>	<b>17</b>
3.1	Reynolds average Navier Stokes turbulence modelling . . . . .	18
3.1.1	The $k - \epsilon$ and $k - \omega$ model . . . . .	20
3.1.2	The Shear-Stress Transport $k - \omega$ model . . . . .	21
3.1.3	The Reynolds-averaged temperature equation . . . . .	21
3.1.4	Wall treatment . . . . .	22
3.2	Boundary treatment . . . . .	24
3.3	Simulation Setup . . . . .	25
<b>4</b>	<b>Computational Mesh</b>	<b>30</b>
4.1	Mesh-Quality Metrics . . . . .	30
4.2	Mesh Generation . . . . .	32
<b>5</b>	<b>Verification and Validation</b>	<b>35</b>
5.1	Convergence . . . . .	35
5.2	Grid Independence . . . . .	37
5.2.1	Grid convergence study . . . . .	37
5.3	Incompressibility Assumption . . . . .	39
5.4	Experimental Validation . . . . .	41
<b>6</b>	<b>Results and Discussion</b>	<b>44</b>
6.1	Geometry . . . . .	44
6.2	Flow Path and Structure . . . . .	45
6.3	Thermal distrubtion . . . . .	53
6.4	Parametric study Results . . . . .	55
6.4.1	hydraulic metrics . . . . .	56
6.4.2	thermal metrics . . . . .	58
6.4.3	dimensionless Analysis . . . . .	60
6.4.4	Efficiency Metrics . . . . .	62
<b>7</b>	<b>Conclusion</b>	<b>66</b>
<b>8</b>	<b>Future work</b>	<b>68</b>

<b>Bibliography</b>	<b>69</b>
<b>A Appendix</b>	<b>76</b>
A.1 Inflow conditions . . . . .	76
A.2 Derivation of the Trasport euations for $k$ , $\epsilon$ and $\omega$ . . . . .	76
A.2.1 Transport equation for the Reynolds stresses . . . . .	76
A.2.2 Transport equation for $k$ and $\epsilon$ . . . . .	77
A.2.3 Transport equation for the specific dissipation $\omega$ . . . . .	78
A.3 Numerical methods . . . . .	79
A.4 Solver . . . . .	81
A.5 SnappyHexMeshDict . . . . .	83
A.6 Nusselt Number Calculation in Buoaynt Solver . . . . .	86
A.7 Finite Volume Schemes Settings . . . . .	88

# Chapter 1

## Introduction

In the last decade, additive manufacturing (AM) and 3D printing technologies have rapidly advanced, establishing themselves as versatile methods capable of fabricating highly complex and customized geometries. A variety of technique, such as laser sintering, fused deposition modeling, material jetting, stereolithography, and selective laser melting, enable the production of components from metals, polymers, and composite materials, with minimal design constraints [69].

This extensive design and material flexibility allows manufacturing of complicated functional models as novel solutions to common engineering problems, such as multifunctional components tailored for specific performance demands, lightweight load-bearing structures or high-surface-area components for increased heat transfer.

Most notably, cellular structures with ordered and periodic pore geometries have gained significant attention, as they enable the tailoring of key design properties such as stiffness, strength, permeability, thermal conductivity, and thermal diffusivity. This makes them particularly suitable for heat transfer applications like heatsinks, where a combination of low thermal resistance, high permeability, large surface-area-to-volume ratio, and enhanced convective heat transfer performance is highly desirable [12]. These regular, repeating cellular architectures are commonly referred to as lattices, in contrast to traditional foams, which exhibit irregular and often random pore structures.

One prominent class of lattice structures receiving significant research attention are strut-based lattices. These architectures consist of interconnected beams (struts) that form periodic, repeating unit cells, as illustrated in Figure 1.1. Studies have shown that heat exchangers and heat sinks designed with these strut-based lattices not only outperform conventional stochastic foams but can also surpass the performance of traditional turbulators, like fin-based designs[15, 21, 31, 73].

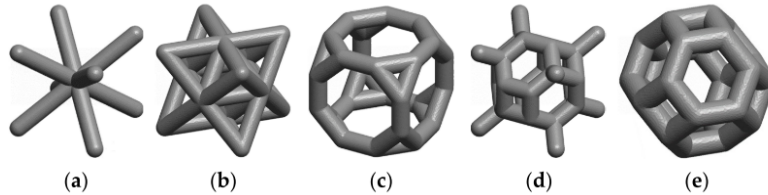


**Figure 1.1:** Different strut based lattices as shown in the review by Yeranee et al. [75]

Another emerging class of lattice structures that has gained considerable attention in recent years comprises three-dimensional shell-based architectures derived from Triply Periodic Minimal Surfaces (TPMS), which provide distinct advantages over strut-based lattices.

These architectures have been shown to possess superior fatigue resistance, improved viscoelastic performance, and enhanced structural stability compared to their strut-based counterparts [22, 61, 62]. Furthermore, TPMS lattices exhibit greater permeability in the direction of longitudinal fluid flow and higher effective thermal conductivity, making them particularly interesting for thermal applications [35, 75].

## 1.1 Triply minimal surfaces

The aforementioned lattices are derived from minimal surfaces, which are geometric surfaces defined by zero mean curvature ( $H = 0$ ) at every point. This condition implies that the surface bends with equal magnitude but in opposite directions along its two principal curvature directions. The principal curvatures, denoted  $k_1$  and  $k_2$ , correspond to the maximum and minimum normal curvatures at a given point and are formally defined as the eigenvalues of the Weingarten map, a matrix that characterizes the local curvature of a surface. Consequently, for a surface to qualify as minimal, the sum of the principal curvatures must be zero at each point ( $H = \frac{1}{2}(k_1 + k_2) = 0$ ). Geometrically, this results in a particular surface that can not be made smaller by local deformations [16].

Triply periodic minimal surfaces (TPMS) are a subclass of minimal surfaces, that are infinitely repeating periodically in three independent spatial directions [75]. The first TPMS to be discovered were the Diamond surface, described by Schwarz, and the Neovius surface, introduced by Neovius in the 19th century [39, 60]. They went on to discover additional minimal surfaces, including the Primitive and Hexagonal types. Nearly a century later, in the mid-20th century, Schoen introduced several new types of TPMS, with the most notable being the Gyroid surface [59].

TPMS structures can be designed based on mathematical algorithms describing the minimal surface. One of the most commonly used approaches is the level-set method, which represents the surface through an equation derived from a Fourier series expansion [17]. The equation is composed of a combination of trigonometric functions that define an implicit surface satisfying the condition  $\Phi(x, y, z) = c$  [75]. Some level-set equations for the most common TPMS structures can be seen below.

$$\text{Primitive: } \cos(2\alpha\pi x) + \cos(2\beta\pi y) + \cos(2\gamma\pi z) = c \quad (1.1)$$

$$\text{Diamond: } \cos(2\alpha\pi x) \cos(2\beta\pi y) \cos(2\gamma\pi z) - \sin(2\alpha\pi x) \sin(2\beta\pi y) \sin(2\gamma\pi z) = c \quad (1.2)$$

$$\text{Gyroid: } \sin(2\alpha\pi x) \cos(2\beta\pi y) + \sin(2\beta\pi y) \cos(2\gamma\pi z) + \sin(2\gamma\pi z) \cos(2\alpha\pi x) = c \quad (1.3)$$

In this context,  $\alpha$ ,  $\beta$ , and  $\gamma$  are scaling constants that define the dimensions of the unit cell, which is defined as the smallest repeating volume that characterizes the periodic geometry of the lattice. The parameter  $c$  controls the isosurface offset level. When  $c = 0$ , the surface has zero thickness and divides the space symmetrically into two equal subdomains (see Figure 1.2a).

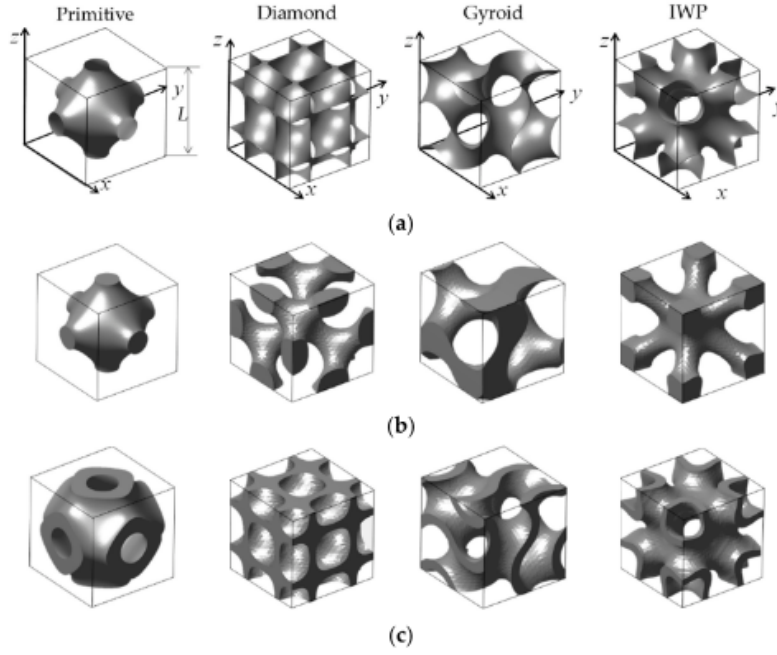


**Figure 1.2:** Different TPMS lattices as shown in the review by Yeranee et al. [75]

Two different approaches can be taken to generate TPMS lattices based on the level-set equation. Solid-network structures are created by setting  $c$  to a positive value and solidifying the enclosed volume (Figure 1.2b). Sheet-network structures are produced by solidifying the volume enclosed between two minimal surfaces evaluated at  $\pm c$  (Figure 1.2c). For both structures, the parameter  $c$  is directly related to the volume fraction ( $V_f$ ), which is defined as the ratio of the volume occupied by the lattice to the total volume. It also serves as an indicator of porosity ( $\phi$ ), where  $\phi = 1 - V_f$  [2].

Sheet- and solid-network TPMS structures exhibit fundamentally different morphological characteristics. In solid-based TPMS lattices, the void space typically forms a single, continuous, and interconnected domain. In contrast, sheet-based TPMS structures divide the void space into two distinct, non-interconnected regions, resulting in fundamental differences in pore size, wall thickness, and surface area-to-volume ratio. As a result, TPMS structures of the same type (e.g., Gyroid, Diamond...) and with identical porosity can exhibit markedly different mechanical, mass transport, and heat transfer properties depending on whether they are designed as solid or sheet networks.

The high versatility in tailoring design parameters such as TPMS type, network configuration, porosity, and unit cell size has facilitated an increasing amount of research centering around the implementation of TPMS structures across a wide range of heat transfer applications.

## 1.2 TPMS Literature

One of the earliest studies to explore the thermal properties of triply periodic minimal surface (TPMS) structures was conducted by Abueidda et al. [1] in 2016. In this work, the authors numerically investigated the effective thermal conductivities of cellular materials

based on various sheet-network TPMS architectures. Their findings demonstrated that TPMS-based foams exhibit significantly higher thermal conductivity compared to conventional strut-based lattice structures at equivalent void fractions. Furthermore, it was observed that the effective thermal conductivity increases approximately linearly with increasing solid volume fraction.

Building on this work, Catchpole-Smith et al. [8] conducted an experimental investigation of TPMS lattices fabricated using laser powder bed fusion. The study focused on three specific TPMS geometries, namely Diamond, Gyroid, and Primitive, and aimed to experimentally characterize their thermal conductivities. Consistent with the earlier numerical findings, volume fraction was identified as the dominant factor influencing thermal performance. Among the geometries tested, the Primitive lattice exhibited the highest thermal conductivity, followed by the Diamond and Gyroid structures.

Other studies, including those by Mirabolghasemi et al.[34] and Qureshi et al.[53] have further demonstrated that TPMS geometries significantly enhance thermal conduction compared to conventional foam and lattice structures, making them prime candidates for heat transfer applications.

In recent years, research has expanded on this by placing greater effort into testing TPMS structures as a mean to also increase convective heat transfer. This research can roughly be divided into two main applications: heat sink applications and two-fluid heat exchangers [75].

### **1.2.1 TPMS topologies in heat exchangers**

As discussed in Section 1.1, sheet-network TPMS structures inherently partition space into two continuous, interwoven domains. This characteristic makes them highly promising for heat exchanger applications, where thermal energy must be transferred efficiently between separate fluid streams [75].

Building on this concept, Iyer et al. [24] conducted a numerical study to evaluate the performance of TPMS-based heat exchangers in laminar flow regimes. Their results showed a substantial improvement in convective heat transfer compared to conventional tube-based designs. For instance, at Reynolds numbers around 100, TPMS geometries achieved Nusselt numbers 3–5 times higher, while at  $Re = 300$ , enhancements reached up to 14 times compared to tube-based heat exchangers. Among the structures tested, the Diamond topology delivered the highest heat transfer performance, with a 14-fold increase in the Nusselt number accompanied by a 9-fold rise in the friction factor. The Neovius structure exhibited similar thermal performance but suffered from significantly higher pressure losses, with a friction factor nearly 20 times greater than that of a smooth tube. The Gyroid structure, although slightly less effective in heat transfer, offered a more favorable pressure drop of approximately half that of Neovius, positioning it as the second-best performer overall in laminar flow conditions.

Similar observations were made by Cheng et al. [9], who investigated the influence of morphology in TPMS structures on flow resistance, heat transfer performance, and me-

chanical strength in laminar flow regime. Their study compared four TPMS variants, iWP, Primitive, Diamond, and Gyroid, against a conventional simple cubic structure. Numerical simulations revealed that TPMS structures achieved up to 25 % higher volumetric heat transfer coefficients and 20 % higher local (interstitial) heat transfer coefficients than the cubic structure. A comparison of the TPMS structures showed that the Diamond, Gyroid, and iWP configurations offer superior heat transfer performance, whereas the Primitive structure results in the lowest pressure drop. Structurally, the Diamond and Gyroid lattices exhibited greater mechanical strength compared to the iWP and Primitive configurations.

An inquiry with higher Reynolds numbers was performed by Jiaxuan Wang et al.[67], who conducted a combined numerical and experimental investigation of a sheet network TPMS heat exchanger manufactured using Selective Laser Melting. The study evaluated performance over a Reynolds number range from 400 to 6000, focusing on flow resistance, heat transfer characteristics, and overall efficiency. Among the investigated TPMS configurations, the Gyroid structure exhibited the lowest pressure drop, which was only 23 % of that observed for the Primitive structure, the configuration with the highest flow resistance. The Fischer-Koch S structure achieved the highest total heat transfer rate, although this was accompanied by a significantly higher pressure drop. Both the Diamond and Gyroid structures demonstrated the highest Nusselt numbers, reflecting strong convective heat transfer performance. Furthermore, the Gyroid structure achieved the highest Performance Evaluation Criterion (PEC) across the entire range of flow conditions, surpassing the performance of a conventional plate heat exchanger by up to 54 %. However, at higher flow rates, the Diamond structure exhibited the best overall thermal and hydraulic performance among the TPMS configurations.

A similar observation was reported by Brambati et al.[7], who conducted a numerical investigation of convective heat transfer in Gyroid, Diamond, and Primitive TPMS-based heat exchangers over a Reynolds number range of 5,000 to 50,000. Their study explored the effect of porosity, testing values between 70 % and 90 %. In agreement with the findings of Jiaxuan Wang et al., they observed that the Gyroid and Diamond structures outperformed the Primitive geometry in terms of convective heat transfer. Furthermore, the Gyroid structure demonstrated the best overall performance across all porosities, while the Diamond configuration showed comparably high convective heat transfer performance at lower porosity levels.

Further studies by Brambati et al. [7], Wang et al. [68], El Khadiri et al. [28], and others, all showing the benefits of using of TPMS topologies as heat exchangers.

### **1.2.2 TPMS topologies in Heat sinks**

The second main usage for TPMS-structure in thermal systems are heat sinks. In heat sink applications, a cooling fluid at a controlled inlet temperature flows through channels containing the TPMS structure before exiting at the outlet. Typically, two configurations are employed: one in which the surrounding walls serve as the heat source, and another where the TPMS structure itself acts as the heat-generating element [75]. Both sheet- and solid-network structures have been investigated.

Tang et al. [63], for example, employed both experimental and numerical approaches to evaluate the performance of various sheet-based TPMS heat sink structures compared to a traditional fin-based model, within the laminar flow regime ( $Re = 166\text{--}943$ ) and a temperature gradient of approximately 80 K. Their findings revealed that TPMS structures exhibited up to a 207 % increase in convective heat transfer coefficient and up to a 196 % increase in Nusselt number relative to the fin model. Among the TPMS designs, the Diamond and Gyroid structures demonstrated significantly greater enhancements in Nusselt number than the iWP structure. When accounting for pressure drop, the performance evaluation coefficient (PEC) indicated  $PEC > 1$  for Diamond and Gyroid, confirming superior overall performance over the fin-based model, while the iWP structure showed  $PEC < 1$ , suggesting inferior performance.

A comparison of both sheet- and solid-TPMS heat sinks was performed by Khalil et al. [29], who compared Gyroid-Solid, Diamond-Solid, and Gyroid-Sheet structures across a broad range of Reynolds numbers. Their study revealed that the Gyroid-Sheet topology outperformed both solid structures in terms of Nusselt number and areal heat transfer coefficient for  $Re > 6800$ , owing to its significantly higher surface area density. However, this enhanced thermal performance came at the cost of a substantially higher pressure drop, reaching up to 3.9 times that of the Gyroid-Solid, which had the lowest pressure drop due to its larger pore size. Under conditions of fixed pumping power, the solid-network structures, particularly the Diamond solid demonstrated superior thermal efficiency, with the highest efficiency index among the three.

A few studies have also explored the feasibility of using TPMS heat sinks in free convection environments. One such investigation was conducted by Baobaid et al. [6], who studied fluid flow and heat transfer characteristics of Gyroid-solid, Gyroid-sheet, and Diamond-solid heat sinks as passive cooling solutions under natural convection. Their findings showed that horizontally aligned heat sinks outperformed vertically oriented ones by 7–11 %, due to more favorable airflow pathways. Among the geometries tested, the Diamond and Gyroid-solid structures consistently exhibited the lowest surface temperatures across most boundary conditions, identifying them as strong candidates for passive cooling applications. In contrast, the Gyroid-sheet structure generally underperformed, primarily due to its high flow resistance.

In addition to general performance studies, TPMS heat sinks have also been investigated in the context of specific applications. One such application is electronics cooling, where Ansari et al. [4] explored the use of gyroid TPMS heat sinks for managing the thermal loads of high-performance microprocessors. These water-cooled designs were compared to conventional pin-fin heat sinks under laminar flow conditions. The TPMS structure demonstrated a 28 % reduction in thermal resistance, which corresponded to a 4.7 % decrease in maximum temperature. However, this thermal improvement came at the cost of a significantly higher pressure drop, up to 559 %.

Another implementation was explored by Prussack et al. [52], who experimentally evaluated Gyroid and Diamond TPMS geometries as alternative heat transfer surfaces for nuclear reactor cores. Their findings demonstrated that, across a Reynolds number range of 500 to 7,000, both TPMS designs significantly outperformed a conventional rod bundle,

achieving 8 to 10 times higher Nusselt numbers. This improvement in thermal performance, however, was accompanied by a friction factor up to 90 times greater. Moreover, the TPMS structures were capable of supporting up to 2.5x higher power densities than the rod bundle.

The feasibility of TPMS structures in other energy applications, such as gas turbines, was investigated by Yeranee et al. [76], who performed a topology optimization of a diamond TPMS heat sink integrated into a serpentine cooling channel for gas turbines, aiming to minimize pressure losses while maintaining high heat transfer performance. The optimized design placed a diamond sheet network behind the first bend of the serpentine channel. The study examined the effects of varying unit cell sizes, orientations relative to the flow direction, and constant versus variable wall thicknesses. Both numerical and experimental methods were employed across a Reynolds number range of 10,000 to 40,000. The results showed that for all configurations, the total Nusselt number increased by 45–60 %, while pressure drop decreased by up to 30 % due to the mitigation of Dean vortices in the serpentine channel. Among the investigated parameters, unit cell size had the most significant impact on performance, whereas orientation played a comparatively minor role. Notably, smaller unit cell sizes yielded the highest heat transfer enhancement—up to 70 % compared to a plain serpentine channel, but with a more modest reduction in pressure drop.

The presented studies highlight the potential of TPMS structures for enhancing heat transfer across a broad range of applications. However, for these structures to gain wider adoption in industrial settings, a clear understanding of how design parameters influence their thermal and hydraulic performance is essential. While some studies have explored various parameters in the context of TPMS-based heat exchangers, only a limited number have focused on these effects specifically for TPMS heat sinks [75].

One such study was conducted by Attarzadeh et al. [5], who examined the influence of wall thickness on the thermal performance of TPMS heat sinks based on the Diamond structure. Their findings demonstrated that increasing wall thickness (e.g., TPMS4), which reduces porosity, leads to adverse flow characteristics such as backflow and higher flow resistance. In contrast, thinner-walled designs (e.g., TPMS1) enabled smoother flow, resulting in a 2.5x lower pressure drop and 2x higher permeability compared to TPMS4. In addition, TPMS1 achieved a 2.5x higher heat transfer coefficient.

A more comprehensive study on how pore-scale geometric parameters of TPMS heat sinks influence their convection heat transfer performance, to identify optimal trade-offs between heat dissipation and pressure drop, was performed by Anacreonte et al. [3]. They carried out a multi-objective shape optimization of five TPMS topologies—Gyroid, Diamond, iWP, Primitive and Neovius, by systematically varying porosity and stretch factor in a laminar flow regime. Using a genetic algorithm coupled to CFD, they demonstrated that, by tuning geometry parameters, the volumetric Nusselt number can be increased by up to 245.6 % for a fixed wall-temperature case and 76.3 % for the fixed wall-heatflux case, at the expense of friction factor penalties up to 21.7x and 12.0x, respectively. Furthermore, they found that Diamond-type structures dominated the Pareto front under constant-flux heating, while Primitive cells achieved the highest Nusselt numbers under

constant-temperature heating.

The effect of compression was also investigated by Yan et al. [74], who computationally and experimentally analyzed the effects of structural modifications involving compression along different directions and varying degrees of compression for Diamond-solid TPMS heat sinks. Therefore, four modified Diamond structures were designed, one compressed along the flow direction and three compressed along the spanwise direction with varying degrees. They found that the spanwise compression structures exhibited increased overall heat transfer coefficients compared to the original Diamond-solid structure. This increase was shown to be more pronounced for tighter compression. Similarly, the PEC, accounting for both heat transfer and pressure drop, was shown to be up to 34% higher for the spanwise compressed lattices. The structure compressed along the flow direction showed a significant increase in heat transfer (68.5%), but also exhibited a drastically increased pressure drop (448.5%) compared to the original lattice.

A numerical investigation into the effect of porosity, cell size, and material choice on the heat transfer and flow performance of Gyroid heat sinks was undertaken by Samson et al. (2023) [57]. Their findings showed that reducing cell size notably increased surface area, significantly enhancing heat transfer performance. Specifically, decreasing the cell size from the largest to the smallest studied resulted in up to 200 % increase in heat transfer coefficient. Porosity variation also had a substantial impact. Lowering porosity from 80 % to 60 % resulted in approximately a 70 % higher heat transfer coefficient but significantly increased pressure losses, up to 7x more than the higher porosity configurations at the same Reynolds number. Material selection was also shown to markedly influence thermal performance. Compared to aluminum, employing OFHC copper reduced thermal resistance by approximately 12.1 %, while switching to 4340 steel increased thermal resistance by over 102 %, due to steel's lower thermal conductivity. Overall, Gyroid heat sinks demonstrated superior thermal performance compared to traditional fin-based designs, reducing thermal resistance by up to 53 %, increasing the Nusselt number by up to 300 %, and enhancing overall performance efficiency by up to 42 % at certain Reynolds number ranges.

The possibility of reducing the friction factor by employing functionally graded TPMS heat sinks was investigated by Al-Ketan [2]. First, they compared a uniform Gyroid sheet network, a Gyroid solid network, and a Diamond solid network heat sink. The Gyroid sheet network delivered the highest overall convective heat transfer coefficient among the three, but also experienced the largest pressure drop. Between the two solid networks, the Diamond solid network achieved a heat transfer coefficient 32 % greater than that of the Gyroid solid network, albeit with a 33 % higher pressure drop. When the Reynolds number was varied at a fixed heat flux of 100 W, the Gyroid sheet network's heat transfer coefficient rose by about 60 % over the studied range, compared with increases of 48 % for the Gyroid solid network and 45 % for the Diamond solid network. In every case the pressure drop increased exponentially as the Reynolds number grew. They then applied functional grading to the Diamond solid network by expanding the porosity from 10 % at the inlet to 30 % at the outlet, which increased the pressure drop by 112 % and raised the heat transfer coefficient by 14 %; reversing that gradient (30 % to 10 %) cut the pressure drop by 4.5 % but also reduced the heat transfer coefficient by 12 %.

Building on that, Qureshi et al [53] investigated the effects of porosity and functional grading on the heat transfer performance of architected lattices based on TPMS structures embedded with phase change materials. They found that a porosity reduction from 90 % to 60 % significantly reduced melting times by over 75 % and increased the heat transfer coefficient by over 300 % under natural convection scenarios. Conversely, a negative grading of porosity consistently degraded performance, increasing melting time by about 15–20 % and significantly reducing the heat transfer coefficient. The Primitive type performed the best, as it benefits most from natural convection, showing the largest increase in Heat transfer coefficient (over 20 %) when compared to pure conduction at 75 % porosity.

This literature review gives an overview of past research conducted on TPMS structures in heat transfer applications. More comprehensive and in-depth literature analysis were conducted by Yeranev [75] and Dutkowski [14].

### 1.3 Aim of this study

As can be seen, a lot of research has been conducted, demonstrating that TPMS structures are well-suited for heat transfer applications. It has been shown that, due to their continuous, interconnected domains and high surface area densities, these novel geometries can significantly enhance thermal conduction and convection compared to conventional pin-fin, lattice, and foam structures.

TPMS heat sinks, in particular, demonstrate significant potential across different applications, ranging from small-scale, such as electronics cooling, to large-scale like nuclear reactor cores and gas turbine cooling. Numerous TPMS geometries have been investigated across different flow regimes to identify optimal designs. In the laminar flow regime, the Diamond and IWP topologies consistently exhibit the best heat transfer performance. However, when considering a balance between thermal performance and pressure loss, the Gyroid topology achieves a similar performance as the Diamond topology.

At higher Reynolds numbers, the Diamond topology continues to exhibit excellent heat transfer performance, typically surpassed only by the Fischer-Koch geometry, which achieves the highest convective heat transfer enhancement, though this comes with a significantly higher pressure drop. Despite the Diamond structure's thermal efficiency, it is often surpassed by the Gyroid topology in terms of overall performance under turbulent flow conditions, owing to the Gyroid's significantly lower pressure drop. Furthermore, comparisons between sheet- and solid-based TPMS structures reveal that while solid networks typically deliver superior hydraulic performance, they also incur considerably lower heat transfer compared to their sheet counterparts.

Hence, the sheet Gyroid and Diamond structures emerge as the most promising candidates for high performing TPMS heat sinks. They consistently demonstrate high heat transfer coefficients and favorable performance evaluation criteria, offering an effective combination of strong convective heat transfer and manageable pressure drops, particularly when

compared to other TPMS configurations.

The performance of TPMS heat sinks is strongly influenced by key design parameters such as porosity, wall thickness, compression orientation, and material selection. Studies have shown a close relationship between porosity and wall thickness, with increased wall thickness generally resulting in reduced porosity. This reduction enhances heat transfer performance by increasing the effective thermal conductivity and available surface area, at the expense of significantly higher pressure drops. Directional compression of the structure has been shown to significantly enhance convective heat transfer. However, when compression is applied along the flow direction, it also leads to a substantial increase in pressure losses. Also the material selection plays a critical role in the thermal performance of TPMS heat sinks. High-conductivity materials, such as copper demonstrated to significantly enhance heat dissipation, whereas low-conductivity materials, like certain steels or Polymers, considerably reduce thermal efficiency.

Despite extensive research on TPMS-heat sinks, the effect of TPMS unit cell size on heat sink performance remains comparatively underexplored, representing an important knowledge gap that this study will try to close. The investigation will be conducted on Gyroid- and Diamond-sheet structures, as they have been proven to be the most promising topologies. Therefore, the aim of this investigation can be stated as follows:

*What is the effect of unit-cell size on the heat-transfer and flow characteristics in Gyroid and Diamond sheet-network heat sinks?*

To address this question, a parametric study is conducted using computational fluid dynamics (CFD) simulations in the open-source software OpenFOAM.

## Chapter 2

### Case Setup

As previously mentioned, this study focuses on two TPMS topologies: the Gyroid and Diamond sheet structures. For simplification and clarification, a new naming convention is introduced. The term "G" refers to the Gyroid, while "D" denotes the Diamond structure. Since the investigation involves varying unit cell sizes, the naming scheme is further extended to include the unit cell size if necessary. For example, a Gyroid structure with a 10 mm unit cell will be referred to as "10G", whereas a Diamond structure with a 5 mm unit cell will be denoted as "5D".

The case study is conducted within a computational domain measuring 60 mm in length, and is subdivided into three distinct regions: a 10 mm inflow section, a central region containing the TPMS structure, and a 20 mm outflow section, to ensure that entrance and exit effects are adequately captured, without interfering with the internal flow characteristics of the TPMS region itself. The height and width are set to two times the unit cell size  $a$ . The full geometrical setup can be seen in Figure 2.1.

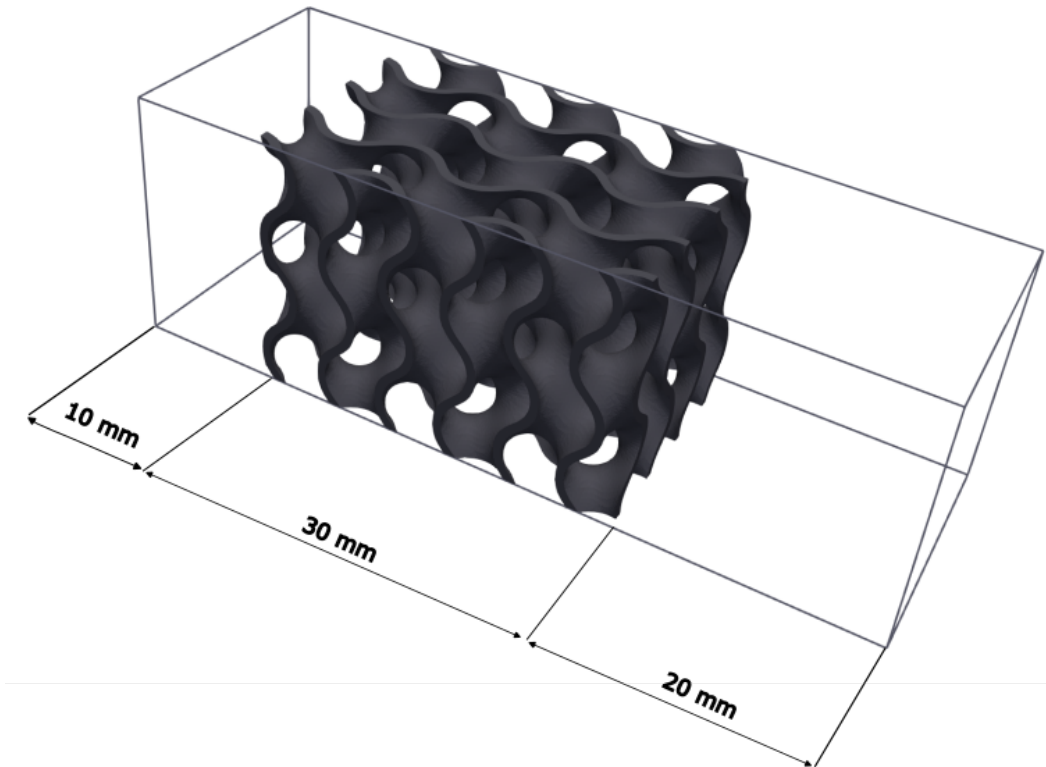


**Figure 2.1:** Geometrical Setup of the Domain and the TPMS-Structure (here: G-sheet) confined in it

In contrast to the height and width of the domain, the length of the TPMS structure in the flow direction is kept constant for two main reasons. First, in confined flows, the pressure drop is directly proportional to the length in the flow direction, i.e.,  $\Delta P \propto L$  [20].

Varying the structure length would therefore complicate the comparison of hydraulic performance across different unit cell sizes. Second, this approach reflects real-world design constraints, where the allowable device length is typically dictated by packaging requirements or a maximum acceptable pressure-drop.

To further isolate the influence of varying unit cell size, the porosity  $\phi$  is held constant at 80 % across all cases. Additionally, wall effects induced by confinement, which can significantly influence flow behavior and consequently thermal performance, are mitigated by applying periodic boundaries in both the y and z directions. Those have the effect that flow exiting one side of the domain reenters from the opposite side, effectively creating an unbounded and repeating environment in those directions.

This approach is adopted because changing the unit cell size has a strong impact on the relative areas of the channel walls and the TPMS surfaces exposed to the fluid. For example, within the same spatial domain, the 5G structure yields a wall-to-gyroid area ratio of 0.54, while the finer 15G structure achieves a ratio of 0.36. Since skin friction and turbulence generation are directly proportional to the contact area [58], channel-wall effects would vary across cases, making it difficult to isolate the influence of the unit-cell size. Practically, this approach represents the center of a larger periodic cellular structure, where the influence of external channel walls is negligible.

As a fluid, air is chosen in this study. Furthermore, the TPMS structures are set to have a uniform temperature of 353 K (80°C), with an inflow fluid temperature of 298 K (25°C). At the inlet, a Reynolds number (Re) of 5,000 is prescribed, which results in an inlet velocity of 3.7 m/s. This inflow velocity, which is kept constant across the cases, is calculated based on the 10G lattice, where the channel height is used as the characteristic length, and air properties at 298 K and ambient pressure (see Appendix A.1).

Because the inlet is driven with the same superficial velocity in every simulation and each case is generated at an identical porosity, the average pore velocity in the lattice remains unchanged from one geometry to the next, which can be seen in the continuity relation

$$\langle u \rangle_{pore} = \frac{1}{V_f} \int_{V_f} u dV = \frac{1}{\phi V} \int_{V_f} u dV = \frac{u_{in} A_{in}}{A_{domain} \phi} = \frac{u_{in}}{\phi}$$

which assumes the same value for all unit-cell sizes.

## 2.1 TPMS Design

The design of the TPMS structures through this work is done on the basis of the zero-level set of a suitably chosen implicit function, as described in section 1.1. These trigonometric expressions produce the characteristic triply-periodic Gyroid and Diamond surfaces. The precise mathematical algorithms used to construct each TPMS in this study are listed below:

Diamond:

$$\Phi_D = \cos(2\alpha\pi x) \cos(2\beta\pi y) \cos(2\gamma\pi z) - \sin(2\alpha\pi x) \sin(2\beta\pi y) \sin(2\gamma\pi z) = c \quad (2.1)$$

Gyroid:

$$\Phi_G = \sin(2\alpha\pi x) \cos(2\beta\pi y) + \sin(2\beta\pi y) \cos(2\gamma\pi z) + \sin(2\gamma\pi z) \cos(2\alpha\pi x) = c \quad (2.2)$$

To generate a sheet structure from these surface equations, the directing surface needs to be thickened. Hereby, the constant  $c$  serves as a threshold that partitions the domain into solid and fluid regions. Formally, the solid domain is defined by solidifying the volume enclosed by  $\pm c$ . By adjusting  $c$  up or down, the entire surface shifts in or out, which uniformly adjusts the thickness of the wall and therefore changes the Volume-fraction ( $V_f$ ). Consequently, a correlation between  $c$  and  $V_f$  can be found, which for the Gyroid-sheet and the Diamond-sheet structures follows the linear relationships  $V_{fG} = 0.65c$  and  $V_{fD} = 1.2c$ , respectively [2]. Since  $V_f$  is held constant at 20 % for all cases,  $c$  is set to 0.31 for the Gyroid cases and 0.17 for the Diamond cases.

The adjustment of the TPMS unit-cell size is effectively done by varying the parameters  $\alpha$ ,  $\beta$ , and  $\gamma$  in the implicit level-set functions. These parameters determine the fundamental spatial periodicity of each trigonometric term. For example, the factor

$$\sin(2\pi \alpha x) \quad (2.3)$$

has period

$$\Delta x = \frac{1}{\alpha} \quad (2.4)$$

along the  $x$ -direction. Consequently, in a cubic domain of side length  $L$ , setting  $\alpha = \beta = \gamma = N \in \mathbb{N}$  yields exactly  $N$  full unit cells in each coordinate direction. Each cell then has side length

$$a = \frac{L}{N}. \quad (2.5)$$

Hence, setting the side length  $a$  inherently changes  $\alpha$  in the level-set equation. Since the domain length is fixed in  $x$ -direction,  $\alpha$  can take non-integer values (for instance  $N + \frac{1}{2}$  or  $N + \frac{1}{3}$ ), leading to the computational box containing  $N$  complete cells plus a fractional

cell of one-half or one-third at the boundary [16]. The Matlab package TPMSDesigner, developed by Jones et al. [26], automates this entire workflow and is used to generate the TPMS geometries for the present study.

The selection of the range for the unit cell sizes is based on the reference cases 10D and 10G. The upper and lower bounds are chosen to be unit cell sizes of 15 mm and 5 mm, respectively, as shown in Figure 2.2. This setup tests a wide range of scenarios while still maintaining a reasonable spread in cell size variation, which could be applicable in industrial applications.

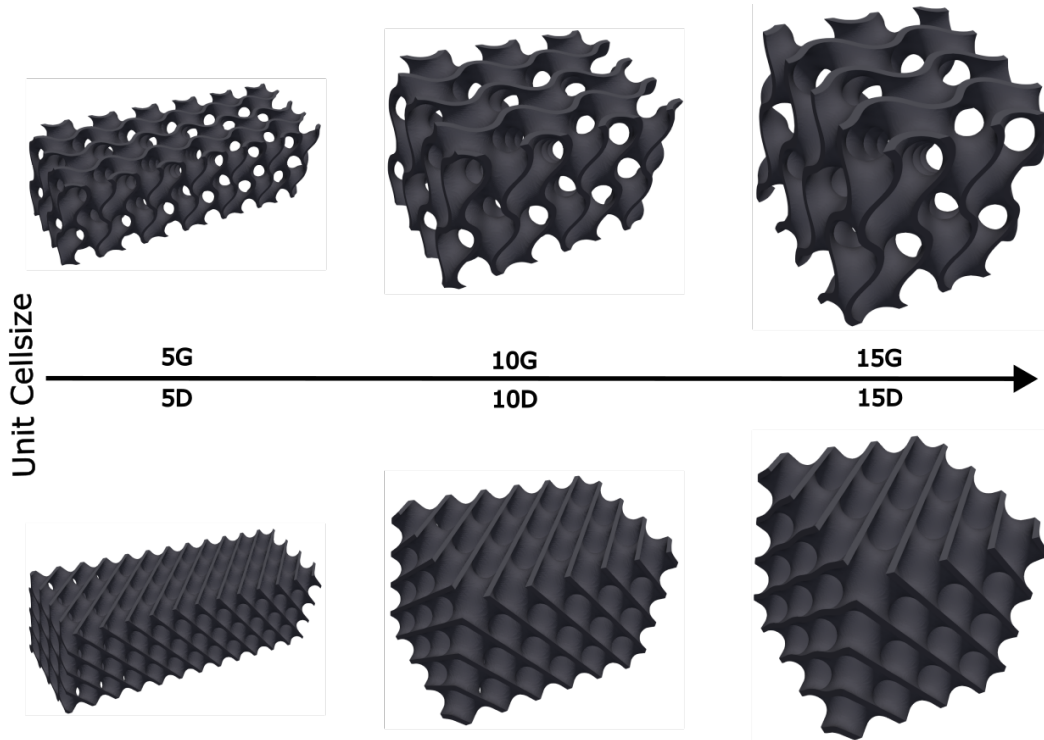


Figure 2.2: Different G and D- geometries for the cellsized 5, 10 and 15

## 2.2 Dimensionless and Performance Parameters

Various dimensionless parameters are employed throughout this study, as they provide means to evaluate and compare the thermal performance of different topologies and unit cell sizes.

One such parameter, commonly used to characterize convective heat transfer in fluid systems, is the Nusselt number (Nu). It quantifies the ratio of convective to conductive heat transfer across a fluid–solid interface. In turbulent flows through TPMS geometries, the average Nusselt number is typically on the order of  $10^2 - 10^3$ , indicating that convective heat transfer dominates and conduction within the fluid plays a minor role [75]. It is defined as [23]

$$Nu = \frac{hL_c}{k}, \quad (2.6)$$

where  $h$  is the convective heat transfer coefficient [ $W/(m^2K)$ ],  $L_c$  is the characteristic length [ $m$ ], and  $k$  is the thermal conductivity of the fluid [ $W/(mK)$ ].

In the context of numerical simulations, the convective heat transfer coefficient  $h$  is commonly evaluated using field-averaged quantities, particularly when a constant surface temperature boundary condition is applied. It is defined as [66]

$$h = \frac{q''}{T_s - T_f}, \quad (2.7)$$

where  $q''$  is the surface heat flux,  $T_s$  is the surface temperature, and  $T_f$  is the reference fluid temperature. In this study,  $T_f$  is taken as the volume-averaged temperature of the fluid domain.

Substituting this expression into the definition of the Nusselt number yields

$$Nu = \frac{q'' L_c}{k(T_s - T_f)}, \quad (2.8)$$

In simulations with an imposed temperature boundary condition, the surface heat flux  $q''$  can be estimated using Fourier's law:

$$q'' = -k \left. \frac{\partial T}{\partial n} \right|_{\text{wall}}, \quad (2.9)$$

where  $\frac{\partial T}{\partial n}$  is the temperature gradient normal to the heated surface. This gradient is typically computed from the numerical solution at the fluid–solid interface using the central differencing method [66]:

$$\left. \frac{\partial T}{\partial n} \right|_{\text{wall}} \approx \frac{T_P - T_F}{\Delta x} \quad (2.10)$$

where  $T_F$  is the fluid temperature at the first cell and  $\Delta x$  is the distance between the first cell and the wall face.

To assess and compare the hydraulic performance of the different TPMS- configurations, the Darcy friction factor is employed. This dimensionless quantity characterizes the pressure loss due to flow resistance relative to the fluid's dynamic pressure [20]:

$$f = \frac{2 \Delta p}{\rho u_{\text{in}}^2} \cdot \frac{D_h}{L}, \quad (2.11)$$

where  $\Delta p$  is the pressure drop across the structure,  $\rho$  is the fluid density,  $u_{\text{in}}$  is the average inlet velocity,  $D_h$  is the hydraulic diameter, and  $L$  is the streamwise length of the TPMS structure.

The hydraulic diameter  $D_h$  is introduced to generalize the analysis of non-circular or complex internal geometries and is defined as [38]

$$D_h = \frac{4V_{\text{fluid}}}{A_{\text{wetted}}}, \quad (2.12)$$

where  $V_{\text{fluid}}$  denotes the volume occupied by the fluid phase and  $A_{\text{wetted}}$  is the total

solid–fluid interface area, i.e., the wetted surface. This formulation ensures applicability across various structural morphologies, including open-cell TPMS geometries.

For porous media, this expression can be expanded using the Darcy-Forchheimer law [40]

$$\frac{\Delta p}{L} = \frac{\mu}{K} u + \rho \beta u^2, \quad (2.13)$$

to yield the following definition of the friction factor [40]:

$$f = \underbrace{\frac{2D_h^2}{K}}_{C_v} \frac{1}{\text{Re}} + \underbrace{2D_h \beta}_{C_i}, \quad \text{Re} = \frac{\rho u D_h}{\mu}. \quad (2.14)$$

The  $C_v/\text{Re}$  term quantifies the viscous (Darcy) contribution, while  $C_i$  represents the inertial (form-drag) contribution that dominates as  $\text{Re}$  increases. This separation allows a direct assessment of whether viscous or inertial effects control the hydraulic performance of a given TPMS architecture [13].

In this investigation, the pressure drop  $\Delta p$  is obtained from surface-averaged pressure values at designated planes right in front and behind the TPMS structure. The absolute pressure gradient per unit length,  $\Delta p/L$ , is often used as a direct measure of hydraulic resistance, whereas the Darcy friction factor provides a normalized, geometry-independent measure of hydraulic performance.

The overall thermo-hydraulic performance of cellular structures is commonly evaluated using the thermal efficiency index  $\eta$ . This dimensionless parameter, originally introduced by Tian et al. [64], provides a quantitative measure of the trade-off between enhanced heat transfer and the corresponding increase in pressure loss and is defined as [64]

$$\eta = \frac{(Nu/Nu_0)}{(f/f_0)^i}, \quad (2.15)$$

where  $Nu$  and  $f$  are the Nusselt number and friction factor for the tested geometry, respectively, and  $Nu_0$  and  $f_0$  correspond to the values for a reference or baseline configuration. The exponent  $i$  reflects the assumed comparison basis. Three different scenarios are differentiated:  $i = 1/3$  corresponds to constant pumping power,  $i = 1/2$  assumes constant pressure drop, and  $i = 1$  corresponds to constant flow rate. Most previous studies on TPMS-based heat exchangers adopt the constant pumping power assumption, i.e.,  $i = 1/3$ . To facilitate comparison with existing literature, the same assumption is applied in the present study. Hence, a higher value of  $\eta$  indicates a greater improvement in convective heat transfer relative to the associated pressure loss.

The baseline configuration must remain consistent across all tested cases to enable a reliable comparison between different TPMS topologies. To maintain consistency with previous studies, both  $Nu_0$  and  $f_0$  are set to unity, as is commonly done in the literature [3, 29].

## Chapter 3

# Computational Procedure

The present case study is carried out using a numerical approach based on the finite volume method. This method discretizes the computational domain into a finite number of control volumes, over which the governing conservation equations are integrated. Fluxes are evaluated at the surfaces of each control volume to ensure local and global conservation of mass, momentum, and energy. The fluid flow and heat transfer phenomena investigated in this work are governed by the Navier–Stokes equations, which describe the transport of mass and momentum, and the energy equation, which accounts for thermal energy transport. These governing equations are presented below [66].

$$\text{Continuity equation} \quad \frac{\partial u_i}{\partial x_i} = 0, \quad (3.1)$$

$$\text{Momentum equation} \quad \frac{\partial u_i}{\partial t} + u_j \frac{\partial u_i}{\partial x_j} = -\frac{1}{\rho} \frac{\partial p}{\partial x_i} + \frac{\partial}{\partial x_j} \left[ \nu \left( \frac{\partial u_i}{\partial x_j} + \frac{\partial u_j}{\partial x_i} \right) \right] - g_i, \quad (3.2)$$

$$\text{Energy equation} \quad \frac{\partial T}{\partial t} + u_i \frac{\partial T}{\partial x_i} = \frac{\partial}{\partial x_i} \left( \alpha \frac{\partial T}{\partial x_i} \right) + \frac{Q}{\rho c}. \quad (3.3)$$

Since the imposed inlet Reynolds number exceeds the widely accepted threshold for the onset of turbulence in internal pipe flows ( $\text{Re} > 2300$  [38, 66]) and the flow is further disrupted by the intricate geometry of the TPMS structure, the flow within the domain is assumed to be turbulent.

In turbulent flows, kinetic energy is introduced at large scales and then passed down to progressively smaller scales in a process known as the energy cascade. This transfer of energy between scales is primarily driven by the nonlinear advection term in the Navier–Stokes equations,  $u_j \frac{\partial u_i}{\partial x_j}$ , which describes how velocity fluctuations transport and distort the flow, effectively causing the flow to advect itself [58]. Within the so-called inertial range of the cascade, viscous effects are minimal, meaning that energy is neither added nor dissipated, but simply redistributed from larger to smaller flow structures [72].

As energy reaches the smallest turbulent structures, referred to as the Kolmogorov scale, their local Reynolds number approaches unity. At this stage, viscous diffusion becomes dominant and dissipates the remaining kinetic energy into heat. Due to the highly nonlinear coupling introduced by the advection term  $u_j \frac{\partial u_i}{\partial x_j}$ , which links all scales of motion, the prediction of turbulent flows becomes extremely complex [58].

To still accurately account for the influence of turbulence on both fluid flow and heat transfer, a suitable strategy must be adopted to account for the energy cascade within the flowfield. In CFD, three primary approaches exist for simulating turbulent flows: Direct Numerical Simulation (DNS), which resolves the full energy cascade over all turbulent length scales by solving the full unsteady Navier–Stokes equations; Large Eddy Simulation (LES), which captures the larger turbulent structures while modeling the smaller scales;

and Reynolds-Averaged Navier–Stokes (RANS) models, which focus on time-averaged flow behavior and use empirical models to represent turbulence effects [66].

DNS and LES require a high grid resolution, making them highly computationally expensive and therefore not suited for an extensive parametric study. For this reason, the present work employs the RANS approach, which provides a practical balance between predictive capability and computational cost.

### 3.1 Reynolds average Navier Stokes turbulence modelling

The RANS approach is based on the concept of Reynolds decomposition, which separates each instantaneous flow variable into a mean and a fluctuating component as seen below [66]:

$$\begin{aligned} u_i &= \langle u_i \rangle + u'_i \\ p &= \langle p \rangle + p' \\ T &= \langle T \rangle + T' \end{aligned} \quad (3.4)$$

By substituting the Reynolds decomposition into the Navier-Stokes and energy equations (Eq. 3.1) and subsequently applying time-averaging, the RANS equations and the time-averaged energy equation are derived as [72]:

$$\begin{aligned} \frac{\partial \bar{u}_i}{\partial x_i} &= 0, \\ \frac{\partial \bar{u}_i}{\partial t} + \bar{u}_j \frac{\partial \bar{u}_i}{\partial x_j} &= -\frac{1}{\rho} \frac{\partial \bar{p}}{\partial x_i} + \frac{\partial}{\partial x_j} \left[ \nu \left( \frac{\partial \bar{u}_i}{\partial x_j} + \frac{\partial \bar{u}_j}{\partial x_i} \right) \right] - \overline{u'_i u'_j}, \\ \frac{\partial \bar{T}}{\partial t} + \bar{u}_j \frac{\partial \bar{T}}{\partial x_j} &= \alpha \frac{\partial^2 \bar{T}}{\partial x_j^2} - \frac{\partial}{\partial x_j} (\overline{u'_j T'}). \end{aligned} \quad (3.5)$$

It should be noted, that the effect of buoyancy acts as a source term in the energy equation and has no effect on the turbulence modelling. For a more compact representation, buoyancy will be neglected in the bulk of this section and then reintroduced at the end.

In the equation above, the time-averaged quantities are denoted by the overbar. The decomposition and subsequent time averaging introduces the terms  $\overline{u'_i u'_j}$  and  $\overline{u'_j T'}$ , which represent the specific Reynolds stress tensor and turbulent heat flux, respectively. Multiplication of the specific Reynolds stress with the density yields the Reynolds stress tensor  $\rho \overline{u'_i u'_j}$  [72]. This tensor is symmetric and does not represent a true physical stress in the classical sense, rather, it characterizes the mean momentum fluxes induced by turbulent velocity fluctuations. The diagonal components  $\overline{u'_i u'_i}$  are referred to as the normal Reynolds stresses, while the off-diagonal components  $\overline{u'_i u'_j}$  with  $i \neq j$  correspond to the shear Reynolds stresses [66].

The Reynolds-Stress introduces six new unknowns into an otherwise fully defined system of equations. This is known as the closure problem.

To close the system, the Reynolds stress tensor must be modeled. The simplest turbulence models used in the RANS framework employ the Boussinesq eddy viscosity approximation. This is often called a gradient-diffusion approach because turbulent transport of a quantity is assumed to behave on average like molecular diffusion [71]. Hence, the Reynolds stress tensor is modelled as the product of an eddy viscosity  $\nu_\tau$  and the mean strain rate tensor  $S_{ij}$ , such that  $\overline{u'_i u'_j} = \nu_\tau S_{ij} = \nu_\tau \frac{\partial \overline{u_i}}{\partial x_j}$ , which resembles the form of Fick's law of diffusion. Using the trace of the Reynolds stress tensor, defined as the turbulent kinetic energy  $k = \frac{1}{2} \overline{u'_i u'_i}$ , the tensor can be decomposed into isotropic and anisotropic components [72]:

$$\overline{u'_i u'_j} = \frac{2}{3} k \delta_{ij} + a_{ij} \quad (3.6)$$

Assuming the anisotropic part  $a_{ij}$  is directly proportional to the mean strain-rate tensor, the Reynolds stress can be written as follows: [72]:

$$\overline{u'_i u'_j} = \frac{2}{3} k \delta_{ij} - 2\nu_\tau S_{ij} \quad (3.7)$$

By substituting the molecular viscosity with an effective viscosity  $\nu_{\text{eff}} = \nu + \nu_\tau$ , and incorporating this into the RANS equations, the modified momentum equation can be derived[72]:

$$\frac{D\overline{u_i}}{Dt} = -\frac{1}{\rho} \frac{\partial}{\partial x_i} \left( \overline{p} + \frac{2}{3} \rho k \right) + \frac{\partial}{\partial x_j} \left[ \nu_{\text{eff}} \left( \frac{\partial \overline{u_i}}{\partial x_j} + \frac{\partial \overline{u_j}}{\partial x_i} \right) \right] \quad (3.8)$$

This equation resembles the form of the laminar Navier–Stokes equations, with the mean velocity  $\overline{u_i}$  and effective viscosity  $\nu_{\text{eff}}$  replacing their instantaneous counterparts, and a modified pressure  $\overline{p} + \frac{2}{3} \rho k$ . Together with the continuity equation, this forms a closed set of equations that can be numerically solved.

However, the assumption that the Reynolds stress  $\overline{u'_i u'_j}$  is linearly proportional to the mean strain-rate  $S_{ij}$  introduces symmetry constraints. Specifically, it predicts [72]:

$$\overline{u' u'} = \overline{v' v'} = \overline{w' w'} = \frac{2}{3} k \quad (3.9)$$

This result of the eddy viscosity model contradicts DNS data, which shows that the stream-wise normal stress  $\overline{u' u'}$  in a plane channel flow exhibits a maximum near the wall region that is considerably higher than the peaks of the wall-normal stress  $\overline{v' v'}$  and the spanwise normal stress  $\overline{w' w'}$  [72]. Another problem arising with this model is the determination of  $\nu_\tau$ , since it is not a fluid property, but depends on the turbulent velocity scale  $v_\tau$  and turbulent length scale  $l_\tau$ .

To overcome the shortcomings of the linear eddy-viscosity hypothesis and the ad-hoc nature of the turbulent viscosity  $\nu_t$ , modern RANS closures generally use non-linear eddy viscosity models. The most common non linear models are two-equation models, which use differential transport equations to estimate the turbulent scales [66]. They estimate the turbulent velocity scale  $v_\tau$  using the turbulent kinetic energy  $k$ , while the length scale  $l_\tau$  is estimated through the dissipation rate  $\epsilon$  or the dissipation rate per unit of turbulent kinetic energy  $\omega = \epsilon / (k\beta^*)$  [72]:

$$v_\tau \approx k^{1/2}, \quad l_\tau \approx \frac{k^{3/2}}{\epsilon}, \quad l_\tau \approx \frac{\sqrt{k}}{\omega} \quad (3.10)$$

### 3.1.1 The $k - \epsilon$ and $k - \omega$ model

The two most widely used two-equation RANS turbulence models are the  $k - \epsilon$  introduced by Jones et al. [27] in 1972 and  $k - \omega$  model introduced by Willcox et al. [71] in 1988, each of which solves two additional transport equations: one for the turbulent kinetic energy  $k$  and one for the dissipation,  $\epsilon$  in the  $k - \epsilon$  formulation or  $\omega$  in the  $k - \omega$  formulation. These transport equations are derived from the instantaneous NS-equation and the RANS-equations as seen in Appendix A.2.

$$\begin{aligned} \frac{\partial k}{\partial t} + U_j \frac{\partial k}{\partial x_j} &= P_k - \epsilon + \frac{\partial}{\partial x_j} \left[ \left( \nu + \frac{\nu_t}{\sigma_k} \right) \frac{\partial k}{\partial x_j} \right], \\ \frac{\partial \epsilon}{\partial t} + U_j \frac{\partial \epsilon}{\partial x_j} &= C_{1\epsilon} \frac{\epsilon}{k} P_k - C_{2\epsilon} \frac{\epsilon^2}{k} + \frac{\partial}{\partial x_j} \left[ \left( \nu + \frac{\nu_t}{\sigma_\epsilon} \right) \frac{\partial \epsilon}{\partial x_j} \right], \\ \frac{\partial \omega}{\partial t} + U_j \frac{\partial \omega}{\partial x_j} &= \alpha \frac{\omega}{k} P_k - \beta^* \omega^2 + \frac{\partial}{\partial x_j} \left[ \left( \nu + \frac{\nu_t}{\sigma_\omega} \right) \frac{\partial \omega}{\partial x_j} \right]. \end{aligned}$$

where

$$P_k = \nu_t \frac{\partial U_i}{\partial x_j} \frac{\partial U_i}{\partial x_j}$$

is the production of turbulent kinetic energy by mean-flow shear.

Here the symbols  $\sigma_k$ ,  $\sigma_\epsilon$ ,  $\sigma_\omega$ ,  $C_{1\epsilon}$ ,  $C_{2\epsilon}$ ,  $\alpha$ , and  $\beta^*$  denote empirical coefficients calibrated against turbulent-flow experiments [72].

As shown, the principal distinction between the two models lies in their treatment of the dissipation of turbulent kinetic energy, which results in two different expressions to estimate the  $\nu_\tau$  [72].

$$\nu_t = C_\mu \frac{k^2}{\epsilon}, \quad \nu_t = \frac{k}{\omega} \quad (3.11)$$

Here,  $C_\mu$  is another dimensionless empirical constant, that is most commonly calibrated as  $C_\mu = 0.09$  [72].

In the  $k - \epsilon$  model the transport equation for  $\epsilon$  (see (3.1.1)) contains the production–dissipation term

$$- C_{2\epsilon} \frac{\epsilon^2}{k}$$

which, as  $k \rightarrow 0$  near a no-slip wall, becomes numerically stiff and unbounded, which would lead to a blowup of  $\nu_\tau$  (see 3.1.4). To maintain stability one must either invoke empirical wall-functions or introduce artificial damping of the  $\epsilon$ -equation. Both approaches alter the true balance of turbulent kinetic energy and dissipation in the buffer and log layers, typically leading to an overprediction of the eddy viscosity in those regions [72].

Far from solid boundaries, however, the  $k - \epsilon$  closure “self-corrects” any inlet–boundary

mismatch in  $\epsilon_\infty$  through its linear production–dissipation balance

$$C_{1\epsilon} \frac{\epsilon}{k} P_k - C_{2\epsilon} \frac{\epsilon^2}{k}$$

and its relatively strong turbulent diffusion term  $\partial_j[(\nu + \nu_t/\sigma_\epsilon) \partial_j \epsilon]$  with  $\sigma_\epsilon \approx 1.3$  [72]. These mechanisms act together to restore the equilibrium  $P_k \approx \epsilon$  within a few boundary-layer thicknesses, so that the algebraic ratio  $k^2/\epsilon$  remains physically realistic in the free stream.

By contrast, the  $k-\omega$  model more accurately predicts boundary-layer turbulence, because its transport equation (3.1.1) remains finite as  $k \rightarrow 0$  [72]. Further from the wall, however, the  $k-\omega$  model often underpredicts turbulent mixing because it is directly set by the freestream boundary condition  $\omega_\infty$ . Since the  $\omega$ -equation (3.1.1) features relatively weak turbulent diffusion ( $\sigma_\omega \approx 0.5$ ) and a quadratic sink  $-\beta^* \omega^2$ , any error in  $\omega_\infty$  persists downstream [72]. This directly translates to  $\nu_t$  and thus often underestimates turbulent dissipation and mixing in the outer region.

### 3.1.2 The Shear-Stress Transport $k-\omega$ model

A model that incorporates both the strength of  $k-\omega$  at the walls and the robustness of  $k-\epsilon$  in free-stream, was introduced by Menter et al. [33] in 1994. This so-called Shear-Stress Transport (SST)  $k-\omega$  model is a hybrid model, which blends the transport equations for  $\epsilon$  and  $\omega$  together using the blending function  $F_1$  [33]:

$$\frac{\partial \omega}{\partial t} + \bar{u}_j \frac{\partial \omega}{\partial x_j} = \alpha \frac{\omega}{k} P_k - \beta \omega^2 + \frac{\partial}{\partial x_j} \left[ (\nu + \sigma_\omega \nu_t) \frac{\partial \omega}{\partial x_j} \right] + 2(1 - F_1) \frac{\sigma_{\omega 2}}{\omega} \frac{\partial k}{\partial x_j} \frac{\partial \omega}{\partial x_j}, \quad (3.12)$$

In different CFD codes the blending function may vary slightly in its exact form, but it is always constructed so that  $F_1 = 1$  at the wall and  $F_1 = 0$  in the freestream. The role of  $F_1$  is not only, to gate the cross-diffusion term  $\frac{\sigma_{\omega 2}}{\omega} \frac{\partial k}{\partial x_j} \frac{\partial \omega}{\partial x_j}$  but also to interpolate each turbulence-model coefficient  $\Phi \in \{\alpha, \beta, \beta^*, \sigma_k, \sigma_\omega\}$  between its near-wall value  $\Phi_1$  and its freestream value  $\Phi_2$  via the relation [72]

$$\Phi = F_1 \Phi_1 + (1 - F_1) \Phi_2 \quad (3.13)$$

This blending of the wall-resolving accuracy of  $k-\omega$  with the free-stream robustness of  $k-\epsilon$ , the SST  $k-\omega$  model delivers the fine near-wall resolution and stable outer-flow behavior required to predict the thermo-hydraulic performance of TPMS structures, where tight curvature, repeated separation and reattachment, and localized heat-flux gradients demand both precision and numerical reliability.

### 3.1.3 The Reynolds-averaged temperature equation

Similarly to the Reynolds stresses, a model equation for the turbulent heat flux  $\overline{u'_j T'}$  in equation 3.1 can be formulated using the gradient-diffusion hypothesis where [72]:

$$\overline{u'_j T'} \approx -\alpha_\tau \frac{\partial \bar{T}}{\partial x_j} \quad (3.14)$$

where  $\alpha_\tau$  is the turbulent thermal diffusivity. Inserting this into the turbulent energy equation yields

$$\frac{\partial \bar{T}}{\partial t} + u_j \frac{\partial \bar{T}}{\partial x_j} = \frac{\partial}{\partial x_j} \left[ (\alpha + \alpha_t) \frac{\partial \bar{T}}{\partial x_j} \right] \quad (3.15)$$

Using the assumption, that turbulent eddies transport heat and momentum by the same physical mechanism the system can be closed by relating the turbulent thermal diffusivity to the turbulent viscosity using the empirically found turbulent Prandtl number ( $Pr_\tau$ ),

$$\alpha_\tau = \frac{\nu_\tau}{Pr_\tau} \quad (3.16)$$

and thereby closing the aforementioned system of governing equations for turbulent flow and heat transfer [72].

### 3.1.4 Wall treatment

The described system accurately captures the flow behavior across most of the domain. However, additional considerations are necessary near the walls to ensure physically accurate results. A wall in turbulence modeling is generally defined as a non-permeable surface, where the mean velocity goes down to zero (no-slip). This no-slip and non-permeability condition impose very steep velocity gradients and hence very high shear stresses right at the boundary, which any turbulence closure must either resolve or model.

The velocity profile adjacent to solid walls can be divided into three regions, the viscous sublayer, buffer layer, and logarithmic (log) layer, each characterized by the balance of the stress tensor [71].

$$\tau_{ij} = \mu \frac{\partial \bar{u}_i}{\partial x_j} + \rho \overline{u'_i u'_j} \quad (3.17)$$

where  $\frac{\partial \bar{u}_i}{\partial x_j}$  describes the viscous stresses and  $\rho \overline{u'_i u'_j}$  the turbulent stresses. Close to the wall  $\tau_{ij}$  is called wall shear stress and generally denoted as  $\tau_w$ . To get a universal description of the wall effects the dimensionless wall coordinates  $y^+$  and  $u^+$

$$y^+ = \frac{u_\tau y}{\nu}, \quad u^+ = \frac{\bar{u}}{u_\tau}. \quad (3.18)$$

where  $u_\tau = \sqrt{\tau_w / \rho}$  [72]. Using the dimensionless distance  $y^+$  the different boundary regions can be quantified as follows

**Viscous Sublayer ( $y^+ < 5$ )** The viscous sublayer is defined as the region where the viscous stress dominates over the turbulent stress, leading to the local Reynolds number  $Re_\tau = (u_\tau y / \mu)$  dropping below 5 [72]. Consequently the wall shear stress can be simplified to

$$\tau_{ij} = \mu \frac{\partial \bar{u}_i}{\partial x_j} \quad (3.19)$$

This can be rearranged and integrated to get

$$\bar{u} = \frac{\tau_w}{\mu} y = u_\tau^2 \frac{y}{\nu} \quad (3.20)$$

Using the definition for  $u^+$  and  $y^+$  the velocity profile can be written in non-dimensional as

$$u^+ = y^+ \quad (3.21)$$

Hence, the velocity in the viscous sublayer depends linearly on the distance to the wall [72].

**Log-Layer** ( $30 \leq y^+ \leq 200$ ) In contrast to the viscous sublayer, the log-layer is dominated by inertial forces ( $Re_\tau \sim 30 - 200$ ), leading to the turbulent stress dominating over the viscous stress [72]. Using the same method as for the viscous sublayer, and the gradient diffusion hypothesis to estimate the Reynolds stresses ( $\overline{u'_i u'_j} \approx \nu_\tau \bar{u}/dy$ ), the dimensionless velocity profile in the log-layer can be estimated to [72]:

$$u^+ = \frac{1}{\kappa} \ln(y^+) + B \quad (3.22)$$

These two estimates for the unitless velocity profile close two the wall can be seen in Figure 3.1, plotted against experimental data.

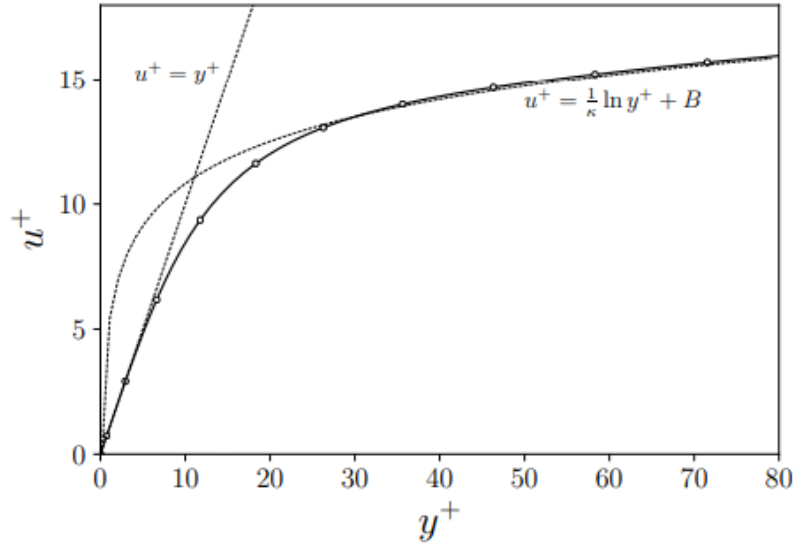


**Figure 3.1:** Law of the Wall taken with consent from a lecture held by Sandro Manservigi on turbulence modelling [65]

It can be seen, that the estimated velocity profiles follow the actual velocity profile very closely in their designated regions. A high deviation however can be seen in the in-between region, called the buffer-layer ( $5 < y^+ < 30$ ).

This unpredictable nature of the velocity in the buffer-layer, makes it unsuited for the position of the first grid point, since the velocity can neither be fully resolved (linear region) or estimated (logarithmic region). Therefore, it is good practice in CFD simulations involving RANS-turbulence modelling to either set the first cell-center in the viscous-sublayer or log-layer. The same applies for temperature profile, which for a constant Prantl Number follows similar formulations as the velocity close to the wall- linear for  $y^+ < 5$  and logarithmic for  $30 \leq y^+ \leq 200$  [72].

For this study, the accurate prediction of fluid property gradients at the wall is essential, since two evaluation criteria, namely the pressure drop and the Nusselt number, depend directly on the velocity gradient and the temperature gradient at the wall, respectively. To fully resolve these gradients, the first grid point for all walls is set in the region of  $y^+ < 1$ , which lies deep within the viscous sublayer.

## 3.2 Boundary treatment

To solve the system of governing equations, additional constraints must be imposed, without which the Navier–Stokes equations (or any partial differential equation) would be ill-posed and therefore unsolvable [66]. These constraints are provided by the problem’s boundary and initial conditions. For a scalar field  $\phi$  defined on a domain  $\Omega$ , the boundary conditions imposed on its boundary  $\partial\Omega$  are generally classified into two main types[37]:

1. **Dirichlet boundary condition**, which prescribes the value of the field itself at the boundary:

$$\phi|_{\partial\Omega} = \phi_0.$$

Physically, this fixes the variable (e.g. temperature, velocity component) to a known profile or constant. In OpenFOAM this is implemented via the `fixedValue` condition.

2. **Neumann boundary condition**, which prescribes the normal gradient (flux) of the field at the boundary:

$$\frac{\partial\phi}{\partial n}\bigg|_{\partial\Omega} = q_0,$$

where  $\frac{\partial}{\partial n} = \mathbf{n} \cdot \nabla$  denotes differentiation in the outward-pointing normal direction  $\mathbf{n}$ . Setting  $q_0 = 0$  corresponds to zero flux (insulating or outflow), implemented in OpenFOAM as `zeroGradient`. Non-zero fixed fluxes can be imposed via `fixedGradient`.

These formulations extend directly to vector fields, such as the velocity  $\mathbf{u}$ , by enforcing the Dirichlet or Neumann condition independently on each component of the vector [37].

On the sides of the domain, a periodic boundary condition is implemented, which does not fall neatly into the Dirichlet or Neumann categories, but rather is a mix of both [47]. It imposes value continuity (Dirichlet-type), in that the field on one side of the interface is set equal to the interpolated value on the opposing patch. In other words,

$$\phi_{\text{patch A}} = \mathcal{I}[\phi_{\text{patch B}}],$$

where  $\mathcal{I}$  is the chosen AMI (Arbitrary Mesh Interface) interpolation operator [47]. However, the cyclic boundary condition also imposes flux consistency (Nuemann-type). Here, the normal gradient (or flux) across the interface is evaluated consistently using the same interpolation weights, so that no artificial jump appears in the diffusive (or convective) flux [47].

The initial conditions implemented, are mathematically not strictly necessary to solve a steady state problem, since it is fully posed by just its boundary conditions. Numerically, however, the iterative linear and non-linear solvers require a starting guess. Hence, the initial conditions in study should rather be seen as a first guess, from where the solver starts marching towards a steady solution, than initial conditions in the conventional temporal sense.

### 3.3 Simulation Setup

Previous sections went into detail on the techniques applied to solve the Navier Stokes equations for turbulent flow in both the free stream and the near wall regions. This section will summarize the applied methods and describe how they are implemented.

All computational work in this thesis is carried out using the open-source CFD toolbox OpenFOAM [70].

#### Turbulence Model

The cases are simulated as steady state, which requires a RANS-turbulence model. The  $k - \omega$  SST model is chosen because it combines the ability to accurately resolve the near-wall boundary layer while still maintaining stability and accuracy in the outer flow region. The standard model coefficients provided by OpenFOAM are chosen. These are shown in Table 3.1.

**Table 3.1:** SST  $k-\omega$  model coefficients

Coefficient	Value
$\alpha_{k1}$	0.85
$\alpha_{k2}$	1
$\alpha_{\omega1}$	0.5
$\alpha_{\omega2}$	0.856
$\gamma_1$	0.555556
$\gamma_2$	0.44
$\beta_1$	0.075
$\beta_2$	0.0828
$\beta^*$	0.09
$a_1$	0.31
$b_1$	1
$c_1$	10

### Discretization Schemes

The governing equations (see Equation 3.1) are discretized via the finite-volume method using Gauss's divergence theorem, and further individual discretization for the convective fluxes and diffusive fluxes. Wherever the mesh quality and flow gradients permit, fully second-order methods are employed. However, in regions prone to instability or oscillations, limited or bounded variants are substituted to preserve stability. A complete overview of the employed discretization schemes is given in Table 3.2. Furthermore a more detailed description of the employed numerical methods is given in Appendix A.3.

**Table 3.2:** Summary of discretization schemes

Category	Scheme	Accuracy	Boundedness
Gradient schemes	cell-limited linear	second-order accurate	limited
Divergence schemes	upwind	first-order accurate	bounded
	limited linear	first- to second-order accurate	regionally bounded
Laplacian scheme	linear corrected	second-order accurate	non-orthogonality corrected
Interpolation scheme	linear	second-order accurate	unbounded

### Solver

In this simulation, the incompressible formulation for the Navier stokes equations and the energy equations need to be solved for a steady state. For this, the SIMPLE solver is chosen, which iteratively solves the non-definite linear system by splitting it into a predictor and corrector loop. One big advantage of the SIMPLE solver is the ability to under-relax the flow fields, and thereby smoothen out oscillations or instabilities, that could otherwise diverge the simulation. The values for the relaxation factor are shown in Table 3.3. A more detailed of this solver can be found in Appensix A.4.

**Table 3.3:** Relaxation factors used in the SIMPLE solver.

Variable	Relaxation Factor
$p$	0.20
$U$	0.50
$T$	0.40
$k$	0.30
$\omega$	0.30

The relaxation factors were set to rather conservative values, to get good convergence even in complex turbulent flow fields such as the one induces by TPMS structures.

### Boundary and Initial Conditions

The boundary conditions must reproduce the actual physics at each surface. Accordingly, at the inlet a fixed velocity of 3.7 m/s and a fixed temperature of 298 K are prescribed, while the pressure is left as zero-gradient so that it can adjust to the imposed flow. The turbulent quantities are set using algebraic equations. The relation

$$k = \frac{3}{2} (|u| I)^2 \quad (3.23)$$

is used to estimate the turbulent kinetic energy at the inlet [19]. Here,  $u$  is the imposed inlet velocity, and  $I \approx 0.16 Re^{-1/8}$  is the specific turbulent intensity. The specific dissipation rate can be estimated using the local  $k$  and the turbulent mixing length  $l_m \approx 0.07D_h$  as follows:

$$\omega = \frac{\sqrt{k}}{C_\mu^{1/4} \ell} \quad \text{with} \quad C_\mu = 0.09$$

In OpenFOAM, these relations can be implemented directly as the boundary conditions "turbulentIntensityKineticEnergyInlet" for  $k$  and "turbulentMixingLengthFrequencyInlet" for  $\omega$ . The turbulent viscosity  $\nu_\tau$  and turbulent thermal diffusivity  $\alpha_\tau$  can be calculated using  $k$  and  $\omega$ , as described in Section 3.1.

At the outlet, standard outflow boundary conditions are imposed. The pressure is fixed at a reference value of zero (arbitrary for incompressible flow), and all other flow and turbulence variables are assigned zero-gradient conditions to allow their profiles to adjust freely.

The side faces are set to have a cyclic boundary condition, which leads to the previously described periodic flow behaviour. The TPMS structure is treated as a wall. Hence, for the velocity a no-slip condition ( $u_{wall} = 0$ ) is imposed. The temperature is set to have a fixed value of 353 K, and the pressure is set to zero gradient. A special treatment is implemented for the turbulent properties  $k$  and  $\omega$ , due to some mesh refinement issues close to the boundary, where some cells exceed  $y^+ = 1$  (see Chapter 4).

To still accurately capture near-wall turbulence, low-Reynolds-number wall functions are implemented for the turbulent kinetic energy  $k$  and specific dissipation rate  $\omega$ . These wall functions enforce the correct asymptotic behavior,

$$\lim_{y^+ \rightarrow 0} k = 0, \quad \lim_{y^+ \rightarrow 0} \omega = \infty,$$

while avoiding under- or over-prediction of turbulent quantities in the few cells for which  $y^+$  exceeds the nominal value of unity. The implemented  $k$ -Wallfunction is formulated as

$$k_{\text{branch}} = \begin{cases} k_{\text{vis}} = \frac{2400 C_f}{C_{\epsilon 2}^2}, & y^+ \leq y_{\text{lam}}^+ \\ k_{\text{log}} = \frac{C_k \ln(y^+)}{\kappa} + B_k, & y^+ > y_{\text{lam}}^+ \end{cases}$$

where  $y_{\text{lam}}^+$  defines the region of the viscous sublayer, where the flow is assumed to be laminar, and in OpenFOAM is set to  $y_{\text{lam}}^+ \approx 10$  [45]. In this study, care is taken, to ensure that even the large boundary layer cells, would not breach  $y^+ \leq 5$ , and therefore still lie in the laminar region. For  $k_{\text{vis}}$  the skin-friction coefficient  $C_f$  is computed as a function of  $y^+$  (and the switch-over constant  $C = y_{\text{lam}}^+ \approx 10$ ) by

$$C_f = \frac{1}{(y^+ + C)^2} + \frac{2y^+}{C^3} - \frac{1}{C^2},$$

so that  $C_f \rightarrow 0$  quadratically as  $y^+ \rightarrow 0$ . Finally, the viscous-sublayer estimate of  $k$  uses

the the second dissipation coefficient in the standard  $k-\epsilon$  model  $C_{\epsilon 2}$ , which is typically set to  $C_{\epsilon 2} \approx 1.92$ .

Similarly to to the  $k$ -Wallfunction, the  $\omega$ -Wallfunction is also divided based on the boundary regions [46]:

$$\omega_{\text{branch}} = \begin{cases} \omega_{\text{vis}} = \frac{6 \nu_w}{\beta_1 y^2}, & y^+ \leq y_{\text{lam}}^+, \\ \omega_{\text{log}} = \frac{\sqrt{k}}{C_\mu \kappa y}, & y^+ > y_{\text{lam}}^+. \end{cases}$$

Here, also only the viscous formulation is relevant since no cell breaches the  $y^+ = 10$  threshold. In this expression,  $\nu_w$  denotes the kinematic viscosity evaluated at the wall and  $\beta_1$  is the first dissipation-rate coefficient in the  $k-\omega$  model (typically  $\beta_1 \approx 0.075$ ). This formulation also enforces the near-wall asymptote  $\omega \sim 1/y^2$ , which guarantees that  $\omega \rightarrow \infty$  as the wall is approached. The turbulent viscosity  $\nu_\tau$  and thermal diffusivity  $\alpha_\tau$  are calculated based on  $k$  and  $\omega$  as described in section 3.1.

On the side walls, a cyclic arbitrary mesh interface (`cyclicAMI`) boundary condition is implemented using a face area weight interpolation method [47]. For each face  $f_A$  on patch A, this algorithm identifies all faces  $f_B$  on patch B whose bounding boxes overlap. It then computes the intersection polygon  $P_{AB}$  between the two faces and measures its area  $A_{AB}$  [48].

The field value on face  $f_A$  of patch A is reconstructed by area-weighted interpolation from the overlapping faces  $f_B$  on patch B:

$$\phi(f_A) = \sum_{f_B} \underbrace{\frac{A_{AB}}{A_A}}_{w_{AB}} \phi(f_B),$$

where

$$w_{AB} = \frac{A_{AB}}{A_A} \quad \text{and} \quad \sum_{f_B} w_{AB} = 1.$$

Here  $A_{AB}$  is the intersection area between  $f_A$  and  $f_B$ , and  $A_A$  is the total area of face  $f_A$ . The interpolation weights  $w_{AB}$  therefore represent the fraction of face  $f_A$ 's area contributed by each overlapping face  $f_B$ . All the implemented boundary conditions are summarized in Table 3.4

**Table 3.4:** Boundary conditions

Field	inlet	outlet	TPMS	side Faces
U	fixedValue 3.7 m/s	zeroGradient	noSlip	cyclicAMI
p	zeroGradient	fixedValue 0	zeroGradient	cyclicAMI
T	fixedValue 298 K	zeroGradient	fixedValue 353 K	cyclicAMI
$\alpha_\tau$	calculated	zeroGradient	calculated	cyclicAMI
k	turbulentIntensityInlet	zeroGradient	kLowReWallFunction	cyclicAMI
$\nu_\tau$	calculated	zeroGradient	calculated	cyclicAMI
$\omega$	turbulentMixingLengthInlet	zeroGradient	omegaWallFunction	cyclicAMI

Unlike in fully transient simulations, where initial internal conditions specify the field at time zero, in steady state solvers they serve as a starting estimate of the final converged solution. A poor guess can cause the simulation to diverge, so selecting reasonable initial values for all variables is crucial, especially for the turbulence fields. In general the inlet conditions for the internal domain were used as a first guess for most parameters, except  $p$ , which was set to the reference pressure (0 in this case). Furthermore, the initial internal fields for  $\alpha_\tau$  and  $\nu_{tau}$  are calculated based on the field values of  $k$  and  $\omega$  (see Equations 3.3 and 3.3).

#### Performance evaluation

Performance is evaluated based on the friction factor, the pressure drop per unit length, and the Nusselt number (see Section 2.2). The thermophysical properties of air are determined using a lookup table, based on the temperature of the first grid point. This is implemented by extending the `boyantBussenesqueSimpleFoam` solver as shown in Appendix A.6

The pressure drop per unit length is defined as the difference in total pressure in front and behind the TPMS structure, where each total pressure is obtained by averaging across the cross-sectional plane immediately upstream and downstream of the porous domain. This averaging procedure normalizes differences in cross-sectional area, enabling direct comparison of pressure drops and subsequently also the friction factor across all cases.

## Chapter 4

# Computational Mesh

In computational fluid dynamics, the mesh (or grid) is the spatial discretization of the domain into a finite number of small, non-overlapping elements (cells or control volumes) on which the governing equations are solved. Therefore, a good mesh is the backbone of any CFD simulation. Mesh quality depends on several factors, including the shape and size of individual cells, the conformity and connectivity between neighboring cells, their alignment with key flow directions, and their overall compatibility with the chosen numerical methods. To systematically quantify these aspects, several mesh-quality metrics are used.

### 4.1 Mesh-Quality Metrics

Mesh quality can be classified according to the geometric integrity of individual cells, such as skewness or aspect ratio, and the mesh's ability to capture case-specific features, such as boundary-layer refinement or gradient resolution. Cell geometry significantly influences the accuracy and stability of the numerical schemes used to solve the governing equations. Consequently, geometric metrics such as skewness, non-orthogonality, aspect ratio, and growth ratio must be evaluated. Some of the most important metrics are summarized below. It should be noted that this study employs a mostly hexahedral mesh, so the following quality metrics are presented in that context. The same metrics, however, can be adapted to triangular, quadrilateral, or other cell shapes by using the corresponding geometric definitions.

#### Skewness

The skewness of a mesh element quantifies its deviation from an ideal shape. Generally, skewness is measured by the displacement between the actual face centroid and the ideal interpolation point: for a face shared by two cells, let  $\mathbf{f}$  be the true face centroid and  $\mathbf{f}'$  the point where the line connecting the cell centers  $\mathbf{c}_P$  and  $\mathbf{c}_N$  intersects the face plane [66]. The centroid-based skewness is then

$$S_{\text{cent}} = \|\mathbf{f} - \mathbf{f}'\|.$$

In OpenFOAM, this is normalized by cell center spacing, defining face skewness as [49]

$$S_{\text{skew}} = \frac{\|\mathbf{f} - \mathbf{f}'\|}{\|\mathbf{c}_N - \mathbf{c}_P\| + \text{VSMALL}},$$

where VSMALL is a small constant to avoid division by zero. However, due to the way OpenFOAM computes both cell centers and face centroids, the ideal intersection point  $\mathbf{f}'$  does not coincide exactly with the face centroid  $\mathbf{f}$ . In practice, this yields  $\|\mathbf{f} - \mathbf{f}'\| \approx \|\mathbf{c}_N - \mathbf{c}_P\|$ , so that even a perfect hexahedral mesh reports  $S_{\text{skew}} \approx 1$ .

A high face skewness degrades interpolation accuracy by displacing the face centroid from its ideal location, thereby introducing truncation errors proportional to the skewness. It also misaligns the face-area vector  $\mathbf{S}_f$  in Gauss's theorem, necessitating larger non-orthogonal correction terms that increase computational cost and can lead to instability. Thus, in OpenFOAM, it is recommended to maintain internal face skewness below 4, while allowing boundary face skewness up to 7 [11, 41].

### Non-Orthogonality

A closely related metric is the non-orthogonality. In contrast to skewness, which measures the positional deviation of a face centroid from its ideal interpolation point, non-orthogonality quantifies the angular deviation between the normal vector of a face and the line that connects the centers of its adjacent cells, effectively measuring how far the mesh departs from the perfect right angles [66].

In OpenFOAM, this is computed for each internal face by letting  $\mathbf{d} = \mathbf{c}_N - \mathbf{c}_P$  denote the vector between the two cell centers and  $\mathbf{S}_f$  the face-area vector, then evaluating [49]

$$\theta_f = \cos^{-1} \left( \frac{\mathbf{d} \cdot \mathbf{S}_f}{\|\mathbf{d}\| \|\mathbf{S}_f\| + \text{VSMALL}} \right) \quad (\text{degrees}).$$

A perfectly orthogonal mesh has  $\theta_f = 0^\circ$ . As  $\theta_f$  increases, larger non-orthogonal correction terms are required in the discretization of diffusion and gradient operators, which degrades formal accuracy, raises computational cost, and may impair solver convergence. While angles up to  $70^\circ$  are deemed acceptable, it is best practice to maintain  $\theta_f \lesssim 65^\circ$  for reliable CFD results [11, 41].

### Aspect Ratio

The aspect ratio of a cell describes the ratio between its longest and shortest characteristic lengths. A low aspect ratio (close to unity) indicates a nearly isotropic cell, whereas a high aspect ratio denotes a stretched or elongated element.

Numerically, very elongated cells cause the finite-volume discretisation to become highly anisotropic. This leads to central-difference approximations of gradients along the long dimension suffering large truncation errors, thereby smearing out features aligned with the stretch and under-resolving gradients across it [11]. This imbalance can also produce coefficient matrices with widely varying diagonal and off-diagonal entries. The resulting ill-conditioning forces tighter under-relaxation or more inner-loop iterations and can cause divergence in extreme cases [11].

As a general rule of thumb, cells in the bulk flow should maintain an aspect ratio below 10 : 1 to avoid numerical anisotropy and ill-conditioning of the linear system [37]. However, boundary-layer cells may safely reach aspect ratios of 50 : 1 when their long axis is aligned with the wall-normal direction, since this alignment preserves accuracy, while satisfying the  $y^+$  requirements [41].

### Growth Ratio

The growth ratio measures how rapidly cell sizes change from one layer to the next. It is

most commonly defined on a face-by-face basis as

$$G_f = \frac{\max(V_P, V_N)}{\min(V_P, V_N)},$$

where  $V_P$  and  $V_N$  are the volumes (or characteristic lengths) of the two cells sharing face  $f$  [49]. High growth ratios amplify truncation errors by forcing interpolations and gradient estimates across uneven cell sizes, which smears sharp features and can induce oscillations. They also worsen matrix conditioning, creating stiff linear systems in implicit or steady solvers, which can slow down convergence or cause divergence [38]. Therefore, growth ratios between adjacent cells should be kept below 2 [41]

The case specific quality features can be broken down into the choice of the cell type and the specific boundary features that the grid must exhibit, to fulfill the requirements of the chosen modelling approach.

Grids are generally classified as either structured, in which cells are arranged in a regular Cartesian topology, or unstructured, in which cells connect in an arbitrary pattern using elements such as triangles, tetrahedra, or other polyhedra [66]. Structured grids provide high computational efficiency because the alignment of cell faces with the coordinate axes eliminates the need for face-normal corrections, and they deliver excellent numerical accuracy when those faces are aligned with the flow direction [66].

On the other hand, unstructured grids require explicit storage of cell-to-cell connectivity in additional data tables, which increases both memory usage and computational cost [41]. However, their flexibility allows seamless adaptation to complex geometries, which is one of the main disadvantages of structured grids.

Consequently, a hybrid meshing strategy was adopted, where the bulk flow region is discretized with a structured hexahedral grid, while tetrahedral cells are used close to the TPMS structure to capture its complex geometry.

As described in Section 3.1, the wall-resolved  $k-\omega$  SST model is used to simulate turbulence effects in the flow. This model requires the first grid point to lie within the viscous sublayer ( $y^+ < 5$ ). Furthermore, to resolve the steep velocity and thermal gradients near the wall, several finely spaced boundary-layer cells are employed, with the first cell satisfying  $y^+ \leq 1$ . Here, the general rule of thumb is to have 10 – 15 cells with growth ratios below 1.3 within the boundary layer [41].

## 4.2 Mesh Generation

Four open source mesh generators were tested for this study: cfMesh, snappyHexMesh, Gmsh and SALOME Meca. Gmsh and SALOME Meca were unable to import and heal the highly detailed STL files needed to resolve the TPMS curvature and were therefore excluded. Both cfMesh and snappyHexMesh successfully handled the geometry and generated prism cells along the walls, but cfMesh could not maintain the required mesh quality while also achieving the fine first layer thickness needed for  $y^+ \leq 1$ . Hence, snappyHexMesh [50] was

chosen as the meshing tool for this thesis.

In this section, the meshing procedure will be demonstrated based on the base case 10G. However, the same meshing strategy is also applied to all other cases. Therefore, everything explained in this section accounts for all cases, except specifically stated otherwise.

SappyHexMesh generates the mesh in three sequential stages. During castellation, the background Cartesian grid is locally refined around the imported STL file by subdividing any intersecting cells to the user-specified refinement level. In the snapping phase, the vertices are projected onto the exact surface triangles, smoothing the staircase approximation while preserving the cell connectivity created during castellation. Finally, boundary-layer cells are formed by extruding prism layers normal to the wall according to the specified layer count, [50]. These steps are controlled in the so-called `sappyHexMeshDict`, which defines the parameters for each step. The dict file in this study is kept the same for all the cases, and is included in Appendix A.5. The mesh generated in `sappyHexMesh` for the 10G structure is shown in Figure 4.1.

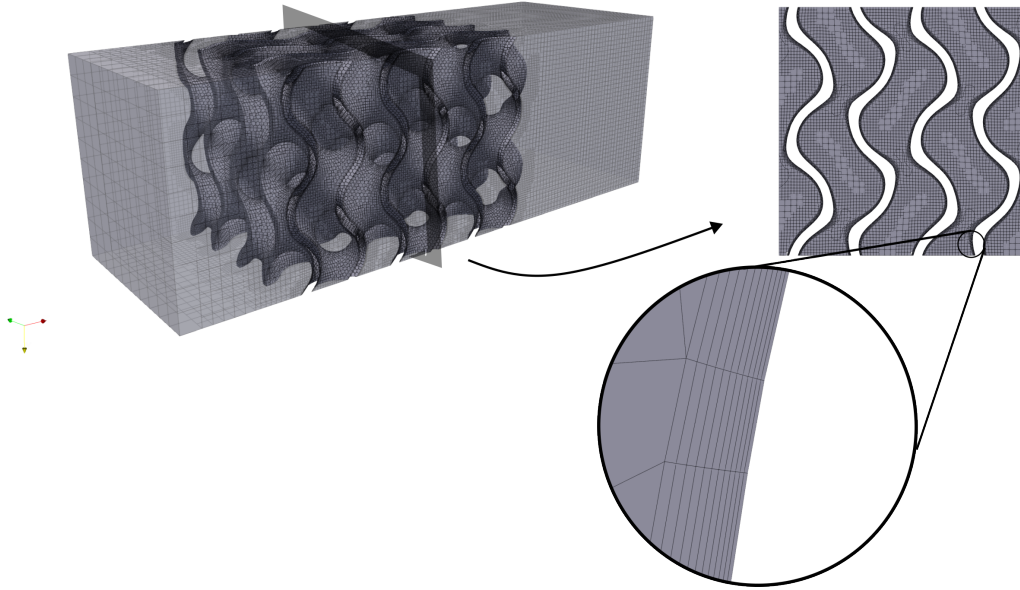


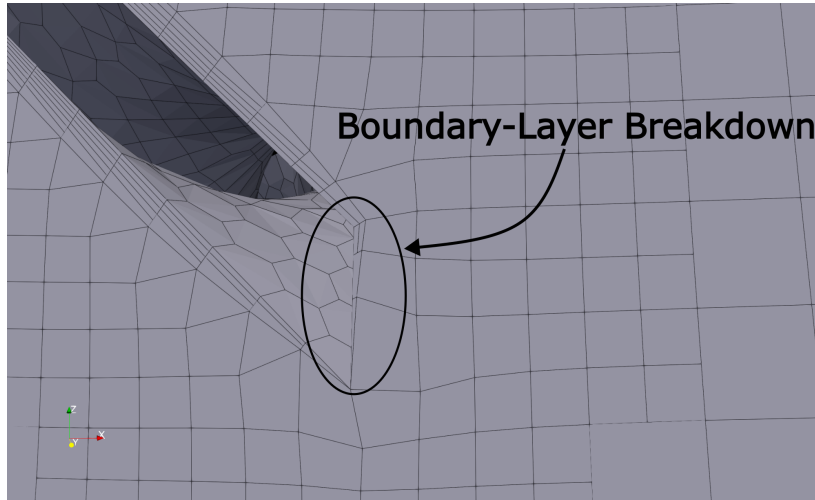
**Figure 4.1:** Meshed computational domain shown as the Gyroid structure embedded in the rectangular meshing domain, a slice through the bulk mesh, and a detail of said slice

The figure shows the gyroid structure embedded in the rectangular meshing domain, a slice through the bulk mesh, and a detail of said slice. The slice shows that different refinement-zones are applied, with decreasing cell size towards the TPMS structure. Immediately adjacent to the geometry, twelve prism layers are extruded with a growth ratio of 1.1 and a positioning of the first layer, such that  $y^+ < 1$ . The internal hexahedral cells are aligned with the primary flow direction (x-direction), and near-wall cells conform precisely to the TPMS surface. Furthermore, the mesh is kept at high quality by enforcing the constraints summarized in Table 4.1.

**Table 4.1:** Mesh quality settings for checkMesh

Setting	Value
max Non-Orthogonality	65
max Boundary Skewness	7
max Internal Skewness	4
max Concaveness	80
min Volume	$1 \times 10^{-13}$
min TetQuality	$1 \times 10^{-15}$
min Twist	0.02
min Determinant	0.001
min FaceWeight	0.05
min Volume-Ratio	0.01
max Aspect Ratio	50
max Growth Ratio	2

As outlined before, enforcing these mesh quality constraints is crucial for solver stability and accurate results. However, this strict adherence occasionally prevents the extrusion of the full set of boundary-layer cells in some regions, as the layer-generation algorithm can not satisfy all quality thresholds while maintaining the specified layer thicknesses. One of those regions where the boundary layer breaks down is shown in Figure 4.2.

**Figure 4.2:** Boundary layer breakdown in regions, where mesh quality and low cell size could not be combined

Although the location and extent of these regions vary slightly between cases, no less than 97 % of the boundary layer is fully extruded throughout the different setups. Furthermore, to still maintain accuracy in the breakdown regions, the first wall-adjacent cell in these zones is refined to satisfy  $y^+ < 5$ , thereby allowing to model these regions with the low-Reynolds-number wall functions (see Section 3.3).

Special care is also taken to ensure that the meshes on corresponding AMI patches (left  $\leftrightarrow$  right, top  $\leftrightarrow$  bottom) are closely matched. Poor alignment can yield very small or zero interpolation weights, which skew gradient calculations, underpredict fluxes, and ultimately can lead to a violation of continuity across the interface.

## Chapter 5

# Verification and Validation

Using a simulative approach to investigate real-world phenomena provides a powerful, cost-efficient, and flexible method to test novel engineering applications. However, to ensure that the attained results are physically accurate, the assumptions and numerical behaviour need to be verified, and the final simulation results must be validated against experimental data. Numerically, different aspects need to be taken into account, such as the convergence and grid independence of the simulation results. Once grid-independence and convergence is proven, the assumptions of incompressibility assumption is verified, before the final simulation results are validated against experimental data from literature. Because the overall flow structure is very similar for all cases, verification and validation are performed only for the 10G configuration. It is assumed that the results extend to the other configurations as well.

It should be noted that the experimental study used for validation defines the hydraulic diameter as the side length of the channel. To ensure consistency and avoid confusion from switching between definitions, this convention is maintained throughout this chapter. This choice does not affect the verification procedure, as it is applied exclusively to the 10G structure, where any change in hydraulic diameter would merely result in a rescaling of the Nusselt number and friction factor.

### 5.1 Convergence

The SIMPLE solver iteratively solves the incompressible Navier–Stokes equations toward a steady-state solution. This solution is assumed to be converged when successive iterations no longer produce meaningful changes between iteration steps. Gauging convergence is essential because it confirms that the computed flow field satisfies the governing equations to the desired precision, ensuring physical reliability of the results.

Therefore, convergence is assessed using three different metrics. First, the evolution of pressure and velocity at three representative probe locations is kept track of and inspected to confirm that these variables no longer change significantly between successive iterations. Second, global thermophysical quantities, namely the Nusselt number and the overall pressure drop, are tracked in the same manner and are considered converged once their incremental variation falls below a predefined tolerance. The third metric considers the solver residuals, which quantify the remaining imbalance in the linear system. In OpenFOAM, the residuals are calculated as [42]

$$r = \frac{1}{n} \sum_{i=1}^n |b_i - (A\mathbf{x})_i|.$$

where  $n$  is the total number of discretized equations (typically one per control volume),  $b_i$  is the right-hand-side contribution for equation  $i$ ,  $A$  is the coefficient matrix assembled

from the discretized governing equations,  $\mathbf{x}$  is the current solution vector, and  $(A\mathbf{x})_i$  is the reconstructed left-hand side for equation  $i$ . The absolute difference  $|b_i - (A\mathbf{x})_i|$  therefore measures the imbalance of each equation, and  $r$  represents the average of these imbalances over the entire domain.

Two different residuals are monitored. The initial residual, which quantifies the imbalance remaining from the previous solution before the new set of SIMPLE corrector iterations starts, and the final residual, which indicates how effectively those iterations have reduced that imbalance. This essentially keeps track of how well the overall simulation is converging (initial residual) and how well the SIMPLE solver converges within the current set of corrector iterations for that same step (final residual).

In general, both of these should drop over the course of the simulation, since the solver is getting closer to the steady state solution. In highly turbulent flows, however, this decrease can level off and the residuals can stall, because the solver is forcing a steady-state formulation onto a flow that is inherently unsteady [10]. This could be circumvented by solving for the fully transient flow. However, since the unsteady flow features are not of interest for this study, a case is deemed converged when the integral quantities of interest have stabilized and the monitored field variables show only minor fluctuations, even if the residuals have plateaued. Exemplary, the convergence of the 10G case is shown below:

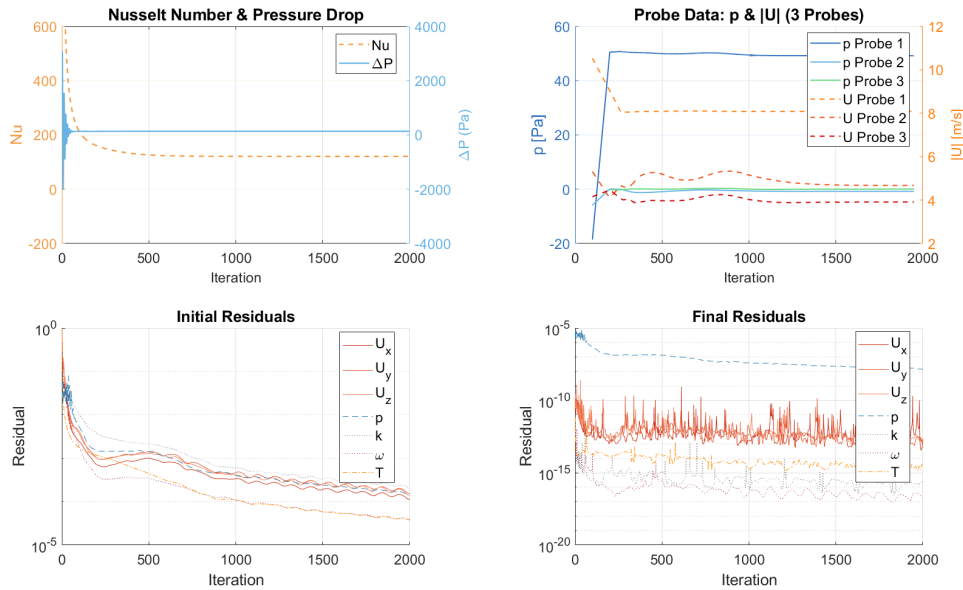


**Figure 5.1:** Exemplary convergence of the 10G case, including the initial and final residuals, the integrated quantities, and probe values

It can be seen that both the Nusselt number, the pressure drop, and the probe values level off toward constant values. In addition, the initial and final residuals decline as the simulation proceeds, although they exhibit oscillations due to the flow's unsteady nature. Any simulation, that exhibits a similar behaviour, is assumed to be converged.

## 5.2 Grid Independence

As mentioned previously, a CFD simulation is a numerical approach to approximate the solution of the governing equations for a given flow problem. The accuracy of this approximation heavily depends on the discretization of the problem over the computational Grid [56]. This discretization leads to numerical errors that occur from representing said governing equations as an algebraic expression in a discrete spatial domain.

The discretization errors decrease asymptotically as the spacing between individual grid points ( $\Delta x$ ,  $\Delta y$ ) decreases, and the total number of grid cells increases. As a result, the simulation solution becomes progressively less sensitive to the grid spacing with mesh refinement [55]. However, finer meshes lead to a significant increase in computational cost. A rule of thumb is that the computational cost scales roughly linearly with the total number of cells. For instance, doubling the resolution in both dimensions of a 2D grid ( $N_x \times N_y$ ) results in a fourfold increase in the number of cells, thereby quadrupling the computational cost. Hence, a balance between a low discretization error and a reasonable computational cost needs to be achieved [56].

Since the discretization error reduces asymptotically with smaller grid spacing, a region of grid independence can be defined. In this region, further mesh refinement does not lead to a substantial reduction in discretization error, ensuring that the solution is effectively independent of the grid resolution.

Various methods exist to quantify spatial and temporal convergence, as outlined by Roache [55]. However, the most common approach to evaluate numerical uncertainty is a grid convergence or grid refinement study. When combined with the Grid Convergence Index (GCI), a standardized method proposed by Roache [54] for reporting grid convergence studies, this approach provides an effective tool for assessing grid independence.

The GCI is based on Richardson extrapolation, a numerical technique used to estimate the exact solution of discretized problems by utilizing numerical results obtained at different levels of discretization [55].

### 5.2.1 Grid convergence study

In the grid convergence study, two or more discrete solutions of different grid spacings are generated to calculate a Richardson error estimator  $E$ , which approximates the error of a grid solution  $f$  to that of a coarser or finer grid. It can be differentiated between a fine-grid estimator, where the error of a fine mesh solution,  $f_2$ , is approximated, by comparing it to a solution of a coarse grid  $f_1$ . Or a coarse-grid estimator, where the error of the coarse mesh solution is approximated by comparing it to the fine grid. The estimators are defined as [55]:

$$E_1^{fine} = \frac{\epsilon}{1 - r^p} \quad E_2^{coarse} = \frac{r^p \epsilon}{1 - r^p} \quad (5.1)$$

The estimators depend on the relative error between the solutions  $\epsilon = \frac{f_1 - f_2}{f_1}$ , on the order of convergence  $p$ , and on the refinement ratio  $r$ , which are defined as [55]:

$$r = \frac{h_i}{h_j}, \quad p = \frac{\ln|f_2 - f_3| - \ln|f_1 - f_2|}{\ln r}.$$

where  $h_{i,j}$  denotes the characteristic grid spacing on mesh  $i$  or  $j$ . For structured grids the grid spacing is defined as  $h = \Delta x$ . For unstructured grids, it is usually defined as  $h = (\bar{V})^{1/3}$ , using the cube root of the mean cell volume. The indices 1, 2, and 3 here represent three different mesh refinements: coarse, medium, and fine. Using the estimators and a safety factor of  $F_s = 1.25$ , the GCI for the fine- and coarse-grid solutions are [55]

$$\text{GCI}_{\text{fine}} = F_s |E_1^{\text{fine}}| \quad \text{GCI}_{\text{coarse}} = F_s |E_2^{\text{coarse}}|$$

where the fine-grid GCI measures the discretisation error still present in the finest mesh, while the coarse-grid GCI provides the corresponding error estimate for the next-coarser mesh. These estimates can be seen as a measure of the percentage that the solution is away from the asymptotic numerical value. Hence, it defines an error band that predicts how much the solution would shift if the mesh were refined further [55]. A low GCI therefore, signals that the simulation has already entered the asymptotic regime and additional refinement would produce minor changes.

The grid independence study is conducted for the 10G case using the Nusselt number and pressure drop. Three different meshes with 1.13 million, 1.66 million, and 2.40 million cells are created, resulting in a refinement ratio of  $r \approx 1.2$  between the grids. Since the Nusselt number heavily depends on the spacing of the first grid cell adjacent to the wall, the same refinement factor is applied to the boundary cells. The results of the Grid refinement study are shown below.

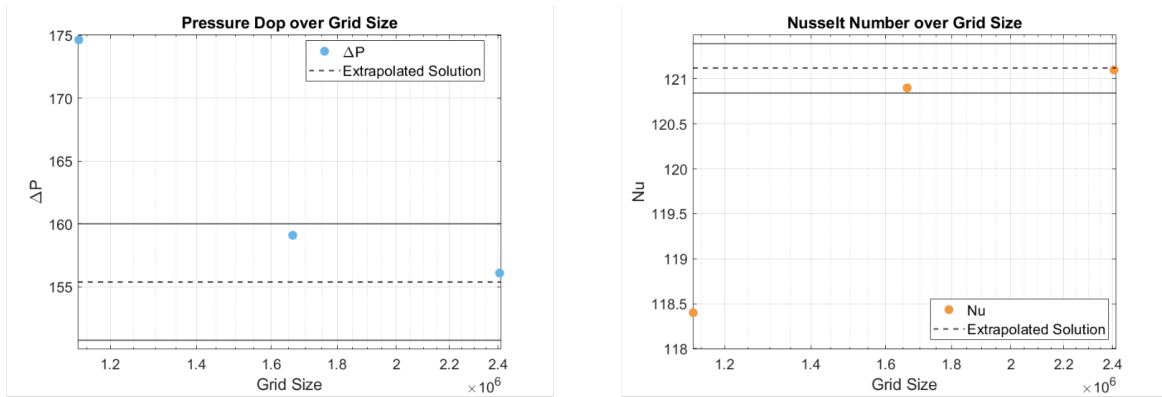


**Figure 5.2:** Values of the Nusselt number and pressure drop for the coarse, medium and fine meshes, plotted over the Gridsize

Figure 5.2 shows the results of the Nusselt Number and pressure drop for the three different grids. The error band describes the absolute uncertainty band around the exact solution, calculated as  $\text{Band} = f_{\text{exact}} \pm \text{GCI}_{f_m} \cdot f_{\text{exact}}$ , which can be treated as a 95%-style confidence interval for the discretization error [55]. Therefore, based on the observed grid-convergence behaviour and the conservative safety factor, the true drag coefficient is expected to fall somewhere between error-band if the mesh were refined towards the continuum limit.

It can be seen that, as the mesh is refined, both the Nusselt number and the pressure drop converge towards the Richardson-extrapolated value. Furthermore, the values for the medium and fine mesh lie inside the 95 % confidence interval for both integrated measures, indicating that the medium mesh lies inside the asymptotic range of convergence. This is supported by  $AR = \frac{GCI_{fine}}{GCI_{coarse} r^p} = 0.9984$ , which is very close to the ideal value of unity, confirming that the solutions have reached the asymptotic regime according to the criterion suggested by Roache et al. [55]. To fully gauge if the simulation is grid independent, the GCI values, which for the coarse and the medium mesh are shown in Figure 5.3, are also taken into account.

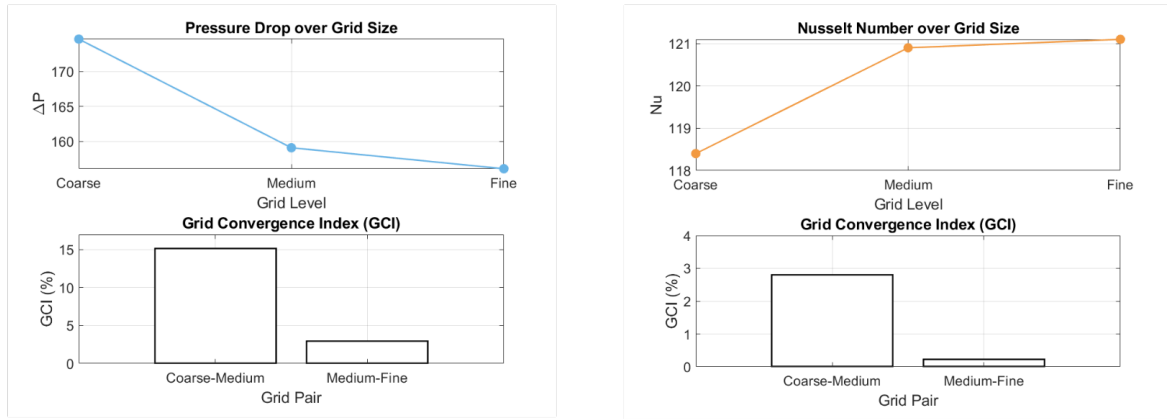


**Figure 5.3:** Grid convergence indices based on the coarser mesh, for both the coarse and medium mesh

The calculated GCI values for the pressure drop and Nusselt number, based on the previously described coarse estimator, are 15.05 % and 3.01 % for the coarse mesh, and 2.92 % and 0.211 % for the medium mesh, respectively. For the medium mesh, these values fall comfortably below the 5 % threshold suggested by Roache [55]. The low GCI values, together with the demonstrated asymptotic behavior, indicate that the medium mesh is sufficiently fine to accurately resolve the flow. It is therefore chosen over the fine mesh due to its significantly lower computational cost while maintaining comparable accuracy. Conversely, the coarse mesh is not selected, as it exhibits high discretization errors and fails to provide sufficient accuracy.

It should be noted that some of the smaller unit-cell configurations require finer grid spacing to fully resolve their detailed features. Nevertheless, the grid spacing used throughout all investigated cases never exceeds that of the medium mesh established in the grid-independence study.

### 5.3 Incompressibility Assumption

The flow in this study is assumed to be incompressible, because inclusion of compressibility effects would significantly increase the computational cost. However, strictly speaking, heated air cannot be treated as fully incompressible, since high temperature gradients and elevated velocities can cause noticeable changes in density. Quantitatively, an increase in temperature from 298 K (inlet) to 353 K (TPMS region) results in a density decrease of

approximately 15 % (from  $1.18 \text{ kg/m}^3$  to  $1.00 \text{ kg/m}^3$ ), potentially introducing inaccuracies due to fluid compressibility effects. One such compressibility-driven effect is buoyancy, which can be evaluated through the Richardson number ( $Ri$ ). For this specific setup, the Richardson number is calculated as  $Ri \approx 4 \times 10^{-4} \ll 1$ , indicating that buoyancy forces are small compared to inertial forces and thus do not significantly influence the flow field.

The Mach number in this study remains well below the compressibility threshold of 0.3, indicating, that velocity-induced compressibility is negligible.

Regarding the pressure drop, rearranging the friction factor equation (Eq. 2.11) yields:

$$\Delta p = f \frac{L}{D} \frac{\rho U^2}{2},$$

This demonstrates a direct dependence of the pressure drop on fluid density. Thus, a density variation of up to 15 % could theoretically introduce a corresponding discrepancy in the computed pressure drop. However, since the pressure drop is averaged across the entire channel cross-section and not all fluid regions experience temperatures as high as 353 K, the actual error is anticipated to be substantially lower and within an acceptable range.

To conclusively verify this an additional simulation employing the compressible solver rhoSimpleFoam is conducted and compared directly to the incompressible results. These results are shown below:

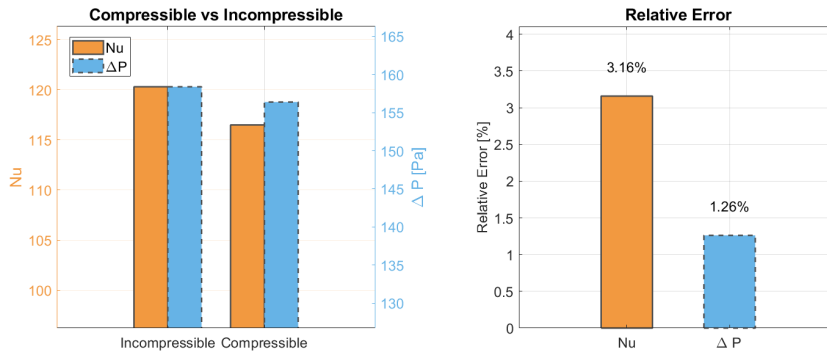


**Figure 5.4:** Comparison of the Nusselt number and pressure drop for the incompressible and compressible 10G case

The Nusselt number and pressure drop for the incompressible and compressible cases are 120.9 and 116.5, and 158.4 Pa and 156.3 Pa, respectively. The compressible case exhibits slightly lower values for both quantities. This behavior can be attributed to thermal expansion. The resulting decrease in density increases the kinematic viscosity, enhancing momentum diffusion and leading to a flatter velocity profile. Consequently, the velocity gradient at the wall decreases, reducing the wall shear stress  $\tau_w$  and thereby the pressure drop. Furthermore, thermal expansion increases the thermal boundary layer thickness, which lowers the temperature gradient at the wall and results in a reduced Nusselt number.

Figure 5.4, also shows that the observed differences in Nusselt number and pressure drop between the incompressible and compressible cases are relatively small. As shown in Figure 5.4, the relative error is 3.16 % for the Nusselt number and 1.26 % for the pressure drop. These discrepancies are minor, and in the case of the pressure drop, the difference is even smaller than the estimated discretization error ( $GCI_{\text{coarse}} = 3.01\%$ ). This suggests that, under the given conditions, the effects of thermal and inertial compressibility are limited, and the compressibility assumption can be used to obtain accurate results at a lower computational cost.

## 5.4 Experimental Validation

To complete the verification and validation process and build confidence in the physical accuracy of the simulation results, they are compared with experimental and computational data from the literature. As discussed in Section 1.2, only a few studies have experimentally investigated heat transfer in TPMS structures. Moreover, most of these studies used different setups and boundary conditions, making direct comparison with the present work difficult. However, one study by Khalil et al. [29] experimentally investigated flow through a Gyroid sheet structure with a porosity of 20 % and a unit cell size of 10 mm. Based on this, the 10G case from the present study is selected for validation, using the results from Khalil et al. [29] as a reference.

The study by Khalil et al. [29] was conducted over a broad range of Reynolds numbers, including  $Re = 5000$ , although a key difference is that their experiment employed physical walls as channel boundaries. In their work, the pressure drop was measured and used to calculate the friction factor, which served as the basis for validating a CFD simulation. This validated simulation was then used to investigate the heat transfer characteristics in more detail. As a result, experimental validation in the present study can only be performed using pressure drop and related flow parameters. To further increase confidence in the physical accuracy of the simulation, the Nusselt number and heat transfer coefficient will be compared against the computational results provided by Khalil et al. [29]

### Pressure Drop and Friction Factor

In their study, Khalil et al. [29] calculated the friction factor based on the mean density and mean velocity of the fluid within the TPMS structure. Additionally, they use the channel height as the hydraulic diameter. To ensure a consistent and easier comparison, the friction factor in this section is computed using the same approach. The values for the pressure drop per unit length and the friction factor are shown in Figure 5.5

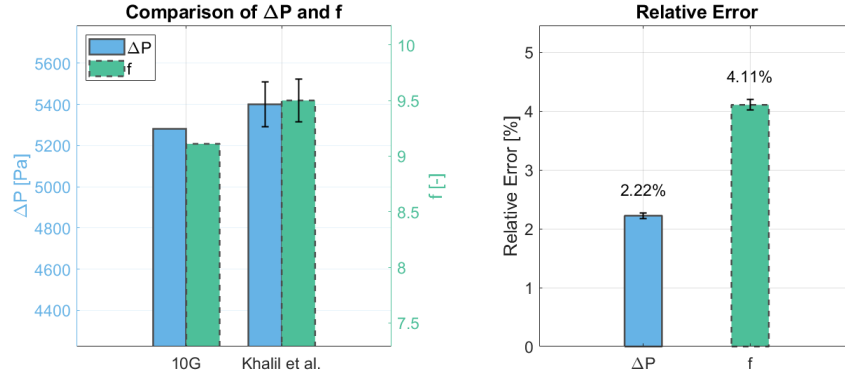


**Figure 5.5:** Comparison of the simulated pressure drop per unit length and friction factor with the experimental results reported by Khalil et al. [29]. The error bars indicate uncertainties due to the approximate extraction of the values from the published data.

At  $Re = 5000$ , the study by Khalil et al. [29] does not report explicit numerical values for the pressure drop and friction factor, but presents them graphically. As a result, the values could only be approximated by extracting data from the plots, introducing some uncertainty. To account for this, a reading uncertainty of 2 % is assumed. This is represented by the error bars in Figure 5.5.

The experimentally determined pressure drop, normalized by the length of the TPMS structure, is slightly higher at  $\Delta P/L = 5400 \pm 100$  Pa/m compared to the simulated value of  $\Delta P/L = 5280$  Pa/m. This discrepancy can be attributed to the absence of channel walls in the present simulation, where periodic boundary conditions reduce wall-induced shear stress, leading to a lower overall pressure drop. However, since the total pressure drop is primarily governed by the interaction of the flow with the TPMS geometry, the deviation remains small, within a range of 2.18 % to 2.26 %.

As the friction factor directly depends on the pressure drop per unit length (see Equation 2.11), a similar trend is observed here. The deviation in friction factor, however, is slightly larger than that of the pressure drop per unit length, ranging from 4.02 % to 4.2 %. This can again be attributed to the use of periodic boundary conditions, which do not have lateral flow confinement and thereby result in a higher mean velocity magnitude through the structure, which decreases the friction factor.

The inverse behaviour can be seen for the heat transfer coefficient and the Nusselt number, which are shown in Figure 5.6

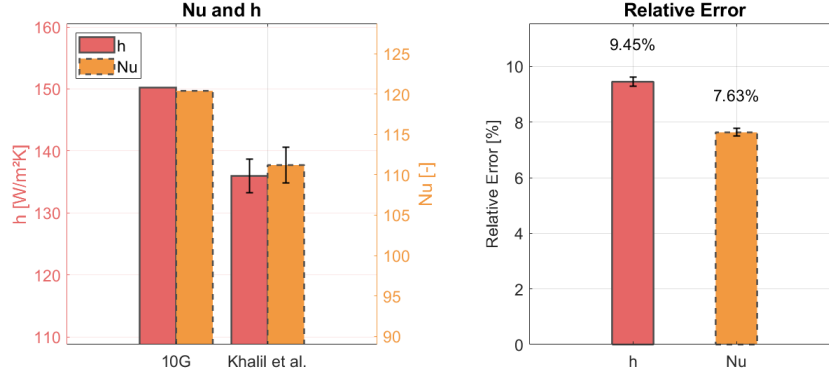


**Figure 5.6:** Comparison of the simulated heat transfer coefficient and Nusselt number with the computational results reported by Khalil et al. [29]. The error bars indicate uncertainties due to the approximate extraction of the values from the published data.

The Nusselt number and heat transfer coefficient for the 10G case are  $Nu = 120$  and  $h = 150 \text{ W/m}^2\text{K}$ , respectively. These values are slightly higher than those reported by Khalil et al. [29], who found  $Nu = 111 \pm 2.2$  and  $h = 136 \pm 2.7 \text{ W/m}^2\text{K}$ . This difference is expected, as the absence of confining lateral walls in the periodic simulation allows for increased flow circulation, which enhances convective transport and thus improves heat transfer performance. Nevertheless, similar to the pressure drop and friction factor, the deviations in the Nusselt number and heat transfer coefficient remain relatively small, with relative errors generally below 10%.

This, together with the low relative errors observed in pressure drop and friction factor, indicates that the simulation results closely align with experimental and computational data from the literature, suggesting that the computational setup employed in this study is physically sound and reliable.

## Chapter 6

# Results and Discussion

With the verification and validation providing a high level of confidence in the physical accuracy of the modeling approach, the simulation study is conducted to investigate the influence of unit cell size on the system's thermal and hydraulic performance. This chapter presents the results of that study, highlighting how changes in unit cell size affect key thermal and hydraulic performance indicators of the system.

For integral parameters such as the Nusselt number and friction factor, this chapter adopts the definition of hydraulic diameter introduced in Section 2.2, as it is considered to be more representative of the characteristic length of the individual TPMS structures than the channel height employed in the previous chapter.

### 6.1 Geometry

Changing the unit-cell length while holding the porosity constant alters key geometric parameters of the structures, such as the total interfacial area  $A_{\text{TPMS}}$  and the hydraulic diameter  $D_h$ . Because the domain volume increases, a direct comparison of the absolute surface area would be misleading, since a larger unit cell size would appear to have a higher surface area simply by occupying more space. A more rigorous descriptor is the specific surface area, defined as the interfacial area normalized by the corresponding fluid volume, i.e. the amount of solid-fluid interface available per unit volume of fluid:

$$A_s = \frac{A_{\text{TPMS}}}{V_{\text{fluid}}} \left[ \frac{\text{mm}^2_{\text{solid}}}{\text{mm}^3_{\text{fluid}}} \right].$$

This normalization removes the scaling effect and allows cases with differing volume to be compared on an equivalent geometric basis. This specific area is shown in Figure 6.1

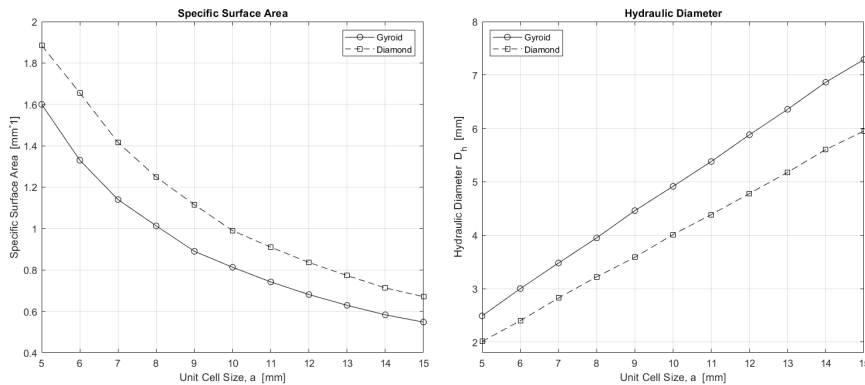


**Figure 6.1:** The left figure shows specific Area, which is calculated as the Area of the TPMS divided by the Volume of the fluid, plotted over the unit cell size. The right finger presents the hydraulic diameter over unit cell size

As anticipated, the calculated specific surface area decreases non-linear as the unit cell size is reduced, which aligns with the findings from Samson et al. [57]. Furthermore, a systematic difference between the two topologies is also apparent, where for every cell size examined, the diamond lattice exhibits a 15 % larger specific surface area than its Gyroid counterpart.

Figure 6.1 also shows the hydraulic diameter, for all investigated unit cell sizes. In contrast to the specific surface area, the hydraulic diameter increases linearly with increasing unit cell size. For the Gyroid and Diamond topologies, this increase from the 5 mm unit cell to the 15 mm unit cell, is 190 % and 196 %, respectively. A direct consequence of the higher specific surface area of the Diamond topologies is their lower hydraulic diameter, which for all unit cell sizes is about 19 % below that of the Gyroid structures.

## 6.2 Flow Path and Structure

To gain a deeper understanding of the mechanisms influencing thermal and hydraulic performance, the general flow structures within the TPMS geometries are examined first. Both the Gyroid and Diamond structures exhibit complex, three-dimensional flow patterns across all investigated unit cell sizes. To highlight the characteristic flow behavior in the two different TPMS topologies, the streamlines for the 15G, 15D, 10G, 10D, 5G, and 5D configurations are shown in Figures 6.2.

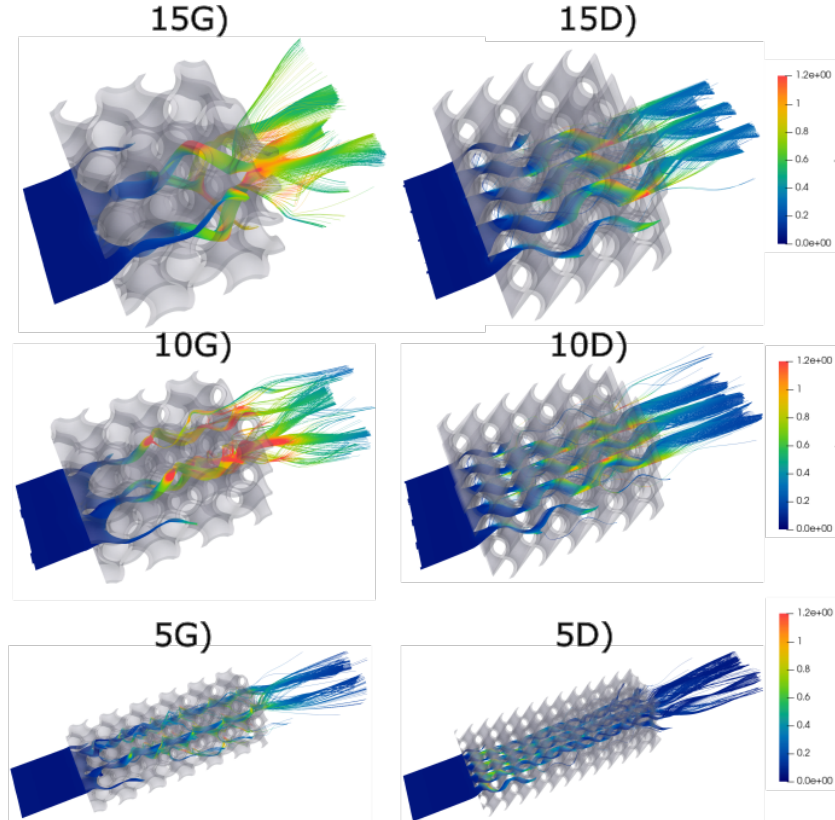


**Figure 6.2:** Streamlines through the Gyroid and Diamond Structure, which are colored using the turbulent kinetic energy

The streamlines in Figure 6.2 are colored by the turbulent kinetic energy ( $k$ ) and extend from the inlet to the outlet of the domain. Since the simulation is conducted under steady-state conditions, the streamlines represent the paths that fluid elements would follow in this steady regime. It can be observed that, as the fluid penetrates the porous domains the streamlines diverge in both topologies.

In the Gyroid lattices (Figure 6.2, left column), fluid dispersion is more chaotic than in the Diamond lattices, which leads to a steeper rise in turbulent kinetic energy  $k$  for the Gyroid structures at equivalent unit cell sizes. Similar observations are described in previous studies by Yreanee et al. [75]. Furthermore, as the unit cell size increases, the Gyroid flow becomes progressively more disordered, whereas the Diamond lattices exhibit only a modest increase in flow dispersion with increasing unit cell size. In both topologies,  $k$  decreases as the unit cell size is reduced, which is also consistent with previous findings by Samson et al. [57].

This can mainly be attributed to the decrease in hydraulic diameter, which increases the fraction of fluid subjected to near-wall effects and thereby increases the fraction of the viscous sub-layer, in which the turbulent kinetic energy is suppressed. Because the volume-averaged velocity is approximately constant across all cases ( $\langle u \rangle_{pore} = u_{in}/\phi$ , see Section 2), a smaller  $D_h$  lowers the average local Reynolds number  $Re_h = \langle u \rangle_V D_h / \nu$ , which reduces the production of turbulence and thereby leads to a lower turbulent kinetic energy.

Furthermore, for all cases the turbulent kinetic energy is found to increase as the flow propagates further through the TPMS, with the exception being the 5D setup. Here, a reduction in  $k$  in flow direction can be observed. This is shown in more detail in Figure 6.3, which presents samples of the turbulent kinetic energy throughout the 5G and 5G structure.

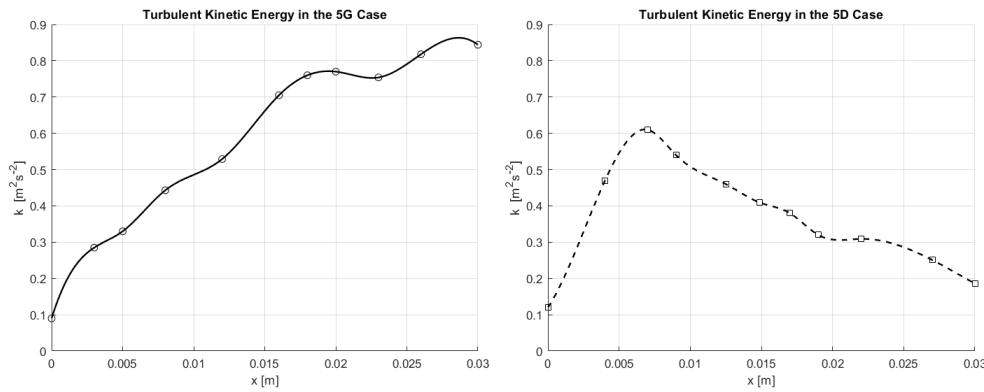


**Figure 6.3:** Different samples in x-direction of the turbulent kinetic energy throughout the 5G (left) and 5D (right) cases

After an initial increase in turbulent kinetic energy due to flow disruption, a downstream decline in  $k$  is observed in the 5D lattice, indicating a progressive weakening of turbulence along the flow path. This turbulence damping, which is only present for the 5G case, arises from the small hydraulic diameter, which gives an average local Reynolds number of  $Re_{h,5D} = 564$  and thereby suppresses turbulence production. In the 5G lattice, the average local Reynolds number is only slightly higher, at  $Re_{h,5G} = 713$ . However, the combination

of a higher  $Re_h$  and a more chaotic and convoluted flow path of the Gyroid geometry enhances turbulence generation and offsets the tendency toward turbulence damping. This effect of turbulence damping in small channels is well documented in literature for micro channels and converging nozzles [18, 36]

As described, Figure 6.2 highlights the more chaotic flow patterns within the Gyroid structure but also indicates that the geometric variations induce different internal fluid behavior. This contrast in internal flow between the Diamond and Gyroid configurations is further illustrated in Figure 6.4 and 6.5, which presents velocity contours and vector fields on the central x-z and y-z plane for the 15G, 15D, 10G, 10D, 5G, and 5D cases.

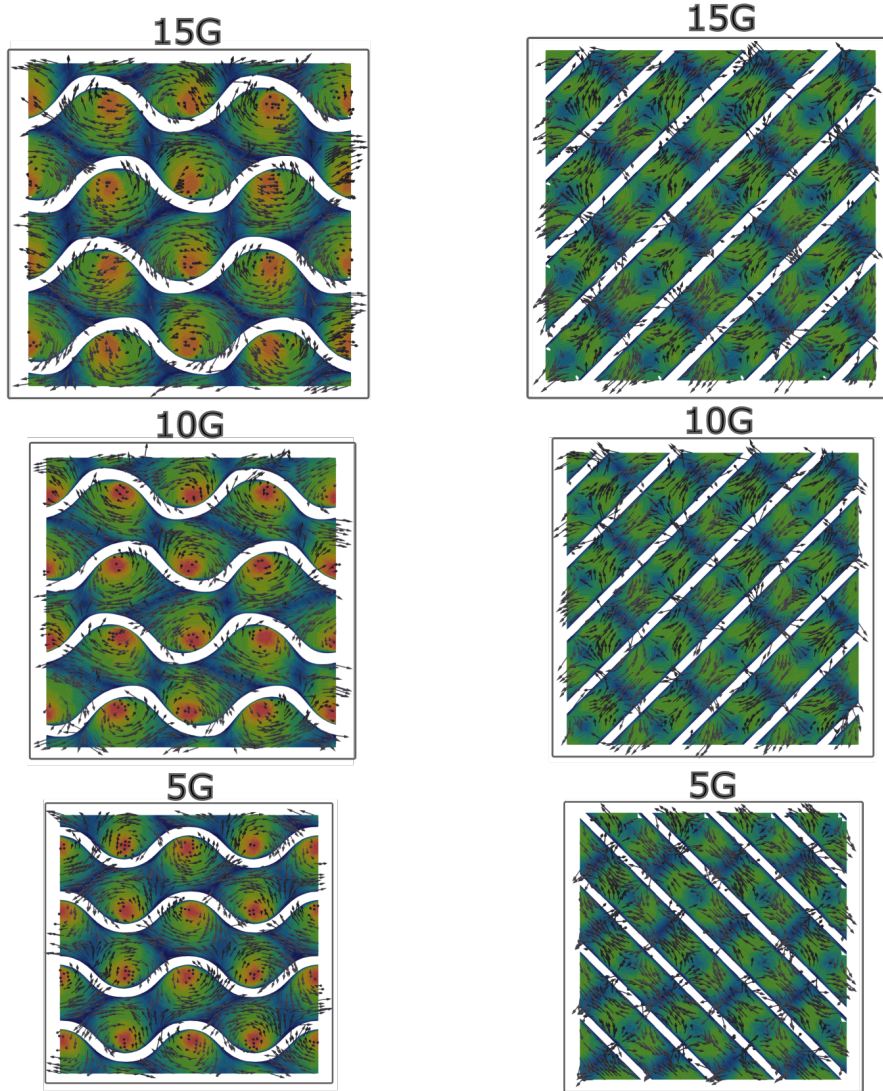


**Figure 6.4:** Slices of the flow field through the lateral center plane of the 15G, 15D, 10G, 10D, 5G, and 5D structures. These are colored using the velocity.

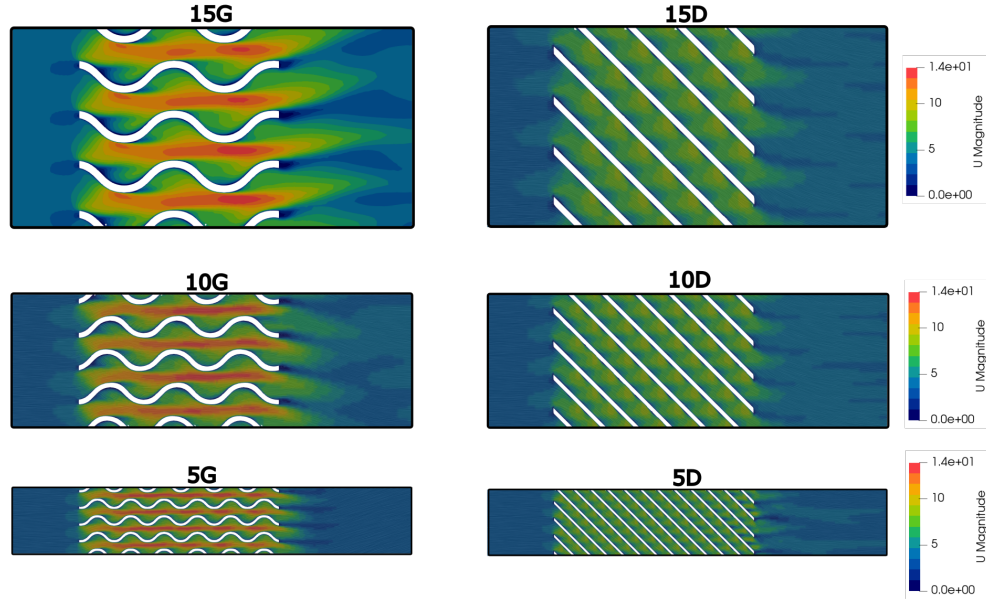


**Figure 6.5:** Slices of the flow field through the horizontal center plane of the 15G, 15D, 10G, 10D, 5G, and 5D structures. These are colored using the velocity. The arrows follow the velocity vectors

In Figure 6.4, it can be observed that the sheet-like TPMS surfaces bisect the flow into two distinct domains. In the Gyroid structures (Figure 6.4 left), one domain develops a clockwise helical motion while the other spins counter-clockwise, both swirling around the through-holes, where speeds peak at about 14 m/s. Figure 6.5 shows, that these through-holes are aligned with the flow direction and therefore allow for a high velocity region to form with the Gyroid structures.

In contrast, the Diamond structures (Figure 6.4, right) exhibit alternating clockwise and counterclockwise vortices within each partitioned domain. While localized regions of acceleration and recirculation are present, the overall flow is more uniform, with lower peak velocities reaching up to 9.3 m/s. This behavior is further supported by the horizontal slices shown in Figure 6.4, which indicate slightly elevated velocities near the upper channel walls. This occurs because the diagonal arrangement of the Diamond geometry diverts the flow at these surfaces, deflecting it from the primary flow direction, which leads to local acceleration. However, this effect is less pronounced than in the Gyroid case, as the Diamond topology lacks a single, continuous pathway aligned with the main flow direction. This difference in flow organization also contributes to the lower levels of turbulent kinetic energy observed in the Diamond structures, since the more structured flow and smoother velocity gradients reduce turbulence generation and promote a more stable and uniform flow profile.

As the fluid passes through the TPMS structures, it interacts with the surfaces of the lattice, generating shear stress along the walls. The resulting local wall shear stresses are shown in Figure 6.6 for the 15G, 15D, 10G, 10D, 5G, and 5D cases.

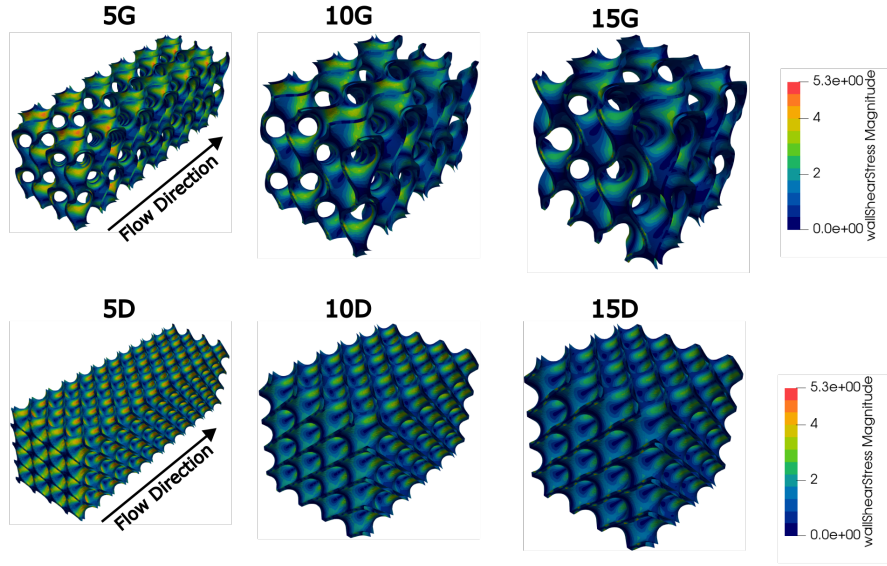


**Figure 6.6:** Distribution of the wall shear stress on the surface of the TPMS structures

The wall shear stress is directly proportional to the velocity gradient normal to the surface, as described by  $\tau_w = \mu \left( \frac{\partial u}{\partial n} \right) \big|_{\text{wall}}$ . This relationship explains the generally higher wall shear stress observed in cases with smaller unit cell sizes. As these configurations maintain a similar average pore velocity while confining the flow to narrower channels, the resulting velocity gradients near the wall become steeper, thereby increasing the shear stress. This trend has also been reported by Samson et al. [57] and Li et al. [30] for Gyroid structures.

A comparison of the two topologies reveals that both the Gyroid and Diamond structures exhibit localized regions of elevated wall shear stress. In the Gyroid structures, these regions are found where the flow paths narrow and the high-velocity core passes close to the structure surface, as shown in Figure 6.5. This proximity increases the local velocity gradient, which increases wall shear stress. For Gyroid topologies these regions were also linked to flow recirculation by Samson et al. [57]. They further show that these wall shear stress peaks are higher compared to the mean wall shear stress for bigger unit cell sizes, indicating stronger recirculation. Recirculation regions are also observed in this study behind most Gyroid topologies, as shown in Figure 6.7.

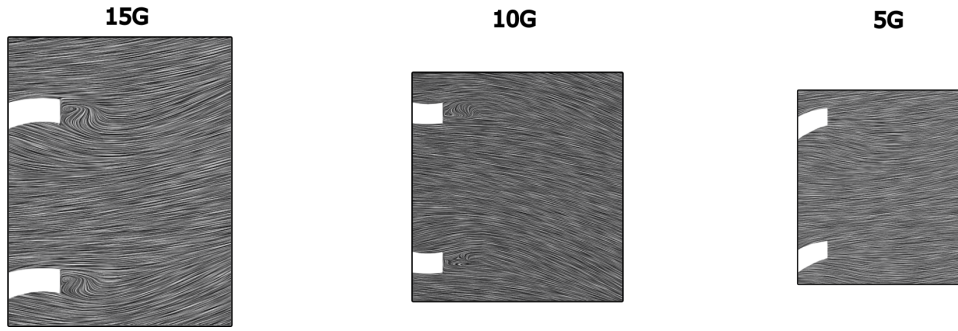


**Figure 6.7:** Detail of regions behind the 15G, 10G and 5G structures, showing recirculation zones

It can be seen that recirculation zones form downstream of the trailing edges of the solid struts. In the 15G case these zones are most pronounced. For the 10G case they remain visible but are weaker, and in the 5G case, they are completely absent, indicating that, as the size of the unit cell decreases, flow recirculation progressively weakens until it eventually vanishes.

This observation aligns with the earlier finding that, in the Gyroid topology, larger unit-cell sizes promote increasingly chaotic flow, since enhanced flow separation and the resulting recirculating wakes destabilize the shear layers, driving the transition to a more chaotic and turbulent regime [58].

In the Diamond topologies, no such recirculation regions behind the structures are present, thereby allowing for the more stable flow pattern.

Further analysis of Figure 6.6 shows, that for the Diamond topologies, regions of high wall shear stress are less extreme than in the Gyroid cases, but more frequent and typically appear as two distinct zones on opposite sides of the internal surfaces. These occur where the geometry forces the fluid to redirect around the central wall features, resulting in elevated shear stress along both paths. This flow splitting plays a key role in generating the counter-rotating vortices observed in Figure 6.4.

These rotational motions, induced by both the Gyroid and Diamond topologies, give rise to coherent vortex structures that extend downstream of the TPMS. Figure 6.8 visualizes these vortices using the Q-criterion on slices taken 10 mm downstream of the cellular structures.

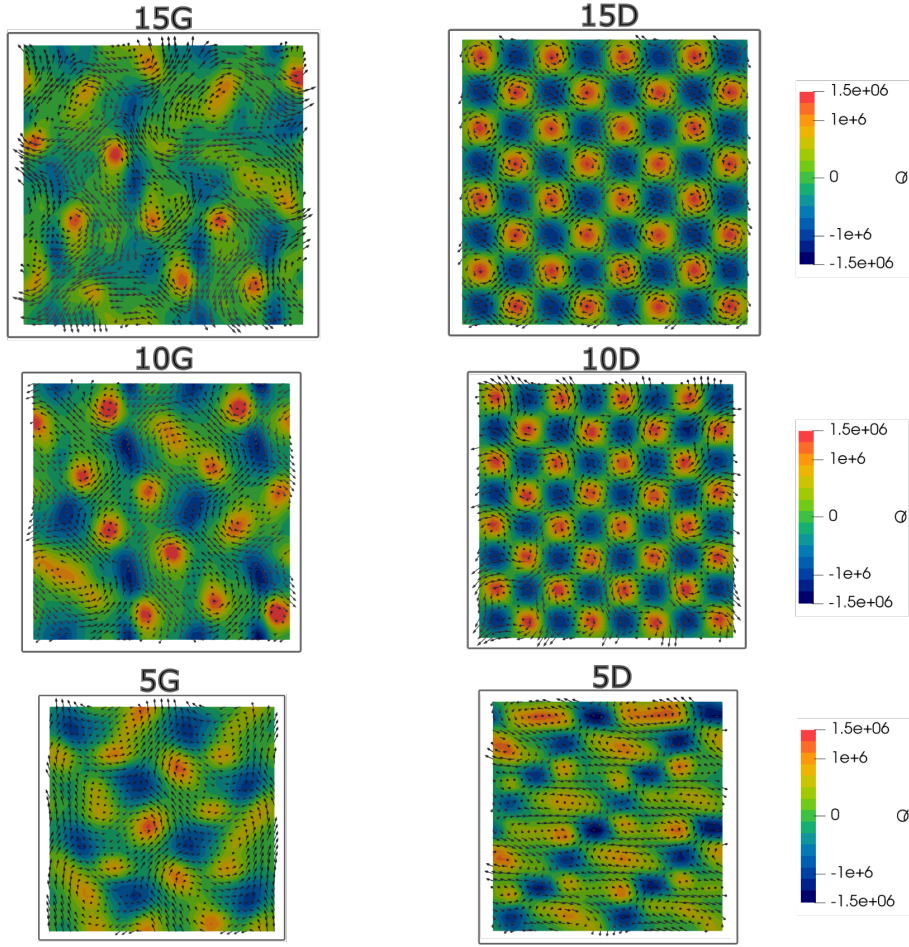


**Figure 6.8:** Slices of the flow field 10 mm behind the 15G, 15D, 10G, 10D, 5G, and 5D. These are colored by the Q-criterion

These slices are colored using the Q-criterion and show the velocity vector-field in the form of arrows. Generally, vorticity can be used to measure local fluid rotation. It alone, however, does not reliably distinguish between pure shear and true vortical motion. To address this, the Q-criterion is employed, to more accurately identify coherent vortex structures within the flow [25]. The Q-criterion is defined as  $Q = \frac{1}{2} (\|\mathbf{\Omega}\|^2 - \|\mathbf{S}\|^2)$ , where  $\mathbf{\Omega}$  and  $\mathbf{S}$  are the antisymmetric and symmetric parts of the velocity gradient tensor, representing rotation and strain, respectively. This criterion evaluates the local balance between rotation and strain. Regions where  $Q > 0$  indicate that rotation dominates over strain, indicating the presence of vortex structures, with the vortex cores being in the regions of the highest  $Q$ .

As shown in Figure 6.8, the Gyroid structures (left) generally display a more irregular vortex distribution, whereas the vortices in the Diamond geometries (right) form a checkerboard-like pattern. This contrast reflects the inherently more chaotic flow in the Gyroid topology described above. Significant variations also emerge across unit cell sizes within each topology. In the Gyroid structures, the 15G configuration exhibits lower peak values of  $Q$  in its vortex cores and a more smeared  $Q$ -distribution than the 10G case, due

to increased momentum mixing from its more disordered flow. The 5G model likewise shows reduced maximum  $Q$  and increased dispersion. However, here the difference is driven by the lower turbulent kinetic energy in the 5G case, which accelerates vortex decay. Consequently, by 10 mm downstream of the TPMS, momentum diffusion has markedly smoothed velocity gradients and weakened coherent vortex structures.

This trend is even more pronounced in the 5D case, which features the lowest turbulent kinetic energy at the outlet of all samples. At higher unit cell sizes however, the increased dispersion of  $Q$  seen in the 15G does not occur in the Diamond lattice, which exhibits nearly identical structures between the 10D and 15D case. This is a result of the comparatively orderly nature of the flow through the Diamond lattices, even at high unit cell sizes, which never transitions into the highly dispersed, chaotic regime observed in the 15G configuration.

### 6.3 Thermal distrubtion

As the fluid progresses through the TPMS structure, it steadily warms along the flow direction. This progressive heating is directly influenced by the pore geometry and the resulting flow structure, which governs both the local temperature distribution and the overall thermal performance of the TPMS structure. To illustrate this relationship, the temperature distribution within the 15G, 15D, 10G, 10D, 5G, and 5D cases are presented in Figure 6.9.

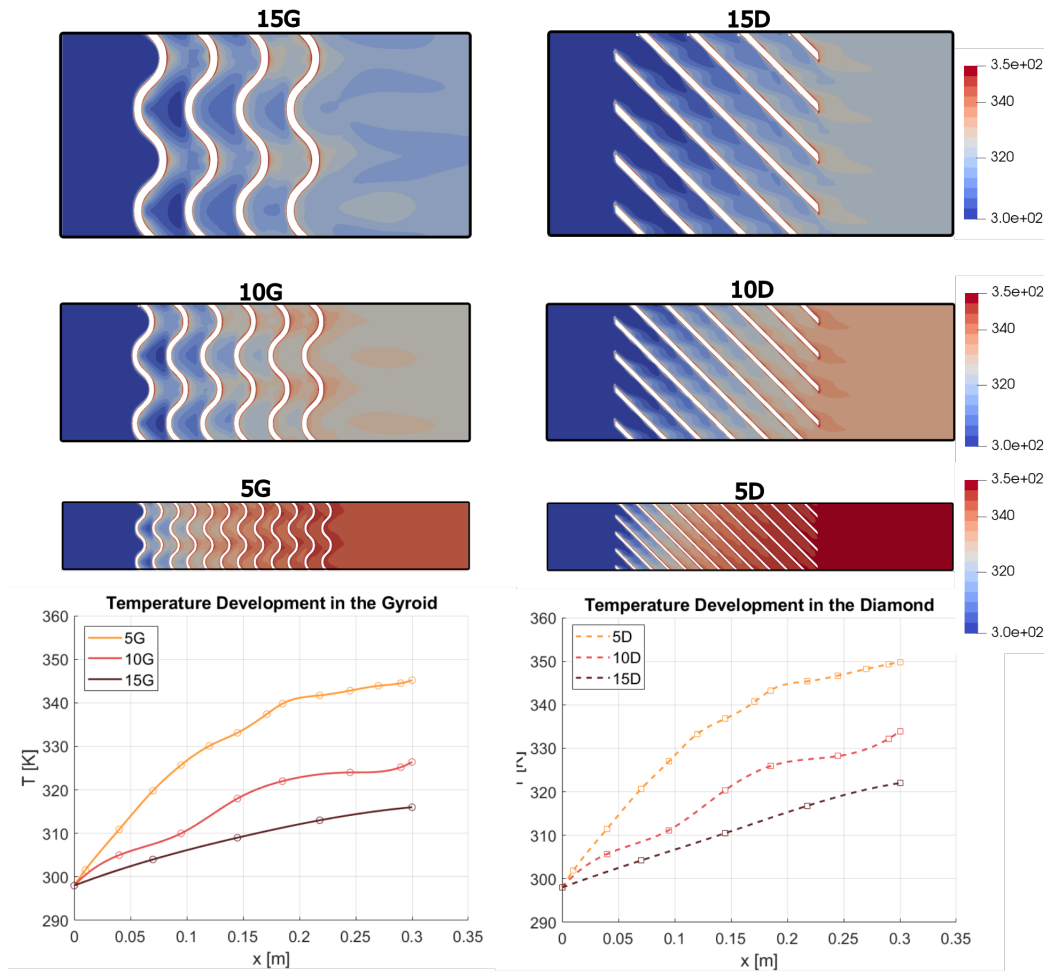


**Figure 6.9:** Slices of the temperature field through the horizontal center plane of the 15G, 15D, 10G, 10D, 5G, and 5D structures are shown, with color indicating local temperature. The graphs below plot the temperature readings recorded by probes placed in each corresponding structure.

The slices shown in Figure 6.9 illustrate the temperature distribution within the central  $x$ - $z$  plane for the different TPMS structures. The accompanying plots show the temperature profiles for the depicted Gyroid and Diamond structures, derived from samples taken at multiple bulk-flow locations (away from the walls) along a straight line, which is positioned centrally within the flow domain.

It can be seen that the fluid temperature increases steadily as it passes through the structures. This temperature rise is more pronounced for smaller unit cell sizes, which have a

higher specific surface area. As a result, these structures offer a greater solid-fluid interface per volume of fluid, thereby enhancing heat transfer and accelerating the temperature increase. For example, in the Gyroid structures, the 5G case reaches the outlet temperature of the 10G structure (326 K) after just 0.009 m, corresponding to approximately 30 % of the total length. The outlet temperature of the 15G structure (317 K) is reached even earlier, at 0.006 m (20 %).

A similar trend is observed in the Diamond structures, although the distances required for the 5D case to reach equivalent 10D and 15D outlet temperatures are slightly longer. This can be attributed to their generally higher specific surface area. In the 5D case, the outlet temperature of the 15D structure (323 K) is reached after 0.008 m (27 %), and the outlet temperature of the 10D structure (334 K) is attained after 0.012 m (40 %).

Comparing the two topologies reveals that, for identical unit cell sizes, the Diamond structures consistently exhibit higher temperatures throughout the domain. This can again be linked to their higher specific surface area relative to the Gyroid topology, enabling more efficient heat transfer through a larger interface.

Internally, the temperature distribution closely reflects the velocity fields shown in Figure ???. Regions of high velocity tend to exhibit lower temperatures, while regions with slower flow display elevated temperatures due to longer residence time and increased heat uptake. As a result, Diamond structures exhibit a more uniform temperature distribution, consistent with their more homogeneous velocity field. In contrast, Gyroid structures develop a high-velocity core along the flow direction, creating a colder region surrounded by warmer fluid.

These low-temperature zones extend downstream of the Gyroid structures, resulting in a less uniform temperature distribution in the wake. As the unit cell size decreases, this inhomogeneity becomes less pronounced and nearly disappears in the 5G case, due to a combination of a more orderly flow pattern and enhanced heat transfer per unit fluid volume. In the Diamond structures, a small region of thermal inhomogeneity can also be observed downstream. However, the overall temperature distribution remains significantly more uniform than in the Gyroid structures. As with the Gyroid cases, this residual inhomogeneity diminishes with decreasing unit cell size, leading to an increasingly uniform thermal field.

The different temperature distributions observed across the various cases have a direct influence on the wall heat flux, which is governed by the temperature gradient normal to the wall surface (see Section 2.2). In regions where the thermal boundary layer is relatively thick and the fluid temperature near the wall is relatively high, the local temperature gradient is reduced, leading to a lower local wall heat flux. This relationship is illustrated in Figure 6.10, which shows the wall heat flux distributions for the 5G, 5D, 10G, 10D, 15G, and 15D cases.

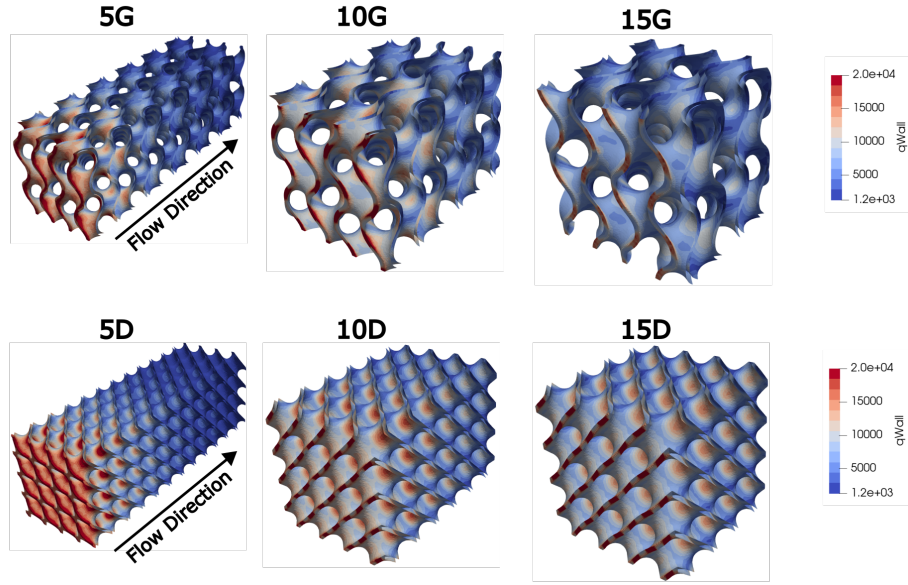


**Figure 6.10:** Distribution of the wall heat flux on the surface of the G, 5D, 10G, 10D, 15G, and 15D cases

It can be observed that the wall heat flux decreases along the flow direction, which can be attributed to the reduction in the temperature gradient as the fluid progressively heats up. This effect is more pronounced in structures with smaller unit cell sizes, where the enhanced heat transfer per unit volume leads to a faster temperature rise in the fluid, thus diminishing the wall-to-fluid temperature gradient more rapidly.

A comparison between the different topologies shows that both the Gyroid and Diamond structures exhibit high wall heat flux values on the surfaces directly facing the incoming flow. Beyond this entry region, however, the regions of elevated heat flux mimics the regions of high local wall shear stress. Similar findings were also reported by Li et al. [30]. This is to be expected, as regions of high wall shear stress correspond, by definition, to regions with a steep velocity gradient at the wall. This steep gradient leads to a breakdown of the thermal boundary layer and the observed increased wall heat flux.

## 6.4 Parametric study Results

The analyses in the previous sections have demonstrated that both internal topology and unit cell size play a critical role in shaping the flow behavior and thermal distribution within TPMS structures. Distinct differences were observed between the Gyroid and Diamond configurations, as well as across the range of unit cell sizes. While these findings offer valuable qualitative insight into the underlying mechanisms, they do not fully quantify the impact of varying unit cell size on overall system performance. To address this, a parametric study is carried out, focusing on key performance indicators. The results of this study are presented in the following section and provide a more comprehensive understanding of the design trade-offs associated with modifying unit cell size.

### 6.4.1 hydraulic metrics

The overall performance of the individual depends on both the hydraulic and thermal performance. For the hydraulic performance the pressure drop is the main influencing factor, since it directly correlates to the amount of power needed ( $W_{pump} = \Delta P \dot{m} / \rho$ ) to force the flow through the TPMS structure at the given flow conditions. In wall-bounded flows such as those within TPMS structures, the pressure drop is governed by internal pressure losses and viscous friction, which depends on the wall shear stress on the solid-fluid interface. To illustrate the latter, Figure 6.11 presents the average wall shear stress and the corresponding pressure drop for all investigated cases.

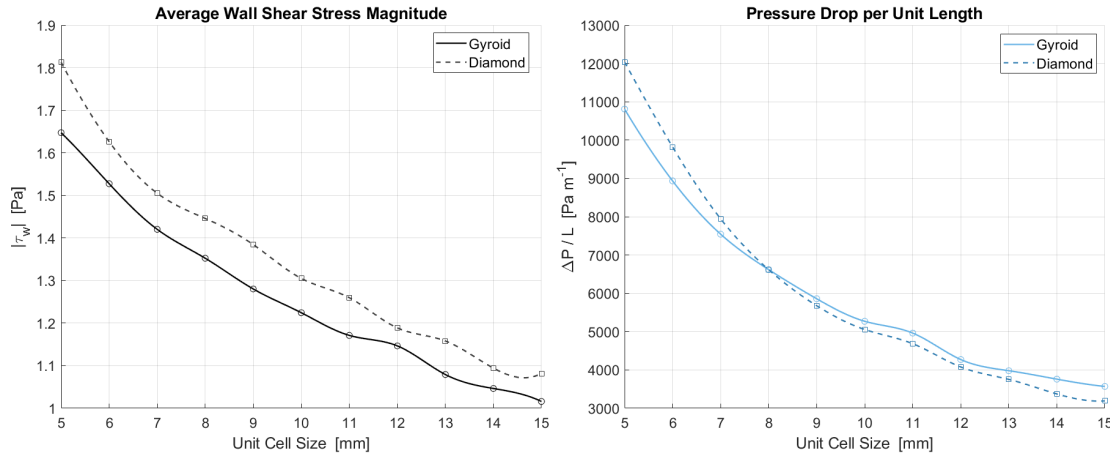


**Figure 6.11:** The left figure shows the average Wall shear stress magnitude for all cases. The right plot shows the pressure drop per unit length over the TPMS structures.

Figure 6.11 supports the observation made in Section 6.2 that wall shear stress decreases exponentially with increasing unit cell size, due to the more gradual velocity profiles found in larger unit cell configurations, which reduce the velocity gradient near the wall. For the Diamond structures, the average wall shear stress decreases by approximately 40 %, from 1.81 Pa in the 5D case to 1.08 Pa in the 15D case. A similar trend is observed for the Gyroid structures, where the wall shear stress drops by about 38 %, from 1.65 Pa to 1.02 Pa.

It can also be observed that the average wall shear stress across the TPMS structures is higher for the Diamond topologies, despite the Gyroid structures exhibiting steeper local velocity gradients. While the Gyroid geometry produces more extreme local peaks in wall shear stress due to its complex flow paths, these high-shear regions are less frequent. In contrast, the Diamond structures feature a greater number of moderate-to-high shear zones, which results in a higher average wall shear stress for the Diamond configurations.

The pressure drop follows a similar behavior as the wall shear stress curve, where finer unit cell configurations exhibit a higher pressure drop while larger cells exhibit a lower one, because lower wall shear stress decreases the amount of pressure loss due to skin friction. In the Diamond topology, increasing the cell size from 5D to 15D reduces the pressure drop by approximately 73 %, from 12037 Pa/m to 3192 Pa/m. In the Gyroid topology, the pressure drop decreases from 10809 Pa/m in the 5G case to 3570 Pa/m in the 15G case, corresponding to a 66 % reduction. The slightly smaller percentage reduction

observed for the Gyroid indicates that its pressure loss penalty is less sensitive to unit-cell size than that of the Diamond structure.

A detailed comparison of the pressure-drop curves for the Gyroid and Diamond topologies reveals that at the smallest unit-cell size (5 mm), the Diamond lattice exhibits a pressure drop approximately 10% higher than that of the Gyroid. This value is close to the 8.5% difference in their average wall-shear stresses, indicating that viscous friction at the walls is the primary contributor to the observed pressure-drop disparity. However, as the cell size increases, the pressure-drop curves for both geometries converge, overlapping at a unit-cell size of 8 mm. Beyond this point, the Gyroid topology consistently exhibits higher pressure drops for all larger unit-cell sizes. This behaviour is not reflected in the wall-shear-stress curves, which do not intersect, thereby indicating that other mechanisms influencing the pressure drop become more impactful as the unit cell size increases. Cheng et al. described the contributors to the pressure drop in TPMS geometries to be viscous friction, a continuous change in flow direction, and flow acceleration, deceleration, and recirculation [9].

As described in Section 6.2, recirculation zones develop in the Gyroid structures but are absent in the Diamond topologies. In the smaller unit-cell sizes, these zones are weak or even nonexistent, leading to viscous forces dominating the pressure drop. As the cell size increases, recirculation intensifies, and internal forces (inertial drag) contribute more to the overall pressure drop. Consequently, although the Gyroid exhibits a lower pressure drop at small cell sizes, its reduction in pressure drop with increasing cell size is less steep than that of the Diamond geometries, leading to the eventual intersection at a cell size of 8 mm and the higher pressure drop in the Gyroid structure beyond that point.

An important design parameter for porous structures that results directly from the pressure drop is the permeability. For porous media the permeability can be calculated from Darcy's law by rearranging the relationship  $\Delta P/L = \mu U/k$ , which gives  $k = \mu U L/\Delta P$ , in which  $\Delta P/L$  is the pressure gradient along the flow direction,  $\mu$  is the dynamic viscosity of the fluid,  $U$  is the superficial velocity (i.e., volumetric flow rate divided by cross-sectional area),  $L$  is the length over which the pressure drop  $\Delta P$  is measured, and  $k$  (with units of  $\text{m}^2$ ) quantifies how easily fluid passes through the porous network. The resulting values for  $k$  over the tested range of unit cell sizes are shown in Figure 6.12

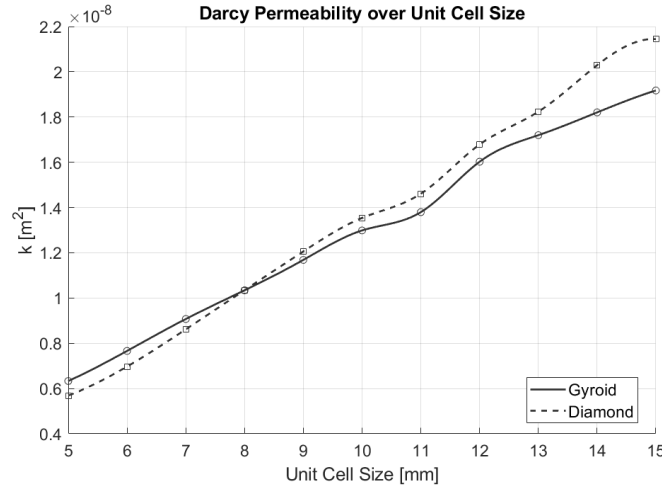


**Figure 6.12:** Permeability calculated using Darcy’s law plotted over the unit cell sizes for both Diamond and Gyroid topologies

It can be seen that the permeability exhibits a linear behaviour. When the unit cell size is small the pores are narrow, which impedes the flow and keeps permeability low. As the unit cell size increases, channels become wider and permeability rises. In the Diamond topology permeability increases from approximately  $0.6 \times 10^{-8} \text{ m}^2$  at 5 mm to about  $2.2 \times 10^{-8} \text{ m}^2$  at 15 mm representing an increase of about 267%. In the Gyroid topology permeability rises from around  $0.56 \times 10^{-8} \text{ m}^2$  at 5 mm to roughly  $1.9 \times 10^{-8} \text{ m}^2$  at 15 mm corresponding to an increase of about 239%. Furthermore, the Diamond and Gyroid curves cross at 8 mm, which is the same point where their pressure drop curves meet. This is to be expected, due to the inverse proportionality of the Permeability to the pressure drop.

#### 6.4.2 thermal metrics

Beyond hydraulic resistance, the thermal performance of a TPMS heat sink is equally critical to its overall effectiveness. In particular, the device’s ability to raise the fluid temperature as it traverses the porous network directly determines how much heat can be extracted from the solid matrix. This temperature increase is shown in Figure 6.13 for all investigated cases, as the difference between the inlet temperature (298 K) and the outlet temperature.

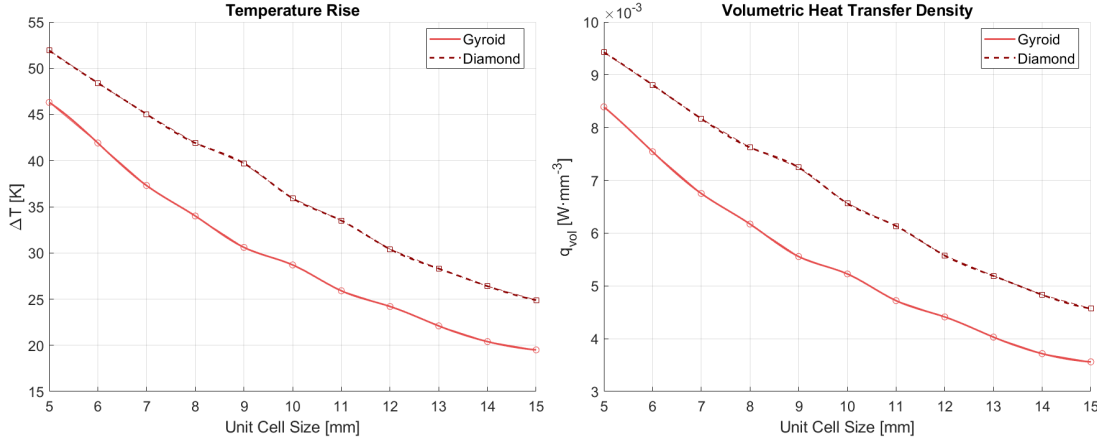


**Figure 6.13:** The left figure shows the outlet temperature for each case, and the right figure shows the volumetric heat-transfer rate plotted against unit-cell size for both Gyroid and Diamond.

It can be seen that as the unit cell size decreases, the temperature difference becomes progressively larger. In the Diamond topology, the 5D case produces a 52 K temperature increase, which is 52 % higher than the 15D case (25 K). A similar trend appears in the Gyroid structures, where the 5G case yields a 46.3 K rise throughout the structure, compared to only 19.5 K for the 15G case, corresponding to a 57 % difference. This behaviour can be attributed to the increased specific surface area of smaller unit cells, providing more heat transfer area per unit volume.

Furthermore, the Diamond topology consistently yields a greater temperature increase than the Gyroid topology. Across all unit-cell sizes, Diamond structures achieve a 6–9 K temperature rise, 11–17 % higher than their Gyroid counterparts. This increase mirrors the Diamond topology’s roughly 15 % larger specific surface area compared to the Gyroid, indicating that the higher specific surface area is the main factor driving the observed difference in temperature rise between the topologies.

The increase in the fluid temperature through the TPMS structures is directly related to the heat transferred to the fluid  $\dot{Q}$  by the relation  $\dot{Q} = \Delta T(\dot{m} c_p)$ , where  $\dot{m}$  is the mass flow rate of the fluid, and  $c_p$  is the fluid’s specific heat capacity. To account for variations in the domain volume and enable a more accurate comparison, the volumetric heat-transfer rate is employed instead of the total heat-transfer rate  $\dot{Q}$ . It is defined as  $q_{vol} = \dot{Q}/V_{fluid}$ , where  $V_{fluid}$  denotes the fluid volume within the TPMS domain. This volumetric heat-transfer rate is also shown in Figure 6.13.

Because  $q_{vol}$  scales directly with  $\Delta T$ , it exhibits the same trends, where smaller unit-cell sizes produce higher volumetric heat-transfer rates, and for any given size, the Diamond topology outperforms the Gyroid in heat transport per unit volume. The reason the two curves match so closely is that the only factor significantly changing with cell size is the temperature rise,  $\Delta T$ . In the chosen design, as the cells get larger, both the fluid volume and the flow area increase together, keeping the mass-flow to volume ratio,  $\dot{m}/V_{fluid}$ , nearly constant. Therefore, since the volumetric heat density is  $q_{vol} = (\dot{m} c_p \Delta T)/V_{fluid}$ , any change in  $q_{vol}$  comes nearly entirely from  $\Delta T$ .

This behavior is reflected in the percentage differences, where in the Diamond topology, the 5D case reaches a volumetric heat-transfer density of  $0.00943 \text{ W/mm}^3$ , about 52 % higher than the 15D case at  $0.00457 \text{ W/mm}^3$ . In the Gyroid topologies, the 5G configuration delivers  $0.00839 \text{ W/mm}^3$  compared to  $0.00356 \text{ W/mm}^3$  for the 15G case, a 58 % improvement. Likewise, the difference between the Diamond and Gyroid topologies is between  $0.001 \text{ W/mm}^3$  and  $0.0018 \text{ W/mm}^3$  or 10 %-19 %.

### 6.4.3 dimensionless Analysis

Up to now, the focus has been on the total metrics, such as the absolute pressure drop  $\Delta P$  and the total volumetric heat transfer rate  $\dot{q}_{vol}$  through each TPMS sample. While these quantities are useful for gaging the energy needed and the amount of heat moved for each specific case, they depend directly on the geometry, sample size, and flow conditions. To allow for better comparison between other geometries and other flow conditions, dimensionless performance metrics are employed that remove those scale effects. This section specifically focuses on the Nusselt number,  $Nu$ , which characterizes the convective heat-transfer strength relative to conduction, and the Darcy friction factor,  $f$ , which measures hydraulic resistance independent of sample length or flow conditions. These dimensionless measures are shown in Figure 6.14 for all investigated cases.

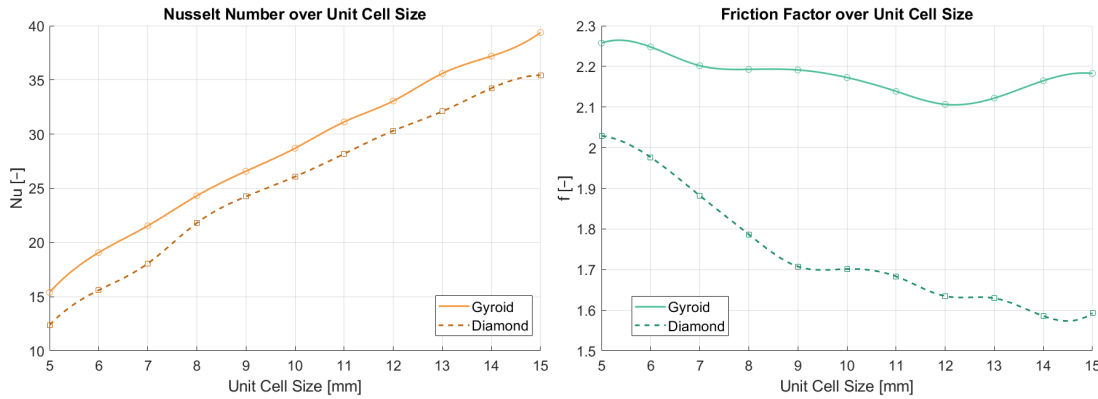


**Figure 6.14:** The left figure shows the average Nusselt number for each case, and the right figure shows the friction factor plotted over the unit cell size for both Gyroid and Diamond

The Nusselt number shown in the figure is obtained by first evaluating its local value on every surface cell of the TPMS geometry, as explained in Section 2.2, and then averaging these values over the entire interface. It can be seen that for both Gyroid and Diamond topologies, the surface-averaged Nusselt number rises close to linearly with the unit-cell size. In the Diamond lattice,  $Nu$  increases from 12.4 for the 5D configuration to 35.4 for 15D, which corresponds to a 186 % gain. The Gyroid exhibits a similar trend, where  $Nu$  grows from 11.5 at 5G to 39.4 at 15G, a rise of 156 %.

Unlike the volumetric heat-transfer  $\dot{q}_{vol}$ , which decreases as the unit-cell size increases, the Nusselt number grows because it is proportional to the hydraulic diameter ( $Nu \propto d_h$ ). As shown in Section 6.1, enlarging the unit-cell edge from 5 mm to 15 mm increases  $d_h$  by about 190 % for the Gyroid lattice and 195 % for the Diamond lattice. This enlargement is the main cause of the observed rise in  $Nu$ . Physically, the larger hydraulic diameter lets

forced convection account for a greater share of the heat transfer relative to fluid conduction. However, simultaneously, the surface-area-to-volume ratio drops, leading to a lower volumetric heat-transfer capacity of the entire structure, even though the local Nusselt number is higher. The same phenomenon can also explain the higher Nusselt number in the Gyroid cases over the Diamond topologies, as they possess higher hydraulic diameters for the same unit cell size.

These observations are further supported by Figure 6.15, which shows the heat transfer coefficient over the whole TPMS structure for all investigated cases.

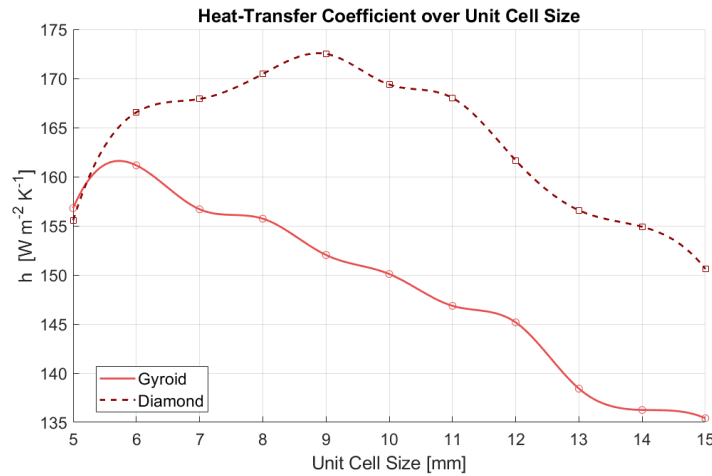


**Figure 6.15:** Average heat transfer coefficient plotted over the unit cell size, for both Gyroid and Diamond

Figure 6.15 shows that the convective heat-transfer coefficient  $h$  changes by only about 20 % between its lowest and highest values for both topologies, confirming that the hydraulic diameter is the dominant factor governing the scaling of the Nusselt number.

It can also be observed that for both the Gyroid and Diamond topologies, increasing the unit cell size from its minimum of 5 mm, leads to a rise in  $h$  up to a maximum, after which the heat transfer coefficient decreases steadily. This trend results from two opposing effects. As the unit cell size, and therefore the hydraulic diameter, increases, the local Reynolds number grows, which intensifies fluid mixing and thins the thermal boundary layer, thereby enhancing heat transfer. At the same time the specific surface area falls, reducing the heat-exchange area. Once this loss outweighs the Reynolds-number benefit, the coefficient begins to drop steadily.

For the Gyroid structures, the maximum appears at a unit cell size of 6 mm, whereas for the Diamond cases it shifts to 9 mm due to their generally lower hydraulic diameter. Overall, the Diamond structures deliver higher heat-transfer coefficients than the Gyroids, which is consistent with the previous observations of other thermal parameters. However, at the smallest unit cell size of 5 mm the Diamond topology shows a lower heat transfer coefficient than the Gyroid because, as demonstrated in Section 6.2, it is the only configuration in which turbulent kinetic energy declines along the flow path. The resulting weak turbulence, caused by the very small hydraulic diameter, keeps the thermal boundary layer stable and thus reduces the heat transfer coefficient.

The second unitless quantity considered is the Darcy friction factor shown in Figure 6.14. For porous media it can be written as  $f = C_v/Re + C_i$  where the first term represents viscous resistance and the second term represents inertial or form drag as explained in Section 2.2 [13].

The friction factor of the Gyroid topologies displays an almost constant behaviour throughout the investigated range. The value falls slightly as the unit cell size increases to 12 mm and then rises again. However, the overall variation remains within 7%. The near constant behaviour of the friction factor reveals an only small dependence on  $Re$ , indicating that inertial drag governs the hydraulic resistance of the Gyroid topology. Similar observations were made by Khalil et al. [29], who found that the friction factor in Gyroid sheet structures is nearly independent of  $Re$  for inlet Reynolds numbers over 4000. They further link this observation to form drag dominating the pressure drop.

The Diamond topologies portray a different behaviour. Here, the friction factor falls more steeply until a unit cell size of 9 mm, before subsequently leveling out. This initial reduction is driven by the rise in Reynolds number that accompanies the larger hydraulic diameter which indicates that viscous drag is a significant contributor to the hydraulic resistance in this range. Beyond 9D, the inertial term becomes the prevailing component, and the friction factor approaches a constant value.

A comparison between the two topologies shows, that the friction factor of the Gyroid structures is higher throughout all cases, due to their higher inertial pressure loss.

#### 6.4.4 Efficiency Metrics

The thermal and hydraulic performance of the system can be evaluated using both performance and efficiency metrics. A common approach to assess performance is to normalize the volumetric heat transfer rate by the required pumping power. This provides a direct measure of how effectively thermal energy is transferred to the fluid relative to the energy input needed to overcome hydraulic resistance. These metrics are illustrated in Figure 6.16.

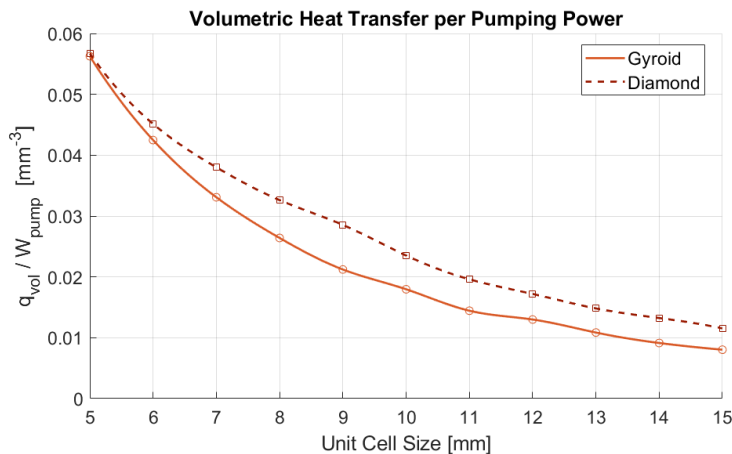


**Figure 6.16:** Heat transfer rate normalized by the pumping power plotted over the unit cell size for Gyroid and Diamond

In the normalized volumetric heat transfer rate plot, a clear trend can be observed for both topologies. As the unit cell size increases, the value of  $\frac{\dot{q}_{\text{vol}}}{W_{\text{pump}}}$  decreases, indicating that larger unit cells require more pumping power to transfer the same amount of heat to an equivalent volume of fluid. For the Gyroid topology, the volumetric performance decreases by 85 %, from  $0.056 \frac{W_Q}{W_P \text{ mm}^3}$  to  $0.008 \frac{W_Q}{W_P \text{ mm}^3}$  between 5G and 15G. Similarly, an 80 % decrease is observed for the Diamond structure, from  $0.056 \frac{W_Q}{W_P \text{ mm}^3}$  to  $0.011 \frac{W_Q}{W_P \text{ mm}^3}$  between 5D and 15D. This suggests that the benefit of reduced pressure drop, due to lower viscous friction and wider flow pathways, is offset by the accompanying reduction in solid–fluid interface area.

A comparison between the Gyroid and Diamond topologies shows that both exhibit similar volumetric performance at a unit cell size of 5 mm. However, as the unit cell size increases, their performance begins to diverge, with the Diamond topology maintaining higher performance values, until, at larger unit cell sizes, the two trends appear to decrease in parallel. The generally lower performance observed for the Gyroid at larger scales suggests that the relatively higher surface area of the Diamond structure becomes increasingly beneficial as scale increases. Additionally, the slightly steeper decline in the Gyroid curve indicates that the impact of unit cell size on volumetric heat transfer performance is more pronounced for the Gyroid topology.

Normalizing the volumetric heat transfer rate by the required pumping power is a common way to evaluate how effectively thermal energy is transferred relative to the energy required to overcome flow resistance. However, since the volumetric flow rate and thus the pumping power scale with the cross-sectional area of the domain, this normalization does not account for the influence of domain size. Instead, it reinforces the effect, because the volumetric flow rate, and thereby the pumping power, scale with the cross-sectional area. To better compare the thermal-hydraulic performance independently of domain scaling, the volumetric heat transfer rate is normalized by the pressure drop using the metric  $\text{eff}_P = \dot{q}_{\text{vol}} / \Delta P^{1/3}$ . Here, the exponent 1/3 reflects the scaling relationship under constant pumping power conditions, as discussed in Section 2.2. Hence, this metric describes how much volumetric heat transfer can be achieved per unit of hydraulic resistance, adjusted to reflect an equal power input across different cases

Another dimensionless efficiency metric that aims to isolate the influence of fluid and thermal transport behavior from geometric scaling effects is the thermo-hydraulic efficiency index,  $\eta$ , which achieves this by relating the Nusselt number to the friction factor. Both metrics are shown in Figure 6.17 for all investigated cases.

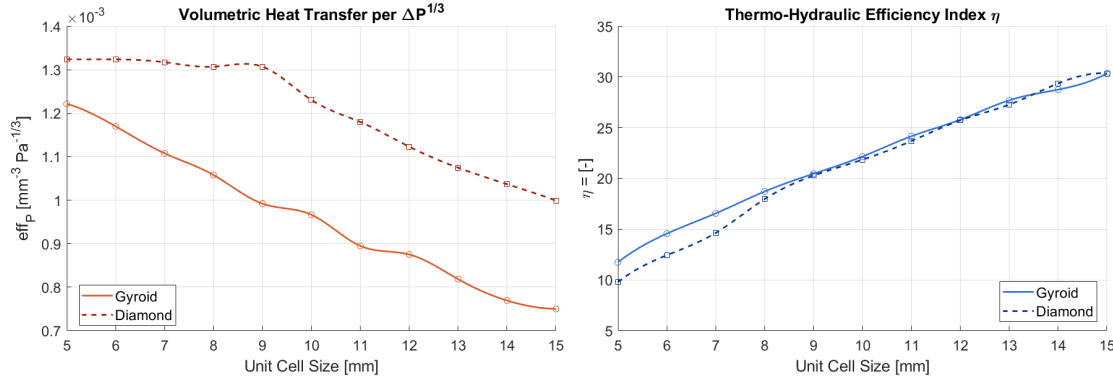


**Figure 6.17:** The left figure shows the volumetric heat transfer rate normalized by the pressure drop plotted over the unit cell size, and the right figure shows the thermo-hydraulic efficiency index plotted over the unit cell size.

A clear difference in the trends of heat transfer per hydraulic resistance can be observed between the Diamond and Gyroid topologies. For the Gyroid structures,  $eff_P$  decreases approximately linearly with increasing unit cell size, indicating that larger unit cells require more pumping power to transfer the same amount of heat per unit volume of fluid. In contrast, the Diamond structures exhibit a different behavior, where  $eff_P$  remains relatively constant up to a unit cell size of 9 mm, after which it begins to decline. This suggests that, for Diamond structures up to 9D, increasing the unit cell size does not significantly impact the pumping power required to maintain the same volumetric heat transfer, whereas after this point, performance begins to drop.

Since it was previously shown that the volumetric heat transfer rate decreases almost identically for both topologies, the differing trends in  $eff_P$  can primarily be attributed to variations in pressure losses. A comparison with the friction factors reveals that the  $eff_P$  curves resemble an inverted and rescaled version of the friction factor trends. The nearly constant friction factor observed for the Gyroid structures, as well as for larger unit cells in the Diamond topology, results in a continuous decline in volumetric heat transfer per pressure input. Conversely, the steadily decreasing friction factor found in the Diamond structures at smaller unit cell sizes leads to a relatively constant behavior in  $eff_P$ . This suggests that the trends in volumetric thermal performance per pressure input are primarily governed by the rate at which hydraulic resistance decreases. In topologies where the friction factor drops significantly with unit cell size, the resulting lower pressure losses help maintain a higher  $eff_P$  despite decreasing heat transfer rates.

A more in-depth comparison of the topologies shows that the Diamond topology consistently exhibits higher volumetric heat transfer performance per pressure input than the Gyroid. While the advantage is moderate at small scales, around 8%, it becomes significantly more pronounced at larger unit cell sizes, reaching nearly 40%. This generally higher  $eff_P$  observed for the Diamond structures is in agreement with their overall higher volumetric heat transfer rates. In addition, the increasingly pronounced advantage at larger unit cell sizes corresponds to the behavior of the pressure drop, where, although the Diamond structures exhibit a higher pressure drop at small unit cell sizes, their hydraulic resistance decreases more rapidly with increasing size and eventually becomes lower than that of the Gyroid structures. This sharper reduction in pressure drop contributes to the

improved  $eff_p$  of the Diamond topology at larger unit cell sizes.

The second efficiency metric shown in Figure 6.17 is the thermo-hydraulic efficiency index,  $\eta$ , which combines the dimensionless Nusselt number and the friction factor. At smaller unit cell sizes,  $\eta$  is slightly higher for the Diamond structures, but both topologies converge at a unit cell size of 9 mm and remain nearly identical beyond that point. In contrast to the previously discussed metrics, the thermo-hydraulic efficiency index increases with increasing unit cell size.

These contrasting behaviors highlight how different unit cell sizes are better suited for different use cases. The low  $\eta$  and high  $eff_p$  observed at smaller unit cell sizes suggest that these configurations can transfer more heat per unit volume at a given pumping power, albeit at the cost of lower energy efficiency. This is primarily due to their higher specific surface area, which enhances heat transfer but increases the pressure loss. In contrast, larger unit cell sizes exhibit higher thermo-hydraulic efficiency, indicating more effective energy usage due to their improved convective transport. However, they are less capable of achieving the same volumetric heat transfer performance as smaller unit cells.

## Chapter 7

# Conclusion

In this study, the influence of unit cell size on both the thermal and hydraulic performance of two types of Triply Periodic Minimal Surface (TPMS) sheet structures, namely Gyroid and Diamond configurations, was investigated. A parametric study was conducted to systematically evaluate the effects of varying unit cell sizes across both topologies. The analysis was performed using Computational Fluid Dynamics (CFD) simulations under the assumption of incompressible flow. As the governing equations, the Reynolds-Averaged Navier-Stokes (RANS) and energy equations were employed, with turbulence modeled using the  $k-\omega$  Shear Stress Transport (SST) turbulence model, which is particularly effective at capturing near-wall phenomena.

A constant inlet velocity of 3.7 m/s was imposed for all cases. Air was selected as the working fluid, entering the domain at a temperature of 298 K, while the TPMS walls were maintained at a uniform temperature of 353 K. To isolate the influence of unit cell size, the porosity was fixed at 80 % across all geometries, thereby maintaining a constant solid-to-fluid volume ratio. Periodic boundary conditions were applied in the transverse directions to eliminate channel wall effects, and the length of the TPMS region in the streamwise direction was held constant in all cases to provide direct comparability of the pressure drop.

To ensure the reliability and accuracy of the simulation results, a grid independence study was conducted using the Grid Convergence Index (GCI) method, which provided a quantitative estimate of the discretization error. This error was estimated to be below 5 %, indicating sufficient grid resolution for accurate results. Furthermore, verification of the incompressibility assumption was performed by comparing the results of incompressible and compressible CFD simulations. The maximum deviation observed between the two approaches was less than 3 %, confirming that the incompressible formulation is appropriate for the flow conditions considered in this study.

Finally, the simulation framework was validated against both experimental and numerical data from existing literature. The predicted Nusselt numbers differed by less than 10 % from published numerical results, and the pressure drop showed a deviation of no more than 5 % compared to experimental measurements. These small discrepancies give a high level of confidence accuracy of the simulation results and demonstrate the reliability of the computational approach.

Analysis of the flow structure showed that the Diamond geometry promoted smoother and more uniform flow paths, while the Gyroid structure generated stronger velocity gradients and localized recirculation zones, leading to increased turbulent kinetic energy. Additionally, it was observed that decreasing the unit cell size resulted in more orderly flow patterns due to their reduced hydraulic diameter, which dampens turbulence intensity and stabilizes the flow field.

A reduction in unit cell size consistently led to an increase in pressure drop for both topologies. From the largest to the smallest unit cell, the pressure drop increased by approximately 73 % for the Diamond structure and 66 % for the Gyroid structure. A comparison between the two revealed an intersection in their pressure drop trends. At unit cell sizes below 9 mm, Diamond structures exhibited up to 10 % higher pressure losses than Gyroid structures. However, beyond this point, the Gyroid configurations showed higher pressure drops. This shift was linked to the development of strong recirculation zones in the larger Gyroid cells, which were largely absent in the Diamond structures.

Friction factor analysis further supported these observations. For the Diamond topology, the friction factor decreased steadily with increasing unit cell size up to 9 mm, after which it stabilized. In contrast, the Gyroid structures maintained an almost constant friction factor across all unit cell sizes, varying by less than 7 %. This behavior suggests that hydraulic resistance in the Gyroid topology is primarily governed by inertial effects, while in the Diamond structures, viscous effects play a more significant role, which increase with decreasing unit cell size.

Volumetric heat transfer rates were found to be significantly higher for smaller unit cell sizes, primarily due to their increased specific surface area. Compared to the largest unit cell size, the smallest unit cell achieved up to 57 % higher volumetric heat transfer. At the same unit cell size, Diamond structures consistently outperformed Gyroid structures by 11 % to 17 %, reflecting their higher specific surface area.

In contrast, the Nusselt number increased with unit cell size for both geometries. From the smallest to the largest unit cell, the Nusselt number rose by up to 186 % in the Diamond structures and 156 % in the Gyroid structures. Additionally, Gyroid structures exhibited Nusselt numbers that were consistently higher than those of Diamond structures at corresponding unit cell sizes. This inverse behavior between the Nusselt number and volumetric heat transfer is explained by the opposing influence of surface area and hydraulic diameter. While smaller unit cells provide higher specific surface areas, resulting in greater overall heat transfer, larger unit cells offer increased hydraulic diameter and promote more chaotic and turbulent flow, which enhances the convective contribution to heat transfer and thus raises the Nusselt number.

Finally, performance and efficiency were evaluated using the volumetric performance index  $eff_p$  and the thermo-hydraulic efficiency index  $\eta$ . The results showed that  $eff_p$  decreased and  $\eta$  increased with growing unit cell size for both topologies, reflecting a trade-off between volumetric heat transfer and energy efficiency. Overall, Diamond structures exhibited up to 40 % higher  $eff_p$  while having virtually the same  $\eta$ .

These results showed that Diamond topologies were generally more effective than Gyroid structures across a broad range of unit cell sizes. Additionally, smaller unit cells consistently outperformed larger ones in terms of overall volumetric heat transfer, making them well-suited for applications where space is limited and high heat removal rates are required. Conversely, larger unit cells demonstrated higher thermo-hydraulic efficiency, which makes them more applicable for scenarios where spatial constraints are less critical and energy-efficient heat transfer is prioritized.

## Chapter 8

### Future work

This study investigated the performance of the Gyroid and Diamond type Triply Periodic Minimal Surfaces, across a wide range of unit cell sizes, with the lattices being kept at a constant wall temperature.

Future investigations could build on this study by exploring how variations in unit cell size influence thermal and hydraulic performance under alternative boundary conditions. This includes cases such as constant heat flux inputs or full conjugate heat transfer setups, which would allow for a more comprehensive understanding of thermal behavior in realistic applications.

In addition, the study could be expanded to include other TPMS geometries beyond the Gyroid and Diamond types. Investigating structures such as Primitive, Neovius, or I-WP could reveal how different topological features interact with cell size and affect flow development, pressure drop, and heat transfer.

The impact of manufacturing-related surface irregularities should also be considered. In practice, surface roughness introduced by additive manufacturing techniques such as 3D printing can significantly alter local flow characteristics. This effect is especially relevant for small unit cell sizes, where even minor roughness can disrupt boundary layers and increase pressure losses.

Finally, further work could evaluate how the choice of material influences performance across different unit cell sizes. Since thermal conductivity and surface energy vary widely between metals, polymers, and ceramics, material selection may play a crucial role in determining the overall efficiency and suitability of TPMS heat sinks for specific applications.

# Bibliography

- [1] Diab W. Abueidda, Rashid K. Abu Al-Rub, Ahmed S. Dalaq, Dong Wook Lee, Kamran A. Khan, and Iwona Jasiuk. Effective conductivities and elastic moduli of novel foams with triply periodic minimal surfaces. *Mechanics of Materials*, 95:102–115, 4 2016. ISSN 01676636. doi: 10.1016/j.mechmat.2016.01.004.
- [2] Oraib Al-Ketan, Mohamed Ali, Mohamad Khalil, Reza Rowshan, Kamran A. Khan, and Rashid K. Abu Al-Rub. Forced convection computational fluid dynamics analysis of architected and three-dimensional printable heat sinks based on triply periodic minimal surfaces. *Journal of Thermal Science and Engineering Applications*, 13, 4 2021. ISSN 19485093. doi: 10.1115/1.4047385.
- [3] Alessandro V. Anacreonte, Marcello Iasiello, Gerardo M. Mauro, Nicola Bianco, and Wilson K.S. Chiu. Pore-scale multi-objective shape optimization of triply periodic minimal surface cellular architectures: Volumetric nusselt number versus friction factor. *International Journal of Heat and Mass Transfer*, 236, 1 2025. ISSN 00179310. doi: 10.1016/j.ijheatmasstransfer.2024.126318.
- [4] Danish Ansari and Christophe Duwig. A gyroid tpms heat sink for electronic cooling. *Energy Conversion and Management*, 319, 11 2024. ISSN 01968904. doi: 10.1016/j.enconman.2024.118918.
- [5] Reza Attarzadeh, Marc Rovira, and Christophe Duwig. Design analysis of the "schwartz d" based heat exchanger: A numerical study. *International Journal of Heat and Mass Transfer*, 177, 10 2021. ISSN 00179310. doi: 10.1016/j.ijheatmasstransfer.2021.121415.
- [6] Nada Baobaid, Mohamed I. Ali, Kamran A. Khan, and Rashid K. Abu Al-Rub. Fluid flow and heat transfer of porous tpms architected heat sinks in free convection environment. *Case Studies in Thermal Engineering*, 33, 5 2022. ISSN 2214157X. doi: 10.1016/j.csite.2022.101944.
- [7] Giovanni Brambati, Manfredo Guilizzoni, and Stefano Foletti. Convective heat transfer correlations for triply periodic minimal surfaces based heat exchangers. *Applied Thermal Engineering*, 242, 4 2024. ISSN 13594311. doi: 10.1016/j.applthermaleng.2024.122492.
- [8] S. Catchpole-Smith, R. R.J. Sélo, A. W. Davis, I. A. Ashcroft, C. J. Tuck, and A. Clare. Thermal conductivity of tpms lattice structures manufactured via laser powder bed fusion. *Additive Manufacturing*, 30, 12 2019. ISSN 22148604. doi: 10.1016/j.addma.2019.100846.
- [9] Zhilong Cheng, Ruina Xu, and Pei Xue Jiang. Morphology, flow and heat transfer in triply periodic minimal surface based porous structures. *International Journal of Heat and Mass Transfer*, 170, 5 2021. ISSN 00179310. doi: 10.1016/j.ijheatmasstransfer.2021.120902.

- [10] Antariksh Dicholkar, Frederik Zahle, and Niels N. Sørensen. Convergence enhancement of simple-like steady-state rans solvers applied to airfoil and cylinder flows. *Journal of Wind Engineering and Industrial Aerodynamics*, 220:104863, 2022. doi: 10.1016/j.jweia.2021.104863.
- [11] Boris Diskin and James L. Thomas. Effects of mesh irregularities on accuracy of finite-volume discretization schemes. Technical report, National Institute of Aerospace and NASA Langley Research Center, n.d. Unpublished technical report supported by NASA Fundamental Aeronautics Program, Supersonics Project, Contract NNL07AA23C.
- [12] Anton du Plessis, Nima Razavi, Matteo Benedetti, Simone Murchio, Martin Leary, Marcus Watson, Dhruv Bhate, and Filippo Berto. Properties and applications of additively manufactured metallic cellular materials: A review, 4 2022. ISSN 00796425.
- [13] Nihad Dukhan, Özer Bağci, and Mustafa Özdemir. Experimental flow in various porous media and reconciliation of forchheimer and ergun relations. *Experimental Thermal and Fluid Science*, 57:425–433, 2014. ISSN 08941777. doi: 10.1016/j.expthermflusci.2014.06.011.
- [14] Krzysztof Dutkowski, Marcin Kruzel, and Krzysztof Rokosz. Review of the state-of-the-art uses of minimal surfaces in heat transfer, 11 2022. ISSN 19961073.
- [15] Pawankumar Ekade and Shankar Krishnan. Fluid flow and heat transfer characteristics of octet truss lattice geometry. *International Journal of Thermal Sciences*, 137:253–261, 3 2019. ISSN 12900729. doi: 10.1016/j.ijthermalsci.2018.11.031.
- [16] Jost Hinrich Eschenburg. *Geometry - intuition and concepts: Imagining, understanding, thinking beyond. an introduction for students*. Springer Fachmedien Wiesbaden, 10 2022. doi: 10.1007/978-3-658-38640-5.
- [17] Paul J.F. Gandy and Jacek Klinowski. Nodal surface approximations to the zero equipotential surfaces for cubic lattices. *Journal of Mathematical Chemistry*, 31:1–16, 2002. ISSN 02599791. doi: 10.1023/A:1015444012997.
- [18] S. Gordeev, V. Heinzl, and R. Stieglitz. Numerical hydraulic analysis of the turbulent contraction nozzle flow for ifmif target application. *Fusion Engineering and Design*, 85: 1859–1865, 12 2010. ISSN 09203796. doi: 10.1016/j.fusengdes.2010.06.012.
- [19] Christopher Greenshields and Henry Weller. *Notes on Computational Fluid Dynamics: General Principles*. CFD Direct Ltd, Reading, UK, 2022.
- [20] E. M. Greitzer, C. S. Tan, and M. B. Graf. *Internal Flow*. Cambridge University Press, 4 2004. doi: 10.1017/cbo9780511616709.
- [21] J. Y. Ho, K. C. Leong, and T. N. Wong. Experimental and numerical investigation of forced convection heat transfer in porous lattice structures produced by selective laser melting. *International Journal of Thermal Sciences*, 137:276–287, 3 2019. ISSN 12900729. doi: 10.1016/j.ijthermalsci.2018.11.022.

- [22] Sajjad Hussain, Wan Aizon W. Ghopa, S. S.K. Singh, Abdul Hadi Azman, and Shahrum Abdullah. Experimental and numerical vibration analysis of octet-truss-lattice-based gas turbine blades. *Metals*, 12, 2 2022. ISSN 20754701. doi: 10.3390/met12020340.
- [23] Frank P. Incropera, David P. DeWitt, Theodore L. Bergman, and Adrienne S. Lavine. *Fundamentals of Heat and Mass Transfer*. John Wiley & Sons, Hoboken, NJ, 7th edition, 2011. ISBN 978-0470501979.
- [24] Jaisree Iyer, Thomas Moore, Du Nguyen, Pratanu Roy, and Joshua Stolaroff. Heat transfer and pressure drop characteristics of heat exchangers based on triply periodic minimal and periodic nodal surfaces. *Applied Thermal Engineering*, 209, 6 2022. ISSN 13594311. doi: 10.1016/j.applthermaleng.2022.118192.
- [25] Jinhee JEong and Fazle Hussain. On the identification of a vortex. *Journal of Fluid Mechanics*, 285:69–94, 1995. ISSN 14697645. doi: 10.1017/S0022112095000462.
- [26] Alistair Jones, Martin Leary, Stuart Bateman, and Mark Easton. TPMS Designer: A tool for generating and analyzing triply periodic minimal surfaces. *Software Impacts*, 10, 2021. ISSN 2665-9638. doi: 10.1016/j.simpa.2021.100167. URL <https://github.com/Alistairj43/TPMS-Designer>.
- [27] W.P Jones and B.E Launder. The prediction of laminarization with a two-equation model of turbulence. *International Journal of Heat and Mass Transfer*, 15(2):301–314, 1972. ISSN 0017-9310. doi: [https://doi.org/10.1016/0017-9310\(72\)90076-2](https://doi.org/10.1016/0017-9310(72)90076-2). URL <https://www.sciencedirect.com/science/article/pii/0017931072900762>.
- [28] Issam El Khadiri, Mohamed Abouelmajd, Maria Zemzami, Nabil Hmina, Manuel Lagache, and Soufiane Belhouideg. Comprehensive analysis of flow and heat transfer performance in triply periodic minimal surface (tpms) heat exchangers based on fischer-koch s, pmy, frd, and gyroid structures. *International Communications in Heat and Mass Transfer*, 156, 8 2024. ISSN 07351933. doi: 10.1016/j.icheatmasstransfer.2024.107617.
- [29] Mohamad Khalil, Mohamed I. Hassan Ali, Kamran A. Khan, and Rashid Abu Al-Rub. Forced convection heat transfer in heat sinks with topologies based on triply periodic minimal surfaces. *Case Studies in Thermal Engineering*, 38, 10 2022. ISSN 2214157X. doi: 10.1016/j.csite.2022.102313.
- [30] Weihong Li, Guopeng Yu, and Zhibin Yu. Bioinspired heat exchangers based on triply periodic minimal surfaces for supercritical co2 cycles. *Applied Thermal Engineering*, 179:115686, 2020. ISSN 1359-4311. doi: <https://doi.org/10.1016/j.applthermaleng.2020.115686>. URL <https://www.sciencedirect.com/science/article/pii/S1359431120331689>.
- [31] Zhensen Liu, Zetian Gao, Mingqiu Dai, Bingke Song, Biqi Yang, Tao Zhang, Shuangyin Yuan, Gang Liu, and Miao Zhao. Fluid flow and heat transfer performances of aluminum alloy lattices with triply periodic minimal surfaces. *Materials*, 18:1407, 3 2025. ISSN 1996-1944. doi: 10.3390/ma18071407.

- [32] MDPI. Mdpi open access information and policy. <https://www.mdpi.com/openaccess>, 2025. Accessed: 2025-05-23.
- [33] F. R. Menter. Two-equation eddy-viscosity turbulence models for engineering applications. *AIAA Journal*, 32:1598–1605, 8 1994. ISSN 0001-1452. doi: 10.2514/3.12149.
- [34] A. Mirabolghasemi, A. H. Akbarzadeh, D. Rodrigue, and D. Therriault. Thermal conductivity of architected cellular metamaterials. *Acta Materialia*, 174:61–80, 8 2019. ISSN 13596454. doi: 10.1016/j.actamat.2019.04.061.
- [35] H. Montazerian, M. Zhianmanesh, E. Davoodi, A. S. Milani, and M. Hoorfar. Longitudinal and radial permeability analysis of additively manufactured porous scaffolds: Effect of pore shape and porosity. *Materials and Design*, 122:146–156, 5 2017. ISSN 18734197. doi: 10.1016/j.matdes.2017.03.006.
- [36] Gian Luca Morini. Laminar-to-turbulent flow transition in microchannels. *Microscale Thermophysical Engineering*, 8:15–30, 1 2004. ISSN 10893954. doi: 10.1080/10893950490272902.
- [37] Fadwa Moukalled, Luca Mangani, and Mohamed Darwish. *The Finite Volume Method in Computational Fluid Dynamics*. Springer, Cham, 2016.
- [38] Bruce Roy Munson. *Fundamentals of fluid mechanics / Bruce R. Munson, Donald F. Young, Theodore H. Okiishi*. John Wiley, New York, third edition update.. edition, 1998. ISBN 047135502X.
- [39] E.R. Neovius. *Bestimmung Zweier Spezieller Periodischer Minimalflächen*. Akademische Abhandlungen, Helsinki, Finland, 1883.
- [40] Donald A. Nield and Adrian Bejan. *Convection in Porous Media*. Springer International Publishing, Cham, Switzerland, 5 edition, 2017. ISBN 978-3-319-49561-3. doi: 10.1007/978-3-319-49562-0.
- [41] Nuclear Energy Agency. Best practice guidelines for the use of CFD in nuclear reactor safety applications – 2024 update. Nea report, OECD Publishing, Paris, 2025.
- [42] OpenFOAM Documentation Team. User Guide: Residuals, 2024. URL <https://www.openfoam.com/documentation/guides/latest/doc/guide-solvers-residuals.html>. Accessed 5 May 2025.
- [43] OpenFOAM Foundation. Cell-limited gradient scheme, 2024. URL <https://www.openfoam.com/documentation/guides/latest/doc/guide-schemes-gradient-cell-limited.html>. OpenFOAM User Guide – Cell-limited gradient scheme in gradSchemes.
- [44] OpenFOAM Foundation. Laplacian schemes, 2024. URL <https://www.openfoam.com/documentation/guides/latest/doc/guide-schemes-sng-rad-corrected.html>. OpenFOAM User Guide – Corrected and uncorrected Laplacian schemes in fvSchemes.
- [45] OpenFOAM Foundation. klowreWallFunction boundary condition, 2025. URL <https://www.openfoam.com/documentation/guides/latest/doc/>

- guide-bcs-wall-turbulence-kLowReWallFunction.html. OpenFOAM User Guide – kLowReWallFunction wall function.
- [46] OpenFOAM Foundation. omegawallfunction boundary condition, 2025. URL <https://www.openfoam.com/documentation/guides/latest/doc/guide-bcs-wall-turbulence-omegaWallFunction.html>. OpenFOAM User Guide – omegaWallFunction wall function.
- [47] OpenFOAM Foundation. Boundary conditions: Coupled and cyclic AMI, 2025. URL <https://www.openfoam.com/documentation/guides/latest/doc/guide-bcs-coupled-cyclic-ami.html>. OpenFOAM User Guide – Coupled and Cyclic AMI boundary conditions.
- [48] OpenFOAM Foundation. faceareaWeightAMI class reference, 2025. URL [https://www.openfoam.com/documentation/guides/latest/api/faceAreaWeightAMI\\_8H.html](https://www.openfoam.com/documentation/guides/latest/api/faceAreaWeightAMI_8H.html). OpenFOAM API Reference – Programmatic Interface for the face-area-weighted AMI interpolation method.
- [49] OpenFOAM Foundation. faceskewness() function reference in cellQuality.c, 2025. URL [https://www.openfoam.com/documentation/guides/v2006/api/cellQuality\\_8C\\_source.html](https://www.openfoam.com/documentation/guides/v2006/api/cellQuality_8C_source.html). OpenFOAM API Guide – Definition of face skewness in meshQualityChecks.
- [50] OpenFOAM Foundation. snappyhexmesh utilities, 2025. URL <https://www.openfoam.com/documentation/guides/latest/doc/guide-meshing-snappyhexmesh.html>. OpenFOAM User Guide – Hybrid hexahedral/prismatic meshing with snappyHexMesh.
- [51] S. V. Patankar and D. B. Spalding. A calculation procedure for heat, mass and momentum transfer in three-dimensional parabolic flows. *International Journal of Heat and Mass Transfer*, 15:1787–1806, 1972. ISSN 00179310. doi: 10.1016/0017-9310(72)90054-3.
- [52] Brett Prussack, Ian Jentz, Tiago A. Moreira, Nicolas Woolstenhulme, Casey Jesse, Greg Nellis, and Mark Anderson. Thermal and hydraulic performance of volumetrically heated triply periodic minimal surface heaters. *Applied Thermal Engineering*, 248, 7 2024. ISSN 13594311. doi: 10.1016/j.applthermaleng.2024.123291.
- [53] Zahid Ahmed Qureshi, Salah Addin Burhan Al-Omari, Emad Elnajjar, Oraib Al-Ketan, and Rashid Abu Al-Rub. On the effect of porosity and functional grading of 3d printable triply periodic minimal surface (tpms) based architected lattices embedded with a phase change material. *International Journal of Heat and Mass Transfer*, 183, 2 2022. ISSN 00179310. doi: 10.1016/j.ijheatmasstransfer.2021.122111.
- [54] P. J. Roache. Perspective: A method for uniform reporting of grid refinement studies. *Journal of Fluids Engineering, Transactions of the ASME*, 116:405–413, 1994. ISSN 1528901X. doi: 10.1115/1.2910291.
- [55] Patrick J. Roache. Quantification of uncertainty in computational fluid dynamics. *Annual Review of Fluid Mechanics*, 29:123–160, 1997. doi: 10.1146/annurev.fluid.29.1.123.

- [56] Siti Ruhliah Lizarose Samion, Nur Haziqah Shaharuddin, and Mohamed Sukri Mat Ali. Grid convergence study for detached-eddy simulation of flow over rod-airfoil configuration using OpenFOAM. *IOP Conference Series: Materials Science and Engineering*, 491(1):012023, 2019. doi: 10.1088/1757-899X/491/1/012023. Proceedings of the 4th International Conference on Mechanical and Aeronautical Engineering (2018).
- [57] Sean Samson, Phuong Tran, and Pier Marzocca. Design and modelling of porous gyroid heatsinks: Influences of cell size, porosity and material variation. *Applied Thermal Engineering*, 235, 11 2023. ISSN 13594311. doi: 10.1016/j.applthermaleng.2023.121296.
- [58] Hermann Schlichting and Klaus Gersten. *Boundary-Layer Theory*. Springer Berlin Heidelberg, 10 2016. ISBN 9783662529195. doi: 10.1007/978-3-662-52919-5.
- [59] A. H. Schoen. Infinite periodic minimal surfaces without self-intersections, 1970.
- [60] H. A. Schwarz. *Gesammelte Mathematische Abhandlungen*. Springer Berlin Heidelberg, 1890. doi: 10.1007/978-3-642-50665-9.
- [61] Avez Shaikh, Jacklyn Griffis, Ryan Stebbins, Kazi Safowan Shahed, Ankit Saxena, Andrew Ross, and Guha Manogharan. Towards gradient design of tpms lattices and laser powder bed fusion processing– role of laser strategies and lattice thickness. *Manufacturing Letters*, 41:1046–1054, 10 2024. ISSN 22138463. doi: 10.1016/j.mfglet.2024.09.129.
- [62] M. Speirs, B. Van Hooreweder, J. Van Humbeeck, and J. P. Kruth. Fatigue behaviour of niti shape memory alloy scaffolds produced by slm, a unit cell design comparison. *Journal of the Mechanical Behavior of Biomedical Materials*, 70:53–59, 6 2017. ISSN 18780180. doi: 10.1016/j.jmbbm.2017.01.016.
- [63] Wei Tang, Hua Zhou, Yun Zeng, Minglei Yan, Chenglu Jiang, Ping Yang, Qing Li, Zhida Li, Junheng Fu, Yi Huang, and Yang Zhao. Analysis on the convective heat transfer process and performance evaluation of triply periodic minimal surface (tpms) based on diamond, gyroid and iwp. *International Journal of Heat and Mass Transfer*, 201, 2 2023. ISSN 00179310. doi: 10.1016/j.ijheatmasstransfer.2022.123642.
- [64] J. Tian, T. Kim, T. J. Lu, H. P. Hodson, D. T. Queheillalt, D. J. Sypeck, and H. N.G. Wadley. The effects of topology upon fluid-flow and heat-transfer within cellular copper structures. *International Journal of Heat and Mass Transfer*, 47:3171–3186, 7 2004. ISSN 00179310. doi: 10.1016/j.ijheatmasstransfer.2004.02.010.
- [65] University of Bologna. Transferable skills moocs. <https://www.unibo.it/en/study/course-units-transferable-skills-moocs/course-unit-catalogue/course-unit/2024/491704>, 2024. Accessed: 2025-05-27.
- [66] H. K. (Henk Kaarle) Versteeg and W. (Weeratunge) Malalasekera. *An introduction to computational fluid dynamics : the finite volume method / H.K. Versteeg and W. Malalasekera*. Longman Group, Harlow, England, 1995. ISBN 0582218845.

- [67] Jiaxuan Wang, Chenyi Qian, Xiang Qiu, Binbin Yu, Lixia Yan, Junye Shi, and Jiangping Chen. Numerical and experimental investigation of additive manufactured heat exchanger using triply periodic minimal surfaces (tpms). *Thermal Science and Engineering Progress*, 55, 10 2024. ISSN 24519049. doi: 10.1016/j.tsep.2024.103007.
- [68] Jinghan Wang, Kai Chen, Min Zeng, Ting Ma, Qiuwang Wang, and Zhilong Cheng. Assessment of flow and heat transfer of triply periodic minimal surface based heat exchangers. *Energy*, 282, 11 2023. ISSN 03605442. doi: 10.1016/j.energy.2023.128806.
- [69] Zuzanna Wawryniuk, Emila Brancewicz-Steinmetz, and Jacek Sawicki. Revolutionizing transportation: an overview of 3d printing in aviation, automotive, and space industries, 10 2024. ISSN 14333015.
- [70] H. G. Weller, G. Tabor, H. Jasak, and C. Fureby. A tensorial approach to computational continuum mechanics using object-oriented techniques. *Computers in Physics*, 12:620–631, 11 1998. ISSN 0894-1866. doi: 10.1063/1.168744.
- [71] David C. Wilcox. Reassessment of the scale-determining equation for advanced turbulence models. *AIAA Journal*, 26:1299–1310, 11 1988. ISSN 0001-1452. doi: 10.2514/3.10041.
- [72] David C.. Wilcox. *Turbulence modeling for CFD*. DCW Industries, 2010. ISBN 1928729088.
- [73] Liang Xu, Qicheng Ruan, Qingyun Shen, Lei Xi, Jianmin Gao, and Yunlong Li. Optimization design of lattice structures in internal cooling channel with variable aspect ratio of gas turbine blade. *Energies*, 14, 7 2021. ISSN 19961073. doi: 10.3390/en14133954.
- [74] Guanghan Yan, Yu Liu, Zhaoda Zhang, Mingrui Sun, Shuai Li, Xiaokai Zhang, Lannan Jiang, Sheng Xing, and Yufan Mao. Thermal-hydraulic performance of modified schwartz-diamond solid-networks triply periodic minimal surface structures. *Applied Thermal Engineering*, 249, 7 2024. ISSN 13594311. doi: 10.1016/j.applthermaleng.2024.123384.
- [75] Kirttayoth Yeranee and Yu Rao. A review of recent investigations on flow and heat transfer enhancement in cooling channels embedded with triply periodic minimal surfaces (tpms), 12 2022. ISSN 19961073.
- [76] Kirttayoth Yeranee, Chao Xu, Yu Rao, and Yueliang Zhang. Experimental and numerical study of improving flow and heat transfer in a serpentine cooling channel with topology-optimized tpms porous structures. *International Journal of Heat and Mass Transfer*, 231, 10 2024. ISSN 00179310. doi: 10.1016/j.ijheatmasstransfer.2024.125873.

# Appendix A

## Appendix

### A.1 Inflow conditions

Here the calculations of the inflow conditions are presented based on [72]

$$T_\infty = 298 \text{ K}, \quad T_w = 353 \text{ K}, \quad D_h = 0.020 \text{ m}, \quad \text{Re} = 5000$$

$$\rho = 1.184 \text{ kg/m}^3, \quad \mu = 1.85 \times 10^{-5} \text{ Pa s}$$

$$\nu = \frac{\mu}{\rho} = \frac{1.85 \times 10^{-5}}{1.184} = 1.56 \times 10^{-5} \text{ m}^2/\text{s}$$

$$\text{Re} = \frac{U D_h}{\nu} \implies U = \frac{\text{Re} \nu}{D_h}$$

$$U = \frac{5000 \times 1.56 \times 10^{-5}}{0.020} \approx 3.7 \text{ m/s}$$

### A.2 Derivation of the Transport equations for $k$ , $\epsilon$ and $\omega$

#### A.2.1 Transport equation for the Reynolds stresses

To derive the transport equation for the Reynolds stresses we start from the RANS equation and the instantaneous momentum equation for the velocity field  $u_i$ .

##### Step 1: subtraction

Subtracting the RANS equation from the instantaneous equation (with Reynolds decomposition  $u_i = \bar{u}_i + u'_i$ ,  $p = \bar{p} + p'$ ) gives

$$\frac{D(\bar{u}_i + u'_i)}{Dt} = -\frac{1}{\rho} \frac{\partial(\bar{p} + p')}{\partial x_i} + \frac{\partial}{\partial x_j} \left[ \nu \left( \frac{\partial(\bar{u}_i + u'_i)}{\partial x_j} + \frac{\partial(\bar{u}_j + u'_j)}{\partial x_i} \right) \right] - g_i \beta (\bar{T} + T'), \quad (A.1)$$

$$\frac{D\bar{u}_i}{Dt} = -\frac{1}{\rho} \frac{\partial \bar{p}}{\partial x_i} + \frac{\partial}{\partial x_j} \left[ \nu \left( \frac{\partial \bar{u}_i}{\partial x_j} + \frac{\partial \bar{u}_j}{\partial x_i} \right) - \overline{u'_i u'_j} \right] - g_i \beta \bar{T},$$

which yields the fluctuation equation

$$\frac{\partial u'_i}{\partial t} + \bar{u}_j \frac{\partial u'_i}{\partial x_j} + u'_j \frac{\partial \bar{u}_i}{\partial x_j} + u'_j \frac{\partial u'_i}{\partial x_j} = -\frac{1}{\rho} \frac{\partial p'}{\partial x_i} + \frac{\partial}{\partial x_j} \left[ \nu \left( \frac{\partial u'_i}{\partial x_j} + \frac{\partial u'_j}{\partial x_i} \right) + \overline{u'_i u'_j} \right] - g_i \beta T'. \quad (A.2)$$

Indexing the fluctuation equation with  $i$  and  $j$ , multiplying one by  $u'_j$  and the other by  $u'_i$ , summing and averaging, leads to

$$\begin{aligned} \frac{\partial \overline{u'_i u'_j}}{\partial t} + \overline{u_k} \frac{\partial \overline{u'_i u'_j}}{\partial x_k} + \overline{u'_i u'_k} \frac{\partial \overline{u_j}}{\partial x_k} + \overline{u'_j u'_k} \frac{\partial \overline{u_i}}{\partial x_k} + \frac{\partial}{\partial x_k} \overline{u'_i u'_j u'_k} \\ = -\frac{1}{\rho} \left( \overline{u'_i \frac{\partial p'}{\partial x_j}} + \overline{u'_j \frac{\partial p'}{\partial x_i}} \right) + \nu \left( \overline{u'_i \frac{\partial^2 u'_j}{\partial x_k^2}} + \overline{u'_j \frac{\partial^2 u'_i}{\partial x_k^2}} \right) \\ - \beta (g_j \overline{u'_i T'} + g_i \overline{u'_j T'}). \end{aligned} \quad (\text{A.3})$$

The pressure-strain term can be rewritten as

$$-\frac{1}{\rho} \left( \overline{u'_i \frac{\partial p'}{\partial x_j}} + \overline{u'_j \frac{\partial p'}{\partial x_i}} \right) = \frac{1}{\rho} \frac{\partial}{\partial x_k} \left( \overline{p' \delta_{ki} u'_j} + \overline{p' \delta_{kj} u'_i} \right), \quad (\text{A.4})$$

and the viscous term as

$$\nu \left( \overline{u'_i \frac{\partial^2 u'_j}{\partial x_k^2}} + \overline{u'_j \frac{\partial^2 u'_i}{\partial x_k^2}} \right) = \nu \left( \frac{\partial^2 \overline{u'_i u'_j}}{\partial x_k^2} - 2 \frac{\partial \overline{u'_i}}{\partial x_k} \frac{\partial \overline{u'_j}}{\partial x_k} \right). \quad (\text{A.5})$$

Collecting terms gives the Reynolds-stress transport equation in brief form,

$$\frac{D \overline{u'_i u'_j}}{Dt} = P_{ij} - \varepsilon_{ij} + \Pi_{ij} + D_{ij} + G_{ij}, \quad (\text{A.6})$$

where

$$P_{ij} = -\overline{u'_i u'_k} \frac{\partial \overline{u_j}}{\partial x_k} - \overline{u'_j u'_k} \frac{\partial \overline{u_i}}{\partial x_k}, \quad (\text{A.7})$$

$$\varepsilon_{ij} = 2\nu \frac{\partial \overline{u'_i}}{\partial x_k} \frac{\partial \overline{u'_j}}{\partial x_k}, \quad (\text{A.8})$$

$$\Pi_{ij} = \frac{1}{\rho} \left( \overline{p' \frac{\partial u'_i}{\partial x_j}} + \overline{p' \frac{\partial u'_j}{\partial x_i}} \right), \quad (\text{A.9})$$

$$D_{ij} = \frac{\partial}{\partial x_k} \left( \nu \frac{\partial \overline{u'_i u'_j}}{\partial x_k} - \overline{u'_i u'_j u'_k} - \frac{p'}{\rho} (\delta_{ki} u'_j + \delta_{kj} u'_i) \right), \quad (\text{A.10})$$

$$G_{ij} = -\beta (g_j \overline{u'_i T'} + g_i \overline{u'_j T'}). \quad (\text{A.11})$$

## A.2.2 Transport equation for $k$ and $\varepsilon$

Taking one-half the trace of the Reynolds-stress equation yields the  $k$ -equation:

$$\frac{Dk}{Dt} = -\overline{u'_i u'_k} \frac{\partial \overline{u_i}}{\partial x_k} - \nu \frac{\partial \overline{u'_i}}{\partial x_k} \frac{\partial \overline{u'_i}}{\partial x_k} + \frac{\partial}{\partial x_k} \left( \nu \frac{\partial k}{\partial x_k} - \frac{1}{2} \overline{u'_i u'_i u'_k} - \frac{1}{\rho} \overline{p' u'_k} \right) - \beta g_i \overline{u'_i T'}, \quad (\text{A.12})$$

or compactly

$$\frac{Dk}{Dt} = P - \varepsilon + D + G, \quad (\text{A.13})$$

with

$$P = -\overline{u'_i u'_k} \frac{\partial \bar{u}_i}{\partial x_k}, \quad (\text{A.14})$$

$$\varepsilon = \nu \frac{\partial u'_i}{\partial x_k} \frac{\partial u'_i}{\partial x_k}, \quad (\text{A.15})$$

$$D = \frac{\partial}{\partial x_k} \left( \nu \frac{\partial k}{\partial x_k} - \frac{1}{2} \overline{u'_i u'_i u'_k} - \frac{1}{\rho} \overline{p' u'_k} \right), \quad (\text{A.16})$$

$$G = -\beta g_i \overline{u'_i T'}. \quad (\text{A.17})$$

### The dissipation-rate equation

Now that we have the transport equation for the turbulent kinetic energy  $k$ , we can derive the transport equation for the dissipation rate  $\varepsilon$ , which appears in the  $k$ -transport equation. This is done by differentiating the fluctuating-velocity equation with respect to  $x_k$ , multiplying by  $2\nu \partial u'_i / \partial x_k$ , and Reynolds-averaging. One obtains

$$\begin{aligned} \frac{D\bar{\varepsilon}}{Dt} = & -2\nu \left( \overline{\frac{\partial u'_i}{\partial x_k} \frac{\partial u'_j}{\partial x_k}} + \overline{\frac{\partial u'_k}{\partial x_j} \frac{\partial u'_k}{\partial x_i}} \right) \frac{\partial \bar{u}_i}{\partial x_j} - 2\nu g_i \beta \overline{\frac{\partial T'}{\partial x_k} \frac{\partial u'_i}{\partial x_k}} \\ & - 2\nu \left( \overline{\frac{\partial u'_i}{\partial x_j} \frac{\partial u'_j}{\partial x_k}} + \overline{u'_j \frac{\partial u'_i}{\partial x_k} \frac{\partial^2 \bar{u}_i}{\partial x_j \partial x_k}} + \nu \overline{\frac{\partial^2 u'_i}{\partial x_k^2}} \right) \\ & + \frac{\partial}{\partial x_j} \left[ \nu \frac{\partial \bar{\varepsilon}}{\partial x_j} - \nu \overline{\frac{\partial u'_i}{\partial x_k} \frac{\partial u'_i}{\partial x_k}} - \frac{2\nu}{\rho} \overline{u'_i \frac{\partial p'}{\partial x_i}} \right]. \end{aligned} \quad (\text{A.18})$$

As before, we introduce the shorthand

$$\frac{D\bar{\varepsilon}}{Dt} = P_\varepsilon + G_\varepsilon - \varepsilon_\varepsilon + D_\varepsilon,$$

with

$$P_\varepsilon = -2\nu \left( \overline{\frac{\partial u'_i}{\partial x_k} \frac{\partial u'_j}{\partial x_k}} + \overline{\frac{\partial u'_k}{\partial x_j} \frac{\partial u'_k}{\partial x_i}} \right) \frac{\partial \bar{u}_i}{\partial x_j}, \quad (\text{A.19})$$

$$G_\varepsilon = -2\nu g_i \beta \overline{\frac{\partial T'}{\partial x_k} \frac{\partial u'_i}{\partial x_k}}, \quad (\text{A.20})$$

$$\varepsilon_\varepsilon = 2\nu \left( \overline{\frac{\partial u'_i}{\partial x_j} \frac{\partial u'_j}{\partial x_k}} + \overline{u'_j \frac{\partial u'_i}{\partial x_k} \frac{\partial^2 \bar{u}_i}{\partial x_j \partial x_k}} + \nu \overline{\frac{\partial^2 u'_i}{\partial x_k^2}} \right), \quad (\text{A.21})$$

$$D_\varepsilon = \frac{\partial}{\partial x_j} \left[ \nu \frac{\partial \bar{\varepsilon}}{\partial x_j} - \nu \overline{\frac{\partial u'_i}{\partial x_k} \frac{\partial u'_i}{\partial x_k}} - \frac{2\nu}{\rho} \overline{u'_i \frac{\partial p'}{\partial x_i}} \right]. \quad (\text{A.22})$$

### A.2.3 Transport equation for the specific dissipation $\omega$

The specific dissipation  $\omega$  is defined as

$$\omega = \frac{\varepsilon}{C_\mu k},$$

where  $\beta^*$  is a model constant. One obtains a transport equation for  $\omega$  by substituting  $\varepsilon = \beta^* k \omega$  into the  $\varepsilon$ -equation and then applying the product and chain rules.

$$\frac{D\omega}{Dt} = \frac{\alpha}{k} P - \beta^* \omega^2 + \frac{\partial}{\partial x_j} \left[ (\nu + \sigma_\omega \nu_t) \frac{\partial \omega}{\partial x_j} \right], \quad (\text{A.23})$$

where

$$P = -\overline{u'_i u'_k} \frac{\partial \overline{u_i}}{\partial x_k}$$

is the production of turbulent kinetic energy, and  $\alpha, \beta^*, \sigma_\omega$  are model constants chosen to recover the correct near-wall and free-stream behavior.

### A.3 Numerical methods

The method used to solve the derived governing equations is the finite-volume method, a numerical technique that discretizes the integral form of the conservation laws over control volumes. It is the preferred method for CFD over other techniques such as finite-element, because it ensures strict local conservation of mass, momentum and energy even in complex flow patterns and unstructured meshes [38].

For any conserved scalar quantity  $\phi$ , its transport over a control volume  $V$  bounded by  $\partial V$  can be written in integral form as

$$\underbrace{\frac{\partial}{\partial t} \int_V \rho \phi dV}_{\text{Transient change}} + \underbrace{\oint_{\partial V} \rho \phi \mathbf{u} \cdot d\mathbf{S}}_{\text{Convective transport}} = \underbrace{\oint_{\partial V} \Gamma \nabla \phi \cdot d\mathbf{S}}_{\text{Diffusive transport}} + \underbrace{\int_V S dV}_{\text{Volumetric source}}. \quad (\text{A.24})$$

By partitioning the domain into discrete control volumes of volume  $V_P$ , applying the divergence (Gauss) theorem to turn surface integrals into sums over each cell's faces, and approximating the surface-fluxes, the transport equation (A.24) becomes [37], for each cell  $P$ ,

$$\underbrace{V_P \frac{d(\rho \phi)_P}{dt}}_{\text{Transient change}} + \underbrace{\sum_f (\rho \phi)_f (\mathbf{u} \cdot \mathbf{S})_f}_{\text{Convective transport}} = \underbrace{\sum_f \Gamma_f (\nabla \phi)_f \cdot \mathbf{S}_f}_{\text{Diffusive transport}} + \underbrace{V_P S_P}_{\text{Volumetric source}}. \quad (\text{A.25})$$

To finalize the discretization, appropriate numerical schemes must be applied to the temporal derivative, the advective face-flux, the gradient reconstruction and the diffusive face-flux. These schemes can be classified by two key attributes: accuracy, which describes how rapidly discretization errors decrease as spatial or temporal step sizes are reduced, and stability, which determines whether numerical perturbations remain bounded or amplify as the simulation proceeds [66].

In this study, transient flow structures are of lesser importance, as the performance of heat sinks primarily depends on the mean flow behavior rather than fluctuations around the mean. Therefore, the flow was solved as a steady-state problem by setting the time derivatives to zero, as this approach accurately predicts the mean flow behavior while being significantly less computationally expensive than fully transient methods.

The advection term is described by the divergence of the convective flux over the face  $f$ . Many different methods have been developed to calculate this flux, but the most relevant

ones for this study are based on the central differencing (linear) and the upwind schemes. In the latter, information is carried along the flow direction, so the face flux is taken from the upstream cell center[37]:

$$(\mathbf{u} \cdot \mathbf{S})_f \phi_f, \quad \phi_f = \begin{cases} \phi_P, & (\mathbf{u} \cdot \mathbf{S})_f > 0, \\ \phi_N, & (\mathbf{u} \cdot \mathbf{S})_f < 0. \end{cases}$$

Here  $P$  is the cell on the downstream side of face  $f$ , and  $N$  is the neighboring cell upstream (from which the flow comes).

Due to its nature of taking the entire face value from the upstream cell center, this scheme is highly diffusive, which leads to a smearing and subsequent underestimation of sharp gradients. This and its first-order accuracy make it not suited for an accurate prediction of turbulent flow, where sharp gradients occur [66]. However, this scheme is unconditionally bounded and exceptionally stable, making it an ideal choice for the startup phase of the simulation to dampen initial spikes, oscillations, and other numerical instabilities and thereby ensuring a smooth transition to higher-order discretisations, namely the limited linear and linear upwind schemes.

Both the linear upwind and limited linear schemes reconstruct the face value by a first-order Taylor expansion about the upwind cell center  $U$  [66]

$$\phi_f = \phi_U + \psi_u \cdot [(\nabla \phi)_U \cdot (\Delta x)]$$

where  $\Delta x$  is the distance between the upwind cell center and the face ( $\Delta x = x_f - x_U$ ). The linear upwind scheme simply takes the full extrapolation (i.e.  $\psi_u = 1$ ), giving second-order accuracy. The limited linear scheme introduces a limiter  $\psi_u \in [0, 1]$  to increase stability against oscillations near sharp gradients. When  $\psi_u = 1$ , the limited-linear scheme behaves exactly like the linear-upwind scheme, while for  $\psi_u = 0$  it falls back on the first-order upwind scheme, giving it 2nd order accuracy in smooth regions.

The linear-upwind scheme offers the greatest accuracy and is therefore preferred over the limited linear scheme. However, under mesh limitations or very steep gradients, it can introduce numerical instabilities that cause the simulation to diverge. In those cases, the limiter is reduced until stability is restored.

In the linear upwind formulation, and also other parts of the system, such as the calculation of the viscous stress term or the diffusive source term, gradients need to be approximated numerically. The most widely used approach is the Gauss linear gradient scheme, which uses the face values and the divergence theorem to compute the gradients similarly to the central differencing scheme [37]

$$\nabla \phi|_P \approx \frac{1}{V_P} \sum_{f \in \partial P} \phi_f \mathbf{S}_f. \quad (\text{A.26})$$

Since this scheme reconstructs the face values purely from a linear Taylor expansion of neighboring cell centers, it is second-order accurate, and non-dissipative, but also unbounded [37]. Therefore, similar to the linear upwind scheme a limiter is applied in

regions of sharp gradients and compromised mesh quality. For this study, the cell-limiter is chosen, which uses the gradient computer by the Gauss linear scheme and extrapolation via the Taylor expansion to the faces [43]

$$\phi_f^{\text{cand}} = \phi_P + (\nabla\phi)_P \cdot (x_f - x_P) \quad (\text{A.27})$$

This extrapolated value  $\phi_f$  is then compared to the extrema of the neighbour cell centers ( $\phi_{\min/\max}(\phi_P, \phi_N)$ ). If  $\phi_f$  lies outside this range, the scheme scales the gradient back by a scaling factor  $\psi_{CM}$ , so that

$$\phi_f^{\text{cand}} = \phi_P + \psi_{CM}[(\nabla\phi)_P \cdot (x_f - x_P)] \quad (\text{A.28})$$

lies between the minimum and maximum values of the neighbouring cell centers [43]. The cell-limiting is chosen, as it is a middle ground in being very computationally effective while only reverting on to first-order accuracy when necessary.

Finally, the diffusive flux  $\sum_f \Gamma_f (\nabla\phi)_f \cdot \mathbf{S}_f$  needs to be discretized. The diffusivity  $\Gamma_f$  at each cell face is evaluated using the second-order accurate central differencing (linear) interpolation scheme, which is also used as the default scheme for most other interpolatoin [66]:

$$\Gamma_f = \omega \Gamma_P + (1 - \omega) \Gamma_N, \quad \omega = \frac{\|x_f - x_N\|}{\|x_P - x_N\|}$$

The gradient is computed as described before. However, before contracting it with the face-area vector  $S_f$ , an non-orthogonality correction is applied [44]. The face vector is decomposed into orthogonal and non-orthogonal components: the orthogonal part enters the implicit matrix treatment, while the non-orthogonal remainder is added explicitly as a source term [44]. This helps to conserve second-order accuracy even in highly skewed or orthogonal mesh regions.

The numerical schemes outlined above discretize the governing equations and are selected to deliver second-order accuracy wherever feasible, while ensuring stability and boundedness in regions that demand it.

## A.4 Solver

As described, this study uses the incompressible Navier-stokes equations to simulate the flow field. In this formulation, the continuity equation does not contain the pressure explicitly (see 3.1). This leads to a linear system in the form of

$$\begin{pmatrix} A & B^T \\ B & 0 \end{pmatrix} \begin{pmatrix} \mathbf{u} \\ p \end{pmatrix} = \begin{pmatrix} \mathbf{f} \\ g \end{pmatrix} \quad (\text{A.29})$$

where  $A$  is the discretized momentum operator,  $B$  the discrete divergence,  $B^T$  the discrete gradient,  $\mathbf{u}$  the velocity vector, and  $p$  the pressure scalar.

Because there is no direct pressure coupling in the incompressible continuity equation, the bottom right is set to zero, which makes the combined system indefinite (positive and negative eigenvalues). This property makes this linear system particularly challenging to

solve since many standard solvers fail on non-positive-definite systems.

To address this challenge, Patankar and Spalding [51] introduced the Semi-Implicit Method for Pressure-Linked Equations (SIMPLE), which decouples the pressure and velocity fields in incompressible flow by splitting the solution into a predictor and corrector loop.

The SIMPLE cycle starts by guessing a pressure, velocity and temperature field, before solving the under-relaxed energy equation and assembling the momentum Matrix  $A_u$ . It then uses the current pressure  $p^n$  to solve the discretized momentum equations and predict a provisional velocity  $u^*$ . From the divergence of  $u^*$ , the pressure correction equation is formed and solved to yield  $p'$ , which is then used to update the pressure to  $p^{n+1}$ . This updated pressure is subsequently used to recompute the face fluxes and correct the velocity ( $u^{n+1}$ ) to enforce continuity. Finally, the Residuals or step count are checked. If the solution hasn't converged, the corrected pressure and velocity become the new "old" fields, and the loop repeats until the desired step count or tolerance is reached:

1. **Initialization:** prescribe initial fields  $p^0$ ,  $\mathbf{u}^0$  and  $T^0$ ; set iteration counter  $i = 0$ .
2. **Energy solve:** assemble and under-relax the discretized energy equation

$$\nabla \cdot (\mathbf{u} T) - \nabla \cdot (\alpha \nabla T) = r \implies \mathbf{A}_T T^* = \mathbf{r},$$

then solve for the provisional temperature  $T^*$ .

3. **Momentum matrix assembly:** form and under-relax the coefficient matrix

$$\mathbf{A}_u \mathbf{u} - \mathbf{b} = 0,$$

where  $\mathbf{b}$  contains all explicit source and convection contributions.

4. **Momentum predictor:** solve

$$\mathbf{A}_u \mathbf{u}^* - \mathbf{b} = -\nabla p^n$$

for the intermediate velocity  $\mathbf{u}^*$ .

5. **Pressure-correction equation:** assemble and solve

$$\nabla \cdot \left( \frac{1}{a_p} \nabla p' \right) = \nabla \cdot \mathbf{u}^*,$$

to obtain the pressure correction  $p'$ .

6. **Pressure update:**

$$p^{n+1} = p^n + \alpha_p p',$$

with  $\alpha_p$  the pressure relaxation factor.

7. **Flux correction:** recompute face fluxes

$$\phi_f := \mathbf{S}_f \cdot \left( \frac{\mathbf{H}(\mathbf{u})}{A} \right)_f - \left( \frac{|\mathbf{S}_f|}{A} \right)_f \nabla_n p_f$$

then under-relax  $p$  as above.

8. **Momentum correction:**

$$\mathbf{u}^{n+1} = \mathbf{u}^* - \frac{1}{a_p} \nabla p',$$

yielding the corrected velocity field.

9. **Convergence check:** if residuals of  $p$ ,  $\mathbf{u}$  or  $T$  remain above tolerance, set  $n \leftarrow n + 1$ , increment  $i$ , and repeat from step 2; otherwise stop.

The SIMPLE algorithm is the most commonly used approach in CFD codes to obtain a steady solution of the incompressible Navier-Stokes equations because it not only helps to circumvent the saddle-point problem (indefinite matrix) but also offers the possibility of internal non-orthogonal corrector loops and under-relaxation.

Under-relaxation in the context of CFD, refers to scaling back each update of a field before applying it. Mathematically, the strength of the under-relaxation is defined by a so-called under-relaxation factor  $\alpha \in [0, 1]$  and is computed as follows:

$$\phi^{new} = \phi^{old} + \alpha \Delta \phi \quad (\text{A.30})$$

By choosing  $\alpha < 1$ , strong fluctuations and overshoots, that could destabilize the simulation, can be damped, which helps to prevent initial blowups and to converge the simulation smoothly. This is especially useful for turbulent flows, which are prone to initial instabilities.

## A.5 SnappyHexMeshDict

```
//-----*- C++ -*-----*\
| ===== |
| \ \      / F i e l d      | OpenFOAM: The Open Source CFD Toolbox |
| \ \      / O p e r a t i o n | Version: v2406 |
| \ \      / A n d | Website: www.openfoam.com |
| \ \ /      M a n i p u l a t i o n |
| \ \ /      M a n i p u l a t i o n |
\*-----*-*/
FoamFile
{
    version      2.0;
    format       ascii;
    class        dictionary;
    object       snappyHexMeshDict;
}

// Which of the steps to run
castellatedMesh true;
snap           true;
addLayers      true;

geometry
{
```

```
Gyroid10.stl
{
    type triSurfaceMesh;
    name TPMS;
}

refinementBox
{
    type box;
    min (-17 -10 -10);
    max ( 35  10  10);
}

}

// Settings for the castellatedMesh generation.
castellatedMeshControls
{
    maxLocalCells      100000;
    maxGlobalCells     1000000;
    minRefinementCells 6;
    maxLoadUnbalance   0.10;
    nCellsBetweenLevels 5;

    features
    (
        {
            file "Gyroid10.eMesh";
            level 3;
        }
    );

    refinementSurfaces
    {
        TPMS
        {
            level (2 3);
            patchInfo { type wall; }
        }
        bottomWallFront
        {
            level (1 1);
            patchInfo { type patch; inGroups (allWalls); }
        }
    }

    resolveFeatureAngle 60;
```

```

    refinementRegions
    {
        TPMS          { mode inside; levels ((1 3)); }
        refinementBox { mode inside; levels ((1 2)); }
    }

    locationInMesh (0 -3 0);
    allowFreeStandingZoneFaces true;
}

// Settings for the snapping.
snapControls
{
    nSmoothPatch      4;
    tolerance         2.0;
    nSolveIter        40;
    nRelaxIter        20;
    nFeatureSnapIter  35;
    implicitFeatureSnap false;
    explicitFeatureSnap true;
    multiRegionFeatureSnap false;
}

// Settings for the layer addition.
addLayersControls
{
    relativeSizes      true;
    firstLayerThickness 0.035;
    expansionRatio      1.11;
    minThickness        0.0005;

    meshShrinker        displacementMotionSolver;
    solver               displacementLaplacian;

    displacementLaplacianCoeffs
    {
        diffusivity inverseDistance 1(TPMS);
    }

    layers
    {
        TPMS { nSurfaceLayers 12; }
    }

    nGrow              0;
    featureAngle       120;
    nLayerIter         100;

```

```

        slipFeatureAngle      180;
        nRelaxIter            20;
        nSmoothSurfaceNormals  5;
        nSmoothNormals        30;
        nSmoothThickness       30;
        maxFaceThicknessRatio  1;
        maxThicknessToMedialRatio 0.9;
        minMedialAxisAngle     3;
        nBufferCellsNoExtrude  0;
    }

    // Generic mesh quality settings.
    meshQualityControls
    {
        #include "meshQualityDict"
    }

    writeFlags
    (
        scalarLevels
        layerFields
    );

    // Merge tolerance.
    mergeTolerance 1e-6;

```

## A.6 Nusselt Number Calculation in Buoaynt Solver

```

1  Info << "Calculating Nusselt number on TPMS surface using midpoint bulk "
2      << "temperature and temperature-dependent k" << endl;
3
4  dimensionedScalar kappaBase("kappa",
5      dimEnergy/(dimTime*dimLength*dimTemperature),
6      laminarTransport);
7  dimensionedScalar LRef("L_ref", dimLength, laminarTransport);
8
9  const volScalarField& T = mesh.lookupObject<volScalarField>("T");
10
11  label inletPatchI = mesh.boundaryMesh().findPatchID("inlet");
12  label outletPatchI = mesh.boundaryMesh().findPatchID("outlet");
13  if (inletPatchI < 0 || outletPatchI < 0) {
14      FatalErrorInFunction
15          << "Patch 'inlet' or 'outlet' not found." << nl
16          << abort(FatalError);
17  }
18
19  // inlet bulk temperature
20  const fvPatchScalarField& T_inPatch = T.boundaryField()[inletPatchI];
21  scalarField areaIn = mag(mesh.Sf()).boundaryField()[inletPatchI];
22  scalar T_inlet = gSum(T_inPatch * areaIn) / gSum(areaIn);

```

```
23
24 // outlet bulk temperature
25 const fvPatchScalarField& T_outPatch = T.boundaryField()[outletPatchI];
26 scalarField areaOut = mag(mesh.Sf().boundaryField()[outletPatchI]);
27 scalar T_outlet = gSum(T_outPatch * areaOut) / gSum(areaOut);
28
29 scalar T_bulk = 0.5*(T_inlet + T_outlet);
30 Info << " Midpoint bulk temperature : " << T_bulk << " K" << endl;
31
32 // temperature dependent conductivity lookup
33 static const scalar TTable[5] = {273.0, 298.0, 373.0, 573.0, 873.0};
34 static const scalar kTable[5] = {0.02436, 0.02500, 0.03162, 0.04441,
35     0.06114};
36
37 auto lookupK = [&](scalar Tf) {
38     if (Tf <= TTable[0]) return kTable[0];
39     for (label i = 0; i < 4; ++i) {
40         if (Tf <= TTable[i+1]) {
41             scalar t0 = TTable[i], t1 = TTable[i+1];
42             scalar k0 = kTable[i], k1 = kTable[i+1];
43             return k0 + (k1-k0)*(Tf - t0)/(t1 - t0);
44         }
45     }
46     return kTable[4];
47 };
48
49 volScalarField qWall(
50     IOobject("qWall", runTime.timeName(), mesh,
51         IOobject::NO_READ, IOobject::AUTO_WRITE),
52     mesh,
53     dimensionedScalar("zero", T.dimensions()/dimLength, 0.0)
54 );
55
56 volScalarField Nu(
57     IOobject("NusseltNumber", runTime.timeName(), mesh,
58         IOobject::NO_READ, IOobject::AUTO_WRITE),
59     mesh,
60     dimensionedScalar("zero", dimless, 0.0)
61 );
62
63 forAll(Nu.boundaryField(), patchI) {
64     if (mesh.boundary()[patchI].name() != "TPMS") continue;
65
66     const fvPatchScalarField& Tpatch = T.boundaryField()[patchI];
67     const scalarField& Twall = Tpatch;
68
69     tmp<scalarField> tGradT = Tpatch.snGrad();
70     const scalarField& gradT = tGradT();
71
72     const labelList& faceCells = mesh.boundary()[patchI].faceCells();
73     scalarField Tfluid(faceCells.size());
74     forAll(faceCells, i) {
75         Tfluid[i] = T.internalField()[faceCells[i]];
76     }
77
78     scalarField kLocal(faceCells.size());
79     forAll(kLocal, i) {
80         kLocal[i] = lookupK(Tfluid[i]);
81     }
82 }
```

```

80     }
81
82     qWall.boundaryFieldRef()[patchI] =
83         -kLocal * gradT;
84
85     Nu.boundaryFieldRef()[patchI] =
86         -LRef.value()*qWall.boundaryField()[patchI]
87         / (kLocal*(Twall - T_bulk));
88
89     scalarField areaMag = mag(mesh.Sf().boundaryField()[patchI]);
90     scalar avgNu = gSum(Nu.boundaryField()[patchI]*areaMag)
91         / gSum(areaMag);
92
93     if (Pstream::master()) {
94         Info << "Time " << runTime.timeName()
95             << "      Avg. Nusselt on TPMS: " << avgNu << endl;
96         OFstream avgFile(runTime.path()/ "averageNu.dat");
97         avgFile << runTime.timeName() << " " << avgNu << nl;
98     }
99 }
100
101 if (runTime.outputTime()) {
102     qWall.write();
103     Nu.write();
104 }

```

Listing A.1: Calculating Nusselt number on TPMS surface

## A.7 Finite Volume Schemes Settings

```

1  /*-----*- C++
2  / ===== /
3  / \ \      / F i e l d      / O p e n F O A M :   T h e   O p e n   S o u r c e   C F D   T o o l b o x
4  / \ \      / O p e r a t i o n      / V e r s i o n :   v 2 4 0 6
5  / \ \      / A n d      / W e b s i t e :   w w w . o p e n f o a m . c o m
6  / \ \ /      M a n i p u l a t i o n      /
7  \*-----*/
8  FoamFile
9  {
10     version      2.0;
11     format        ascii;
12     class         dictionary;
13     object        fvSchemes;
14 }
15 // * * * * *
16 //
17 ddtSchemes
18 {

```

```

19     default          steadyState;
20 }
21
22 gradSchemes
23 {
24     default          Gauss linear;
25     grad(U)          cellLimited Gauss linear 0.8;
26     grad(T)          cellLimited Gauss linear 0.9;
27     grad(p)          cellLimited Gauss linear 1;
28 }
29
30 divSchemes
31 {
32     default          none;
33
34     div(phi,U)        bounded Gauss limitedLinearV 0.5; //Gauss linearUpwindV
35         grad(U);
36     div(phi,T)        bounded Gauss limitedLinearV 0.5;
37
38     turbulence        bounded Gauss upwind;
39     div(phi,k)        $turbulence;
40     div(phi,omega)    $turbulence;
41     div(phi,epsilon)  $turbulence;
42
43     div((nuEff*dev2(T(grad(U)))) Gauss linear;
44 }
45
46 laplacianSchemes
47 {
48     default          Gauss linear limited 0.9;
49     laplacian(diffusivity,cellDisplacement) Gauss linear corrected;
50 }
51
52 interpolationSchemes
53 {
54     default          linear;
55 }
56
57 snGradSchemes
58 {
59     default          corrected;
60 }
61
62 fluxRequired
63 {
64     default          no;
65     p_rgh;
66     T;
67     k;
68     omega;
69 }
70
71 wallDist
72 {
73     method          meshWave;
74 }

```

75

// \*\*\*\*\*  
//

**Listing A.2:** Contents of fvSchemes for buoyant solver